UNIVERSITY OF CALIFORNIA, SAN DIEGO

The Diocotron Echo and Trapped-Particle Diocotron Mode in Pure Electron Plasmas

A dissertation submitted in partial satisfaction of the

requirements for the degree Doctor of Philosophy

in Physics

by

Jonathan Hwa-Jing Yu

Committee in charge:

Professor C. Fred Driscoll, Chairman
Professor Daniel Dubin
Professor Thomas O'Neil
Professor George Tynan
Professor William Young

2004

Table of Contents

List of Figures

Acknowledgements

I would like to thank my advisor Fred Driscoll for his insight, advice, and approachability. In addition, my “labmate” Dr. Andrey Kabantsev has been an example of persistence and experimental efficiency in uncovering plasma mysteries; he also gave me a glimpse of the true Russian spirit. Some of the most educational (and entertaining) moments in the lab involved discussions with both Andrey and Fred. Typically, Andrey would make a bold scientific statement, seemingly out of the blue; Fred would then challenge him by going straight to the data, and would come up with a burning new insight that usually complemented Andrey’s original statement.

It has been a great pleasure and privilege to work in the same research group as Professors Tom O’Neil and Dan Dubin. Prof. O’Neil was tremendously helpful to my graduate career by patiently working with me on the theory in this thesis. Prof. Dubin always had an open door and was willing to answer my questions.

I appreciated discussions with Dr. Francois Anderegg, who was always generous and did science (and everything else) extremely thoroughly. I also thank the graduate students in the group for companionship and useful discussions, including Nobu Shiga, Eric Bass, Dan Creveling, and Stas Kuzmin, and former grads Terry Hilsabeck, James Danielson, Jason Kriesel, David Schecter (who inspired me to search for echoes), and Eric Hollmann (for putting up with me in the Mexican jungles). Thanks to Jo Ann Christina for all her hard work and her help in making

the group run smoothly.

My family and friends provided incredible support during my time at UCSD. Thanks to my parents, David and Carolyn, who encouraged me and have been very supportive. Thanks to Christine and Jacque Moutier for their hospitality and generosity, and thanks to Luke and Camille for all their love. Thanks to Soren Solari, for letting me beat him (yet again) in fooseball, and for providing great friendship. A special thank you goes to Beverly Fruto, who has inspired and sustained me these last few years. She has been incredibly patient and has given me much joy.

Vita, Publications and Fields of Study

Vita

6 June 1972	Born, Seattle, Washington
1995	B.A., University of California, Berkeley
1994-1995	Lab Assistant, Center for Beam Physics Lawrence Berkeley National Laboratory
1996-1998	Engineering Technician, AlliedSignal Corporation Lawrence Livermore National Laboratory
1998-1999	Teaching Assistant, Department of Physics University of California, San Diego
1999-2004	Research Assistant, Department of Physics University of California, San Diego
1999	M.S., University of California, San Diego
2004	Ph.D., University of California, San Diego

Publications

1. J. H. Yu, C. F. Driscoll, and T. M. O'Neil, "Fluid Echoes in a Pure Electron Plasma," in preparation for *Physical Review Letters*.

2. A.A. Kabantsev, J.H. Yu, R.B. Lynch, and C.F. Driscoll, "Trapped Particles and Asymmetry-Induced Transport," *Physics of Plasmas* **10**, 1628 (2003).

3. J.H. Yu and C.F. Driscoll, "Diocotron Wave Echoes in a Pure Electron Plasma," *IEEE Trans. on Plasma Science* **30**, 24 (2002).

4. J.H. Yu and C.F. Driscoll, "Experimental Observations of Fluid Echoes in a Non-Neutral Plasma," *Non-Neutral Plasma Physics IV*, edited by F. Anderegg, *et al.* (American Institute of Physics, San Diego, California, 2002).

5. A.A. Kabantsev, C.F. Driscoll, T.J. Hilsabeck, T.M. O'Neil, and J.H. Yu, "Trapped-Particle Asymmetry Modes in Single-Species Plasmas," *Physical Review Letters* **87**, 225002 (2001).

Fields of Study

Major Field: Physics

Studies in Theoretical Mechanics
Professor Patrick Diamond

Studies in Advanced Classical Electrodynamics
Professor Daniel Dubin

Studies in Quantum Mechanics
Professor George Fuller

Studies in Equilibrium Statistical Mechanics
Professor Daniel Arovas

Studies in Plasma Physics
Professor Patrick Diamond

Studies in Fluid Mechanics
Professor Clint Winant

Studies in Ocean Turbulence and Mixing
Professor Laurence Armi

Studies in General Relativity
Professor Benjamin Grinstein

Studies in Nonlinear and Nonequilibrium Dynamics
Professor Patrick Diamond

Studies in Mathematical Physics
Professor Herbert Levine

Abstract of the Dissertation

The Diocotron Echo and Trapped-Particle Diocotron Mode in Pure Electron Plasmas

by

Jonathan Hwa-Jing Yu
Doctor of Philosophy in Physics
University of California, San Diego
Professor C. Fred Driscoll, Chairman

Experiments are presented on dissipationless damping and echo generation of $k_z = 0$ diocotron waves; and on dissipative damping of the trapped-particle diocotron mode (TPDM) in pure electron plasmas.

The diocotron wave echo demonstrates the reversible nature of spatial Landau damping. An initial launched wave damps due to the phase mixing process of spatial Landau damping, and this is seen in experimental images as spiral wind-up of the density perturbation. A second launched wave reverses this phase mixing, and the unwinding results in a third diocotron wave that spontaneously appears as the echo. Experiments agree with a simple ballistic theory on the basic echo characteristics.

These waves also represent Kelvin waves on an "ideal" rotating 2D fluid, and we refer to the diocotron wave echoes as *fluid echoes.* Real electron plasmas have v_z-dependent particle drifts in the ends, violating the ideal 2D perspective; but surprisingly, the echo is *not* destroyed by this θ-smearing. In essence, separate

v_z-classes of particles execute separate wind-up and unwinding, resulting in the same echo.

At late times, the echo *is* destroyed by weak collisional velocity scattering between these separate v_z-classes. The experimental measurements show quantitative correspondence with calculation of collisional interchange of v_z-classes. In addition, large second wave excitation supresses late-time echoes, but this effect is not yet understood.

Separate experiments characterized the novel Trapped Particle Diocotron Mode. The TPDM consists of passing and trapped particles on either side of an electrostatic potential barrier. The trapped particles undergo $\mathbf{E} \times \mathbf{B}$ drift oscillations that are 180° out of phase on either side of the barrier, while passing particles move along field lines to (partially) Debye shield the potential created by trapped particles.

The damping of the TPDM is caused by collisional diffusion across the separatrix between trapped and passing particles. When the confinement fields have θ-asymmetries, these same dissipative separatrix crossings also cause bulk radial transport of particles. Strikingly, the measured asymmetry-induced transport rates are found to be directly proportional to the measured mode damping rates, with simple scalings for all other plasma parameters.

Chapter 1

Overview

1.1 Introduction

In this thesis, I present experiments on two types of wave damping: *reversible*, dissipationless spatial Landau damping of $k_z = 0$ diocotron waves, enabling echo formation; and *irreversible*, dissipative damping of the trapped-particle diocotron mode (TPDM), with accompanying bulk radial particle transport. The $k_z = 0$ diocotron waves used in the echo experiments damp due to the collisionless wave-particle resonance of spatial Landua damping, while the TPDM damps due to collisional diffusion across the separatrix between trapped and passing particles.

1.2 Echoes

The fluid echo is the spontaneous appearance of a diocotron wave after two externally excited waves have damped away, and this explicity demonstrates the reversible nature of spatial Landau damping. We find that the echo lifetime is limited by weak collisional velocity scattering, which causes irreversibility of subtle non-2D (confinement-field-induced) θ-drifts. The echoes provide further evidence that a nonneutral plasma behaves like an inviscid 2D fluid, despite non-2D effects of the end confinement fields. A simplifying feature of the inviscid wave damping and echo generation is that the phase mixing and unmixing can be imaged directly in (r, θ) configuration space.

To a certain extent, the observation of the echo violates everyday notions regarding the arrow of time. Classically, the dynamics of an *individual* particle is completely reversible; however, the evolution of a *collection* of particles is often determined by the (collisional) entropy increase, leading to the directionality of time. Thus, the (partial) reconstruction of the initial wave, after exciting a second wave, is particularly striking.

Echo phenomena have been seen in a variety of systems spanning many scientific disciplines, including optics [1], atomic physics [2], and plasma physics [3, 4]. Previous work by Malmberg and Wharton [5] reported spatially-separated echoes in a neutral plasma, where the phase mixing was due to “regular” velocity-space Landau damping. In addition, fluid echoes have been predicted [6, 7] and modelled numerically [8].

Here, the first experimental measurements of 2D fluid echoes are presented. Diocotron waves are $\mathbf{E} \times \mathbf{B}$ drift waves rotating in the r–θ plane, as opposed to longitudinal compression waves. The diocotron waves manifest themselves as bulk shape distortions of the plasma column, and also represent Kelvin waves on a rotating 2D inviscid fluid. The fluid echoes are temporally separated from the orignal waves, as opposed to spatially separated. In addition, the wave-particle resonance for inviscid diocotron wave damping occurs in configuration space, as opposed to velocity space for longitudinal plasma wave damping.

To produce the echo, we excite two strongly damped, temporally separated diocotron waves by applying voltage bursts to sectored wall cylinders. The density perturbation of the initial wave executes spiral wind-up as it rotates with the sheared $\mathbf{E} \times \mathbf{B}$ flow of the plasma. Essentially, each “shell” of the plasma rotates at a different rate, stretching the initially aligned density perturbation into a spiral. The second excitation creates θ-dependent radial drifts of the initial spiral pattern. This distorted density perturbation pattern continues to evolve in the sheared plasma flow, and effectively un-winds. After some time, the perturbations in the various shells re-align, resulting in the echo.

We compare the echo measurements to a ballistic, collisionless echo theory. We find the experiments agree with this theory regarding the mode number of the echo, the time of echo appearance, and the “saturation” effect at large values of the product of the second wave amplitude and second wave launch time. At late times, however, the collisionless theory fails, and we investigate effects which could destroy phase coherence and the echo.

Surprisingly, θ-smearing due to weak non-2D θ-drifts [9] in the end confinement fields does not destroy the echo. This θ-smearing is due to the radial component of the confinement electric field causing azimuthal $\mathbf{E} \times \mathbf{B}$ drifts. The effect depends on the particle's z-velocity v_z. Thus, particles within each velocity class experience the same wind-up (and unwinding) in the end fields, which is an extra phase mixing that contributes to the plasma shear-induced wind-up.

We evaluate a second-order ballistic theory that describes the collisional irreversibility of the end-field θ-smearing. The longest observed echo times give effective collision frequencies ν_{eff} that agree surprisingly well with the unavoidable electron-electron collisions. In addition, we artificially enhance the velocity scattering rate by adding noise to one of the confinement cylinders. Even a small level of noise (61 mV rms) causes an increase in ν_{eff} by over a factor of 20, compared with no noise applied. These results support the idea that velocity scattering between velocity classes, together with velocity dependent θ-smearing, destroys the echo.

In addition, we find that large second wave amplitudes destroy the echo up to 5× faster than predicted by the collisional theory, but this effect is not yet understood quantitatively.

We also observe higher-order "echoes of echoes," and echoes of spatial harmonics of the applied wall excitations, for certain values of the second wave amplitude and launch times. These higher-order echoes can produce a striking (but confusing) chain of echoes that persists much longer than the late-time observations of the lowest-order (second-order) echo.

1.3 Trapped-Particle Diocotron Modes, Transport

The TPDM [10] consists of passing and trapped particles on either side of an electrostatic potential barrier, which is created by applying an "electric squeeze" near the z-center of the electron column. The trapped particles undergo $\mathbf{E} \times \mathbf{B}$ drift oscillations that are 180° out of phase on either side of the barrier, while passing particles move along field lines to (partially) Debye shield the potential created by trapped particles.

The TPDM damps due to collisional diffusion across the velocity space separatrix between trapped and passing particles [11, 12]. This damping is similar to that for the dissipative trapped-ion mode, and may be the closest connection the field of nonneutral plasmas has yet made to the neutral plasma physics community. In this connection, the trapped particles correspond to the ions, and passing particles correspond to electrons. In addition, "asymmetry-induced" currents in a non-neutral plasma are similar to bootstrap currents in a tokamak, and trapped-particle modes in both systems are related to a type of neoclassical transport.

A recent theory of TPDM damping predicts a damping rate [13] that scales as $\sqrt{\nu/\omega_a}$, where ω_a is the TPDM frequency. The square root gives a significant enhancement in low collisionality plasmas, leading us to believe that trapped-particle-mediated effects are quite prevalent in pure electron traps.

We also use an intentional or inherent localized increase in the magnetic field as a magnetic trapping barrier, in order to study collisional scattering across a magnetic separatrix. The mode, however, is observed only with electric trapping, and remains elusive with magnetic trapping. Experiments suggest that the magnetically trapped mode is either very strongly damped, or has zero frequency.

In the presence of θ-asymmetries, the collisional separatrix crossings also cause bulk radial transport. We find that the transport rate ν_p is directly proportional to the TPDM damping rate γ_a, with simple scalings for all other plasma parameters. This correspondence between ν_p and γ_a shows that diffusion across the separatrix is responsible for both particle transport and TPDM damping.

We find that the measured transport rate is independent of the fraction of magnetically trapped particles over a wide range of magnetic mirror strengths, so even small magnetic trapping barriers cause significant transport. We speculate that trapped-particle-mediated effects explain the $(L_p/B)^{-2}$ lifetime scalings observed in pure electron traps for the past 20 years. One of the most important results of studying the TPDM is elucidating the detailed mechanism of asymmetry-induced transport for a wide range of plasma parameters.

We use selective dumping techniques to study the dynamical equilibrium of a “tilted” plasma, and to obtain the dynamical properties of “trapped particles.” We find that the dynamical equilibrium position of a tilted plasma is shifted approximately 90° from the tilt axis. This represents the perpendicular drift of passing particles as they execute a partial diocotron orbit centered at the equilibrium position. We also see evidence for the “Debye shielded” density perturbations assumed in the theory of the TPDM. These results may be useful in directing future theory work on TPDM damping and transport in the presence of θ-asymmetries.

Chapter 2

Background for the Experiments

2.1 Description of CamV Apparatus

All experiments in this thesis are performed on the CamV [14, 15, 16] Penning-Malmberg trap at UCSD. The electron trap is shown schematically in Figure 2.1, and consists of a stack of conducting cylinders immersed in an axial z-magnetic field, which provides radial confinement of the plasma. A hot tungsten source emits electrons, which are confined axially using negative voltages on the end cylinders. We use sectored wall cylinders ($4\times60^\circ$ sectors on S4, and $8\times25^\circ$ sectors on S7) to excite and detect diocotron waves. In addition, at a chosen time in the plasma evolution, we destructively dump the plasma onto a phosphor screen and image the fluorescence, giving a z-integrated electron density map $n(r, \theta)$.

The vacuum chamber (with neutral gas pressure $P \lesssim 10^{-10}$ torr) resides inside the bore of a superconducting solenoid magnet. The magnetic field is typically set at 1 to 10 kG, causing electrons to rapidly cyclotron orbit around a field line at the cyclotron frequency Ω_c. Negative potentials (typically $-V_c = -100$ V) applied to end cylinders provides axial confinement, and electrons bounce from one end to another at a rate f_b.

The fastest rate of motion of the trapped electrons is the cyclotron fre-

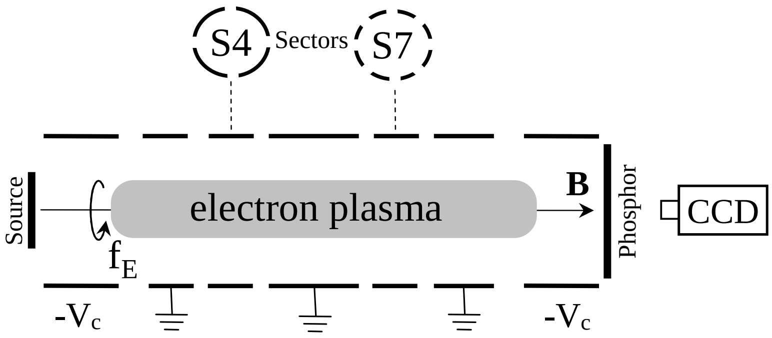

Figure 2.1: Schematic of UCSD's CamV Penning-Malmberg electron trap.

quency:

$$\begin{aligned} \Omega_c &\equiv \frac{eB}{\mathrm{m}c} \qquad (2.1) \\ &\approx 2.8 \times 10^9\,\mathrm{sec}^{-1}\,(2\pi)\left[\frac{B}{1\,\mathrm{kG}}\right], \end{aligned}$$

where m is the mass of the electron.

The axial bounce frequency between the confinement potentials is given by

$$f_b \equiv \frac{v_z}{2L_p} \qquad (2.2)$$

$$\begin{aligned} \bar{f_b} &\equiv \frac{\bar{v}}{2L_p} \qquad (2.3) \\ &\approx 2.1 \times 10^6\,\mathrm{sec}^{-1}\left[\frac{T}{1\,\mathrm{eV}}\right]^{1/2}\left[\frac{L_p}{10\,\mathrm{cm}}\right]^{-1}. \end{aligned}$$

In general, the plasma length $L(r, v_z)$ is a function of the electron radius and axial velocity v_z. Here we define L_p as the distance between end reflection points of a thermal electron, at $r = 0$, i.e.,

$$L_p \equiv L(r = 0, v_z = \bar{v}), \qquad (2.4)$$

where the thermal velocity $\bar{v} \equiv \sqrt{T/\mathrm{m}}$.

The radial electric field $E_r(r) = -\partial\phi(r)/\partial r$ from the un-neutralized plasma leads to an $\mathbf{E}\times\mathbf{B}$ drift in the azimuthal direction, with rotation frequency

$$\begin{aligned} f_E(r) \;&\equiv\; \frac{\omega_E(r)}{2\pi} \;\equiv\; \frac{c}{2\pi r B}\frac{\partial\phi(r)}{\partial r} \\ &\approx\; 1.4\times 10^5\,\mathrm{sec}^{-1}\left[\frac{n}{10^7\,\mathrm{cm}^{-3}}\right]\left[\frac{B}{1\,\mathrm{kG}}\right]^{-1}, \end{aligned} \tag{2.5}$$

where the numerical approximation assumes constant density. Later, in Section 3.4, we consider 3D end effects that make the rotation frequency depend on an electron's z-velocity. The bounce-averaged $\mathbf{E}\times\mathbf{B}$ frequency is then $f_R(r, v_z) \equiv f_E(r) + f_{end}(r, v_z)$ (see Equation 3.28 and Equation 3.32).

The frequency ordering is thus

$$\Omega_c > f_b > f_R, f_m, \tag{2.6}$$

where f_m is the diocotron mode frequency with azimuthal mode m. The fast cyclotron motion makes guiding-center theories applicable, and the fast bounce motion compared with the $\mathbf{E}\times\mathbf{B}$ drift frequency makes the system approximately 2D, as discussed next.

2.2 Magnetized Plasma as a 2D Fluid

One aesthetically and scientifically pleasing aspect of a nonneutral plasma is the dynamical similarity between a pure electron plasma and a 2D incompressible, inviscid fluid [17].

Because the electron axial bounce time f_b^{-1} is much less than the characteristic time scale for the flow of electrons in the r-θ plane (i.e. an eddy turn-over time, or the $\mathbf{E}\times\mathbf{B}$ rotation period f_E^{-1}), the "instantaneous" r-θ velocity of an electron can be approximated by its average velocity over a bounce period. The 2D fluid equations obtained from this bounce-averaging are known as the drift-Poisson equations [18]:

$$\begin{aligned}&(a)\;\; \partial n/\partial t + \mathbf{v}\cdot\nabla n = 0,\\ &(b)\;\; \mathbf{v} = \hat{z}\times c\nabla\phi/B,\\ &(c)\;\; \nabla^2\phi = 4\pi e n.\end{aligned} \tag{2.7}$$

Above, $\mathbf{v}(r,\theta,t)$ is the $\mathbf{E}\times\mathbf{B}$ drift velocity field, $n(r,\theta,t)$ is the z-averaged electron density, and $\phi(r,\theta,t)$ is the electrostatic potential.

The 2D Euler equations describe the evolution of the vorticity ζ in the r-θ flow, and are given by

$$\begin{aligned}&(a)\;\; \partial\zeta/\partial t + \mathbf{v}\cdot\nabla\zeta = 0,\\ &(b)\;\; \mathbf{v} = \hat{z}\times\nabla\psi,\\ &(c)\;\; \nabla^2\psi = \hat{z}\cdot\nabla\times\mathbf{v}\equiv\zeta.\end{aligned} \tag{2.8}$$

Comparing Equation 2.7 with Equation 2.8, the $\mathbf{E}\times\mathbf{B}$ drift velocity corresponds to the fluid velocity, the stream function corresponds to the electrostatic potential by the relation $\psi\equiv c\phi/B$, and the vorticity corresponds to the electron density by the equation $\zeta = 4\pi e c n/B$. Thus, the vorticity is advected with the electron density.

Because ζ is proportional to n, vorticity measurements are (theoretically) equivalent to density measurements [17]. Vorticity is measured by dumping the electrons onto a phosphor screen, and recording the density (vorticity) image with a CCD camera. Although this imaging is destructive, the initial conditions are reproducible, so that the time evolution of flows can be studied. The density (vorticity) perturbation images in Chapter 3, for example, clearly show the spiral wind-up of vorticity, and unwinding that leads to echo formation.

In addition to directly imaging the vorticity, a pure electron plasma has extremely low viscosity, allowing detailed measurements of nearly inviscid 2D flows.

The wall of the electron trap is grounded, imposing the boundary condition $\phi = 0$ at $r = R_w$ which corresponds to free-slip at the wall of a circular container.

2.3 Linear Modes and Spatial Landau Damping

The dioctron wave echo is an explicit demonstration that spatial Landau damping is reversible. We provide here a brief review of the inviscid spatial Landau damping process, in both the weak ($\gamma_m/f_m << 1$) and strong ($\gamma_m/f_m \approx 1$, as in the echo experiments) damping regimes.

In the simplest and most physically meaningful description, spatial Landau damping results from electrons co-rotating with the diocotron wave. For damping to occur, the density gradient must be negative at the location of this resonance, meaning more electrons rotate faster (than the wave) than rotate slower. Electrons moving faster than the wave give energy to it, while those moving slower than the wave take energy from it. Thus, at resonance with a negative density gradient, the electrons' $\mathbf{E} \times \mathbf{B}$ rotation acts as an energy *source* for the diocotron wave. Since diocotron waves are negative energy waves, this exchange of energy from particles to wave *damps* the wave.

We discuss here $m = 2$ diocotron waves, where the quadrupole moment, or ellipticity of the electron plasma, represents the wave amplitude. In the experiments, the diocotron wave amplitude is typically measured from the induced charge on sectored wall cylinders; and this wall signal is directly proportional to the CCD-measured quadrupole moment of $n(r, \theta)$.

For *weak* spatial Landau damping, a rather complete theory description has been developed [18, 19, 20], predicting exponential damping of both the density perturbation and the quadrupole moment. In the *strong* damping regime, where the echo experiments are performed, the density perturbation no longer decays exponentially in the plasma center, but rather undergoes spiral wind-up [21, 22]. Nevertheless, the quadrupole moment (and wall signal) of the strongly damped diocotron mode *does* decay exponentially, and the decay rate agrees with the Landau pole prediction. Thus, spatial Landau damping is an appropriate physical description even in the strong damping regime, despite the fact that the density perturbation does not fully resemble a "quasimode."

From a theory perspective, a weakly damped diocotron mode is a quasimode, with the density perturbation behaving (at early times) like a single exponentially damped mode [19]. The decay rate is proportional to the original density gradient at the critical radius r_c, defined as the radius where the $\mathbf{E}\times\mathbf{B}$ drift rotation frequency $f_E(r)$ is resonant with the mode, i.e.,

$$m f_E(r_c) = f_m. \tag{2.9}$$

Here, f_m is the diocotron mode frequency for the chosen azimuthal mode m.

Analytically, a quasimode is considered to be a wave packet of undamped "continuum modes," each of which rotates at its own frequency. The damping of a quasimode is due to interference, or phase mixing, of these continuum modes. The quasimode's frequency spectrum closely resembles a Lorentzian, with width given by the damping rate γ_m. This finite width of the quasimode frequency spectrum leads to a finite range of radii which satisfy the wave-particle resonance condition. We call this range the critical layer Δr_c.

The description above follows from an eigenmode analysis of linear perturbations on a circular vortex [19]. Quasimodes were originally studied by Briggs *et al.* [18] using a Laplace transform to solve an initial value problem. This approach uncovers a Landau pole, which is a complex frequency with the real and imaginary parts appearing as the frequency $2\pi f_m$ and damping rate γ_m of a quasimode.

The values of f_m and γ_m from the Landau pole agree with Schecter's eigenmode analysis.

Not all $k_z = 0, m \neq 0$ diocotron modes are damped. For example, no damping occurs when the electron density (vorticity) gradient at r_c vanishes. In this case, the perturbation is no longer described by a wave packet of continuum modes, but instead by a single undamped "discrete mode." These discrete modes are readily observed in pure electron plasmas when the plasma radius small and the edge is abrupt, so that r_c lies outside the plasma [16]. (See, for example, Figure 2.3 with $V_a = 0$).

In 1880, Kelvin derived a dispersion relation for these discrete modes, by considering waves propagating along the edge of a vortex-patch [23]. This vortex-patch corresponds to a "top-hat" plasma density profile:

$$n(r) = \begin{cases} \bar{n} & r \leq R_o \\ 0 & r > R_o. \end{cases} \tag{2.10}$$

The discrete waves are delta-function disturbances at the edge of the plasma at R_o:

$$\delta n(r, \theta, t) = \delta(r - R_o) e^{i(m\theta - \omega_m t)}. \tag{2.11}$$

Substituting the above expression into the linearized Euler equations yields the discrete diocotron mode frequency

$$\omega_m = 2\pi f_m = \frac{4\pi e c}{B} \frac{\bar{n}}{2} \left[m - 1 + \left(\frac{R_o}{R_w} \right)^{2m} \right]. \tag{2.12}$$

These undamped discrete modes merge with the continuum, and become damped quasimodes, when the edge of the plasma is expanded past the critical radius r_c.

Here, the echo experiments are intentionally performed in the *strong* damping regime, so that the initial and second wave dampings are complete before non-ideal effects such as collisions come into play. Strong damping also ensures that the free-streaming motion of the density perturbation occurs overs a broad region Δr_c. In the experiments, Δr_c is seen as the range of radii over which spiral wind-up occurs (see Figure 3.2), and is typically a significant fraction of the wall radius.

2.4 Density Profile Shaping

The density profile is intentionally broadened in the echo experiments, in order to produce strong spatial Landau damping. Before the initial and second diocotron waves are excited, an azimuthal electric asymmetry is applied in either an $m = 1$ or $m = 2$ configuration for thousands of plasma rotation periods, resulting in bulk radial transport. The transport results from the applied field asymmetries exerting a torque on the plasma, and changing its angular momentum (and thus its mean square radius). The detailed mechanism of this process is presumably related to diffusion across inherent velocity-space separatrices between trapped and untrapped particles, which is described in detail in Chapter 4. These separatrices are created by small magnetic ripples of strength $\delta B/B \approx 10^{-3}$. Controlled experiments with asymmetry-induced transport are discussed later in Section 4.4 and Section 4.6.

Figure 2.2 shows how the asymmetry strength V_a affects the $m = 2$ diocotron mode frequency f_2, damping rate γ_2, temperature T, and plasma radius R_p. The asymmetry is applied for a duration of 700 ms in an $m = 2$ configuration (to two opposite 25° sectors).

The transport increases at larger values of V_a, demonstrated by the square data points in Figure 2.2. This expansion liberates electrostatic energy, which transforms into kinetic energy and increases the plasma temperature. The decrease in f_2 with increasing R_p is mainly due to the decrease in local density $n(r, \theta, t)$, since $f_2 \propto n$ (see Equation 2.12). The critical radius r_c lies outside the plasma

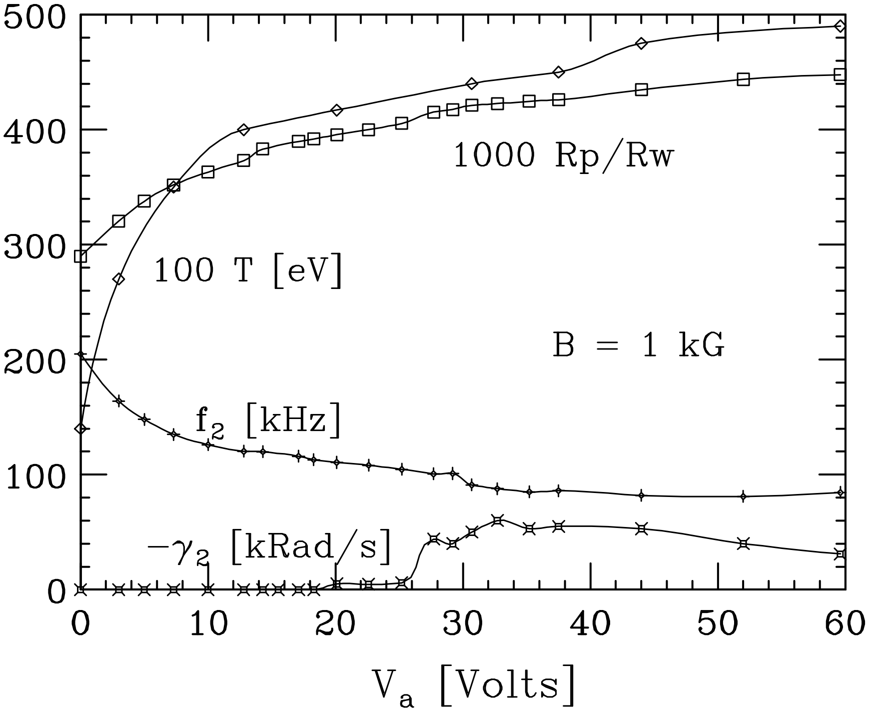

Figure 2.2: The plasma is broadened by applying an asymmetry of strength V_a. The plasma expansion causes plasma heating, and the $m = 2$ damping rate γ_m becomes nonzero when the critical radius lies inside the plasma.

until $R_p/R_w \gtrsim 0.4$ ($V_a \gtrsim 26$ V), at which point the mode is spatially Landau damped. The echo experiments are typically performed on a plasma shaped by an asymmetry strength $V_a = 30 \rightarrow 70$ V applied for a duration $\Delta t_a \approx 1\,\mathrm{sec}\left[\frac{B}{1\,\mathrm{kG}}\right]$.

Figure 2.3 shows density profiles with and without an $m = 2$ asymmetry of $V_a = 60$ V, for both $B = 1$ and 7 kG. At a given magnetic field, the plasmas with and without an asymmetry are held for equal times. The asymmetry is applied for 0.7 sec (1.9×10^5 $V_a = 0$ central plasma rotation periods) in the 1 kG case, and for 7.0 sec (4.6×10^5 central plasma rotation periods) in the 7 kG case.

The $m = 2$ diocotron wave critical radii r_c are marked in Figure 2.3. The critical radii are found from Equation 2.9 using the measured $m = 2$ frequencies and the calculated rotation frequency profiles. For the cases with $V_a = 0$, r_c lies

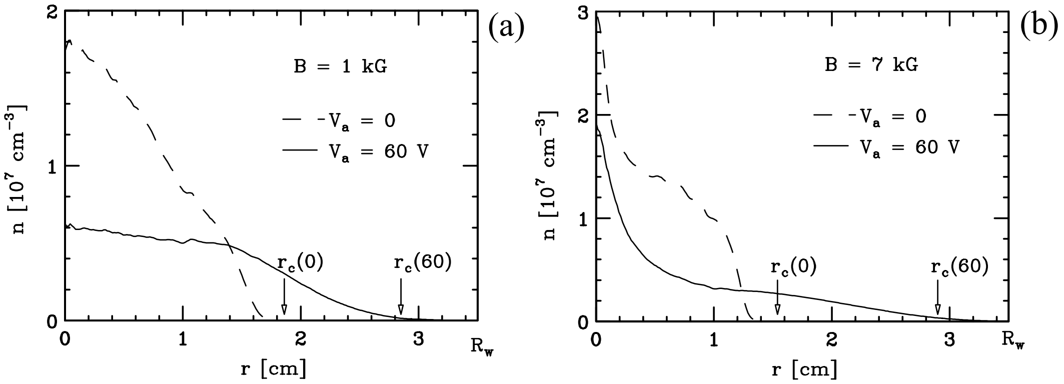

Figure 2.3: Density profiles with and without an applied $m = 2$ asymmetry, for (a) $B = 1$ kG and (b) 7 kG.

outside the plasma and no spatial Landau damping occurs. In contrast, the shaped profiles (shown as solid lines), with $r_c = 2.85$ and 2.89 cm for the 1 kG and 7 kG cases, respectively, have strong damping with $\gamma_2/f_2 = 0.4$.

Chapter 3

Diocotron Wave Echoes

3.1 Overview

In this chapter, diocotron wave echo experiments are presented, demonstrating the reversible nature of spatial Landau damping. These echoes are seen to be destroyed by collisional velocity scattering, which causes irreversibility of end-field θ-smearing. In addition, excessively large second wave excitations degrade the echo up to 5× faster than collisions.

An initial wave with azimuthal mode number m_i is excited at $t = 0$ and damps in a few wave periods ($0.3 \lesssim \gamma_m / f_m \lesssim 1$), forming a spiral density perturbation pattern. At $t = \tau$, a second dioctron wave with mode number $m_s > m_i$ is launched, and causes an unmixing of the initial spiral density perturbation pattern. The unmixing peaks near the echo appearance time t_e.

In Section 3.2, we present the measured echo wall signal and CCD images of the echo. The plasma density perturbation images show the spiral wind-up during the initial wave damping, and unwinding leading to the echo. A special feature of studying the echo in a nonneutral plasma is that the normally abstract, mathematical construct of phase space is directly seen, since configuration space (r, θ) is equivalent to phase space (p_θ, θ) by the relation $p_\theta = \frac{eB}{2c} r^2$. Thus, the spiral wind-up and unwinding of the density perturbation images directly represent phase mixing and unmixing.

A ballistic, collisionless theory for the echo is presented in Section 3.3. This theory treats the density perturbations as passive tracers that free-stream with the sheared $\mathbf{E} \times \mathbf{B}$ flow. The observed echo mode number $m_e = m_s - m_i$, time of echo appearance $t_e \equiv \tau m_s / m_e$, and “saturation” effect at large second wave amplitudes and large τ correspond to theory predictions.

In Section 3.4, we present theory describing θ-smearing due to non-2D effects from the end confinement fields. This effect depends on the particle z-velocity v_z; in the absence of collisions, each velocity class executes its own phase mixing and unmixing. Thus, θ-smearing alone does not destroy the echo.

We find in Section 3.5 that at late times, the echo lifetime is limited by collisional velocity scattering, which produces irreversibility of θ-smearing. A second-order collisional theory gives an effective electron-electron collision frequency ν_{eff} that agrees with the actual electron-electron scattering rate $\nu_{\|}$, provided the second wave amplitude is sufficiently small.

In Section 3.6, we find that the echo is destroyed by applying noise to a confinement ring. Noise artificially enhances velocity scattering, and the observed reduction in echo amplitude supports the conclusion of Section 3.5.

Other possible causes of phase decoherence are discussed in Sections 3.7 − 3.9 including viscosity, discreteness due to the electron cyclotron motion, and electron-neutral scattering.

For large second wave amplitudes the measured echo signal is smaller than the theory prediction, but this effect is not yet understood. In Section 3.10, we explore wall-induced and wave-induced trapping effects, and find that wall-trapping effects are not the cause of echo destruction at large second wave amplitudes.

Most likely a type of brief velocity mixing occurs due to the wall excitation. Particles $\mathbf{E} \times \mathbf{B}$ drift radially due to the E_θ fields imposed by the wall voltage. Since $\phi(r)$, these particles are displaced to a new electrostatic potential, which can change their z-energy. This velocity mixing can act on the θ-smearing effect, and can reduce the echo viability time.

In Section 3.11, we present experiments demonstrating that an axisymmetric voltage burst destroys the echo.

Lastly, in Section 3.13, experiments are presented that show echoes of echoes, as well as echoes of spatial harmonics of the wall excitations.

3.2 Echo Wall Signal and Density Perturbation Images

To create the echo, we first excite an azimuthal mode number $m_i = 2$ initial wave using applied voltages to two opposite 60$^{\text{o}}$ wall sectors. The first pulse of Figure 3.1 represents the received wall sector signal of the initial wave, which decays in a few wave periods due to spatial Landau damping. After a chosen time τ, a second $m_s = 4$ wave is excited by applying voltages to four 25$^{\text{o}}$ sectors, each separated by 90$^{\text{o}}$. For the wave excitations, we use either a square pulse with a duration Δt of about one half of a wave period, or a 3-period sinusoidal drive at the appropriate wave frequency. The second visible pulse of Figure 3.1 shows the time at which the second wave is excited, and represents a direct coupling of the second wave excitation to the wall detector. The third wave packet is the received echo, which occurs at $t \simeq 2\tau$ for the mode numbers used here. The peak received initial and echo wall signals are denoted S_i and S_e, respectively.

As mentioned, a special feature of studying echoes in a pure electron plasma is that configuration space is equivalent to phase space. Thus, we directly see the phase mixing (and unmixing) using the CCD camera.

The perturbation images shown in Figure 3.2 are created by subtracting a CCD image of an axisymmetric equilibrium plasma from an image of a perturbed plasma. That is, the density perturbation images represent $\delta n(r, \theta, t) = n(r, \theta, t) - n_o(r)$, where $n_o(r)$ is the profile obtained at $t = 0^-$ with no wall excitation.

The first three perturbation images of Figure 3.2 show the initial $m_i = 2$ wave forming spiral filaments as the perturbation evolves in the sheared background flow. The rotation is in the counter-clockwise direction, and the shear is negative. The images are taken at the times labeled by the letters in Figure 3.1. By Figure 3.2(c), the initial launched wave has effectively damped away.

The $m_s = 4$ wave is excited in Figure 3.2(d), and the remnants of the initial wave are seen as thin filaments. The application of the second wave creates θ-dependent radial drifts of particles, which displaces the initial wave's filaments to new radial positions. The filaments then $\mathbf{E} \times \mathbf{B}$ rotate at a new rate, due to shear in $f_R(r)$. The spiral pattern partially unwinds, resulting in the echo which peaks in Figure 3.2(f). The reverse symmetry between the mixing of Figure 3.2(b) and the unmixing of Figure 3.2(e) is rather striking.

3.2.1 Simple Echo Simulation

A simple echo simulation shows that the radial drifts produced by the second wave enable unmixing. The echo is simulated as a second-order product of density perturbations, which are treated as passive tracers in a sheared flow. The following dimensionless rotation profile is used:

$$\hat{\omega}_R(r) = 1 - r. \tag{3.1}$$

Figure 3.3 shows a contour plot of the density perturbation that is modeled by the following expression:

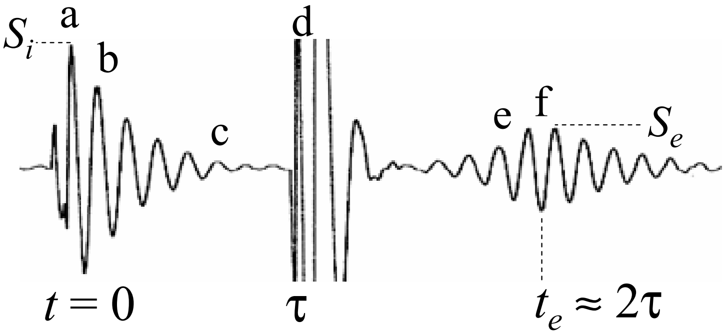

Figure 3.1: Measured wall signal showing initial, second, and echo waves.

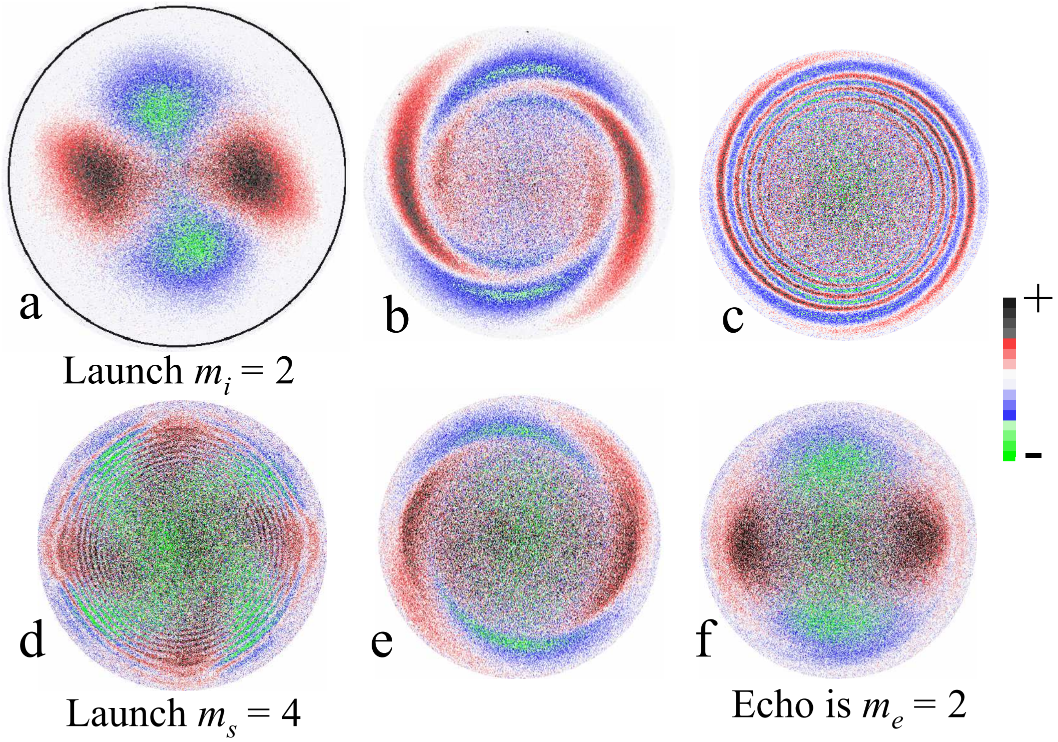

Figure 3.2: Experimental density perturbation images at 6 successive times. The initial wave is excited in figure (a), and the density perturbation executes spiral wind-up as the wave is spatially Landau damped. Figure (d) shows the second wave excitation, and the echo peaks in figure (f).

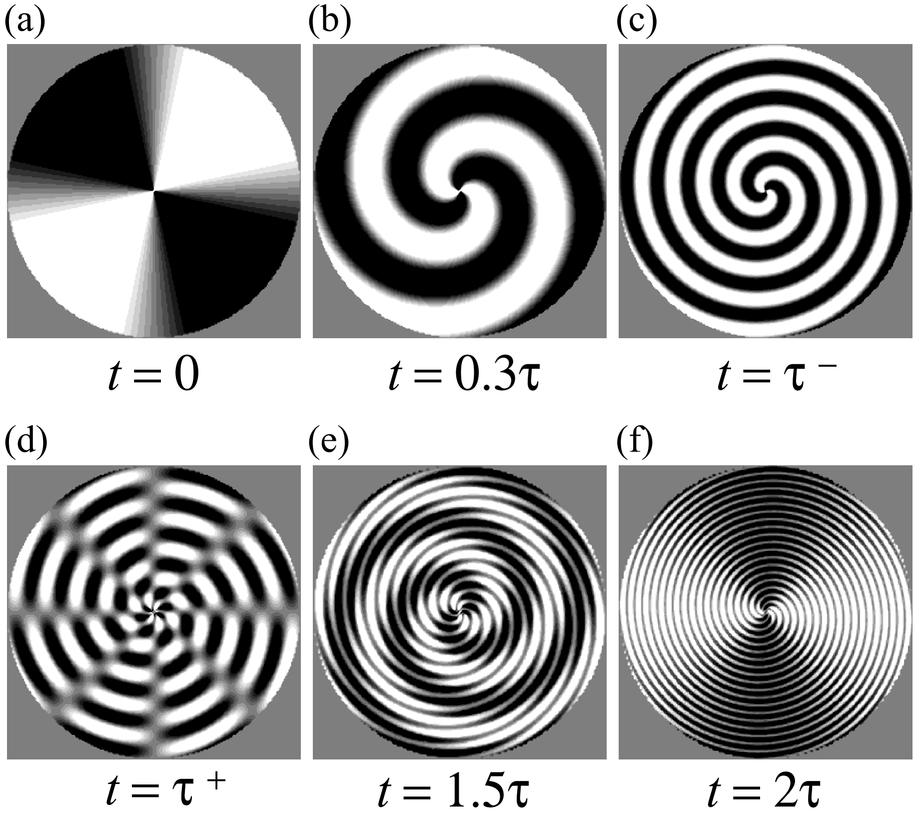

Figure 3.3: Simulated echo. The radial displacements of the density perturbation are shown in Figure (d), immediately after the second perturbation is applied.

$$\delta\hat{n}(r,\theta,t) = \begin{cases} \sin\left[m_i\theta - m_i\hat{\omega}_R\, t\right] & t < \tau \\ \sin\left[m_i\theta - m_i\hat{\omega}_R\, t\right]\, \sin\left[m_s\theta - m_s\hat{\omega}_R\,(t-\tau)\right] & t > \tau. \end{cases} \tag{3.2}$$

For $t < \tau$, the initial $m_i = 2$ density perturbation winds-up with the sheared flow, creating a spiral pattern. The θ-dependent radial displacements $\delta r(\theta)$ created by the second $m_s = 4$ perturbation are seen as discontinuities between adjacent "pie slices" in Figure 3.3(d), immediately after the second perturbation at $t = \tau^+$. This modulated density pattern continues to flow at the rotation rate $\hat{\omega}_R(r)$, and the echo appears at $t = 2\tau$.

3.3 Collisionless Ballistic Echo Theory

Essential features of the echo are captured by a collisionless, ballistic theory [4, 24] that completely neglects collective effects such as waves. We solve for the free-streaming $\mathbf{E} \times \mathbf{B}$ drift trajectories of particles, assuming the particles are acted upon only by impulsively applied wall excitation voltages. The density perturbations are treated merely as passive tracers; thus, the perturbed density does not modify the $\mathbf{E} \times \mathbf{B}$ flow. The approach is fully nonlinear in that it is valid to all orders in the initial and second excitation strengths.

By ignoring collective effects and waves, the theory essentially assumes an infinite wave damping rate γ_m, whereas experiments have $5 < \gamma_m \tau < 100$. Another approximation of the theory is that the time dependence of the applied wall excitations are modeled as delta functions.

These external wall excitations create azimuthal electric fields, which cause radial drifts of particles. The distortion of a circular plasma into an ellipse (the creation of an $m = 2$ diocotron wave), for example, is a direct result of wall-induced θ-dependent radial displacements. The wall excitations also create θ-drifts of particles $\delta\theta$, which will be ignored because they do not cause particles to free-stream at a new rotation rate.

Here, we calculate the electric field at the wall E_w due to a distorted pure electron plasma. The m^{th} Fourier component of the electric potential is

$$\delta\phi_m(r,t) = -e \int_0^{R_w} r' dr' \int_0^{2\pi} d\theta' n(r', \theta', t) G_m(r|r') e^{-im\theta'}, \tag{3.3}$$

where (r', θ') is the source point, and the Green function [20] for the observation point $r > r'$ is given by

$$G_m(r|r') = -\frac{1}{2m} \left(\frac{r'}{r}\right)^m \left[1 - \left(\frac{r}{R_w}\right)^{2m}\right]. \tag{3.4}$$

Following reference [4], we use conservation of particles

$$r'\,dr'\,d\theta' n(r',\theta',t) = r_o\,dr_o\,d\theta_o\,n_o(r_o) \tag{3.5}$$

to express the trajectories in terms of the initial ($t = 0$) coordinates (r_o, θ_o) and unperturbed density $n_o(r_o)$. The electric field at the wall is then

$$E_w \equiv -\frac{\partial \delta\phi_m(r)}{\partial r}\bigg|_{R_w} = e\int_0^{R_w} r_o dr_o \int_0^{2\pi} d\theta_o n_o(r_o)\, g_m[r|r'(r_o,\theta_o,t)]\, e^{-im\,\theta(r_o,\theta_o,t)}, \tag{3.6}$$

where we drop the prime on θ for notational convenience, and the radial derivative of the Green function, evaluated at $r = R_w$, is

$$g_m(r|r') \equiv \frac{\partial G_m(r|r')}{\partial r}\bigg|_{R_w} = \frac{r^m}{R_w^{m+1}}. \tag{3.7}$$

Finding the particle trajectories described by $\theta(r_o, \theta_o, t)$ in the exponential argument of Equation 3.6 is the essence of the theory.

In this collisionless, 2D theory development of the echo wall signal, we use the z-independent Hamiltonian for 2D $\mathbf{E}\times\mathbf{B}$ drift dynamics:

$$H = H_o + \delta H = -e\,\phi_o(r) + \delta H \tag{3.8}$$

where $\phi_o(r)$ is the unperturbed plasma potential that is related to the density by Poisson's equation $\nabla^2\phi_o = -4\pi e n_o$. The perturbed Hamiltonian describes the vacuum potential created by the wall voltages V_i and V_s, and is given by

$$\delta H = eA_i(r)\sin(m_i\theta)\,\delta(t) - eA_s(r)\sin(m_s\theta)\,\delta(t-\tau). \tag{3.9}$$

Here $A_i(r) \equiv k_i V_i \Delta t_i \left(\frac{r}{R_w}\right)^{m_i}$, $A_s(r) \equiv k_s V_s \Delta t_s \left(\frac{r}{R_w}\right)^{m_s}$ represent the r-dependence of the vacuum potentials from the initial and second excitations, where k_i, k_s are the spatial Fourier components of the applied wall voltages, and Δt_i, Δt_s represent the actual durations of the applied excitations.

The angular momentum $p_\theta = eB\,r^2/2c$ is used to express the canonically conjugate variables (p_θ, θ) as (r, θ). The equations of motion are then

$$\begin{aligned}
\frac{\partial \theta}{\partial t} &\equiv \frac{\partial H}{\partial p_\theta} = \frac{c}{eBr}\frac{\partial H}{\partial r} \\
&= \omega_E(r) + \frac{c}{Br}\left[\frac{\partial A_i}{\partial r}\sin(m_i\theta)\delta(t) + \frac{\partial A_s}{\partial r}\sin(m_s\theta)\delta(t-\tau)\right], \qquad (3.10) \\
\frac{\partial r}{\partial t} &= \frac{c}{eBr}\frac{\partial p_\theta}{\partial t} \equiv -\frac{c}{eBr}\frac{\partial H}{\partial \theta} \\
&= \frac{c}{Br}\left[A_i(r)m_i\cos(m_i\theta)\delta(t) - A_s(r)m_s\cos(m_s\theta)\delta(t-\tau)\right], \qquad (3.11)
\end{aligned}$$

where $\omega_E(r) \equiv -\frac{c}{Br}\frac{\partial \phi_o}{\partial r}$ is the $\mathbf{E}\times\mathbf{B}$ rotation rate due to the plasma space-charge electric field. Integrating the equations of motion from $t = 0$ to a time $t < \tau$, before the second wall excitation, gives

$$\theta = \theta_o + \omega_E(r)\,t + \delta\theta_i(\theta_o) \qquad 0 < t < \tau, \qquad (3.12)$$

$$r^2 = r_o^2 + A_i(r)m_i\frac{2c}{B}\cos(m_i\theta_o) \qquad 0 < t < \tau. \qquad (3.13)$$

The impulsive θ-drift from the radial electric field of the initial excitation is given by $\delta\theta_i \equiv \frac{c}{Br}\frac{\partial A_i}{\partial r}\sin(m_i\theta_o)$, and is ignored in the remaining theory. The initial excitation also creates a θ-electric field, causing radial drifts of particles. This radial displacement can be written, to first order, as

$$\delta r_i \equiv r - r_o \simeq \frac{r^2 - r_o^2}{2r} = A_i(r)m_i\frac{c}{Br}e^{im_i[\theta-\omega_E(r)t]} \qquad 0 < t < \tau. \qquad (3.14)$$

The displacement leads to a density perturbation $\delta n = \frac{\partial n_o}{\partial r}\,\delta r$, which we measure directly.

Here we make the distinction between the evolution of diocotron modes and the evolution of a passive tracer:

$$\begin{aligned}
&\text{Mode} \qquad & \delta n(r,\theta,t) &= \delta n_m(r)\,e^{i(m\theta-\omega_m t)}, \\
&\text{Passive Tracer} & &= \delta n_p(r)\,e^{im(\theta-\omega_E(r)\,t)}.
\end{aligned} \qquad (3.15)$$

The ballistic theory ignores modes, and treats the density perturbation as a passive tracer. Experimentally, the modes are strongly damped, which gives the theory applicability to the data.

Integrating Equation 3.10 and Equation 3.11 from $t = \tau$ to a time $t > \tau$, after the second wall excitation, i.e., when the echo appears, gives

$$\begin{aligned} \theta &= \theta(\tau) + \omega_E[r(\tau^+)]\,(t-\tau), + \delta\theta_s[\theta(\tau)] && t > \tau \qquad (3.16) \\ r^2 &= r_o^2 + A_i(r) m_i \frac{2c}{B}\cos(m_i\theta_o) - A_s(r) m_s \frac{2c}{B}\cos\left(m_s\theta(\tau)\right) && t > \tau, \qquad (3.17) \end{aligned}$$

where $t = \tau^+$ is the time immediately after the second excitation. The radial displacements caused by the second wall excitation, applied at $t = \tau$, are given by Equation 3.17. Particles displaced to a new radial position $r(\tau^+)$ rotate at the new rate $\omega_E[r(\tau^+)]$, enabling unmixing.

Neglecting the impulsive θ-drifts $\delta\theta_i$ and $\delta\theta_s$, and using Equation 3.12 and Equation 3.13, we evaluate $\theta(\tau)$ as

$$\begin{aligned} \theta(\tau) &= \theta_o + \omega_E\left[r_o + \frac{c}{Br} m_i A_i(r)\cos(m_i\theta_o)\right]\tau \qquad (3.18) \\ &\simeq \theta_o + \omega_E(r_o)\,\tau + \frac{c}{Br}\left.\frac{\partial\omega_E}{\partial r}\right|_{r_o} A_i(r) m_i \cos(m_i\theta_o)\,\tau, \end{aligned}$$

where ω_E is Taylor expanded in the last line. Similarly, the term $\omega_E[r(\tau^+)]$ in Equation 3.16 is Taylor expanded. The particle θ-trajectories of Equation 3.16 are then

$$\begin{aligned} \theta(r_o,\theta_o,t) = \theta_o &+ \omega_E(r_o)\,t + \frac{c}{Br}\left.\frac{\partial\omega_E}{\partial r}\right|_{r_o} A_i(r) m_i \cos(m_i\theta_o)\,t - \\ &(t-\tau)\frac{c}{Br}\left.\frac{\partial\omega_E}{\partial r}\right|_{r_o} A_s(r) m_s \times \\ &\cos\left[m_s\theta_o + m_s\omega_E(r_o)\,\tau + \frac{c}{Br}\left.\frac{\partial\omega_E}{\partial r}\right|_{r_o} A_i(r) m_i m_s \cos(m_i\theta_o)\,\tau\right]. \qquad (3.19) \end{aligned}$$

This expression for $\theta(r_o, \theta_o, t)$ is used to evaluate the electric field at the wall, given by Equation 3.6.

We make use of the exponential expansion

$$e^{-ia\cos x} = \sum_l (-i)^l J_l(a) e^{-ilx}, \tag{3.20}$$

where J_l is the Bessel function of the first kind of order l, and find that the electric field at the wall vanishes unless $m = q\,m_s - p\,m_i$. Here, p and q are the harmonic orders of the initial and second excitations, respectively, similar to l in Equation 3.20.

For the lowest harmonic numbers $p = q = 1$, the echo mode number is predicted to be

$$m_e = m_s - m_i. \tag{3.21}$$

Experiments agree with this expression for all mode numbers used, and no echo is seen if $m_i > m_s$.

Furthermore, we use the Bessel function identity

$$J_p(c-d) = \sum_s J_{p+s}(c) J_s(d), \tag{3.22}$$

and calculate the following collisionless ballistic theory prediction for the electric field at the wall, for $t > \tau$:

$$E_w(t) = e \int_0^{R_w} r\,dr\,n_o(r)\,g_m(r|r')\,\exp\left[-im_e\omega_E(r)\left(t - \tau\frac{m_s}{m_e}\right)\right] \times$$
$$J_1\left[\frac{c}{Br}\frac{\partial\omega_E}{\partial r}A_i(r)m_i m_e\left(t - \tau\frac{m_s}{m_e}\right)\right] J_1\left[\frac{c}{Br}\frac{\partial\omega_E}{\partial r}A_s(r)m_s m_e\left(t-\tau\right)\right], \tag{3.23}$$

where we have dropped the subscript on r for notational convenience.

3.3.1 Time of Echo Appearance

Equation 3.23 predicts the time of the echo appearance, which is obtained by setting the phase mixing terms to zero. In the experiments, phase mixing is the spiral wind-up of the density perturbation, creating radial ripples of δn. The unique time at which the ripples vanish is found by setting the r-dependent terms in the exponential argument to zero, yielding the echo appearance time

$$t_e = \tau \frac{m_s}{m_s - m_i}. \tag{3.24}$$

We find that the observed time of the echo appearance corresponds to the above prediction for t_e. Figure 3.4 shows the measured value of t_e versus the second wave launch time τ, both normalized to the $m = 2$ wave period T_2. The dashed lines are the theory predictions, and the initial, second, and echo mode numbers are shown in parentheses. The case with $m_i = 2$ and $m_s = 4$ has the largest data range due to the large signal-to-noise ratio for the echo amplitude.

Interestingly, no echo is seen if the initial, second, or attempted echo mode number is $m = 1$. We speculate this is due to the impossibility of spatial Landau damping for the center-of-mass mode, since the critical radius r_c is at the wall, where the density $n = 0$. The absence of an $m = 1$ echo observation, however, contradicts the simple ballistic theory, which completely neglects collective resonant effects.

Figure 3.5 shows the measured wall signal from an $m_i = 2$, $m_s = 5$, $m_e = 3$ echo sequence, using resonant drives for the initial and second waves, and one sector of S7 as the detection antenna. Figure 3.6 shows the density perturbation images at the 6 times labeled in Figure 3.5. These images are created using the same method as in Figure 3.2, by subtracting an image of the unperturbed density profile taken at $t = 0^-$ from an image of the perturbed plasma at $t > 0$.

At $t = 0$, a 5-period sinusoidal drive at $f_i = 94$ kHz $\simeq f_2$ is applied to two opposite S4 wall sectors. Figure 3.6(a) corresponds to the peak $m_i = 2$ amplitude at the end of the external excitation, and images (b) and (c) show the

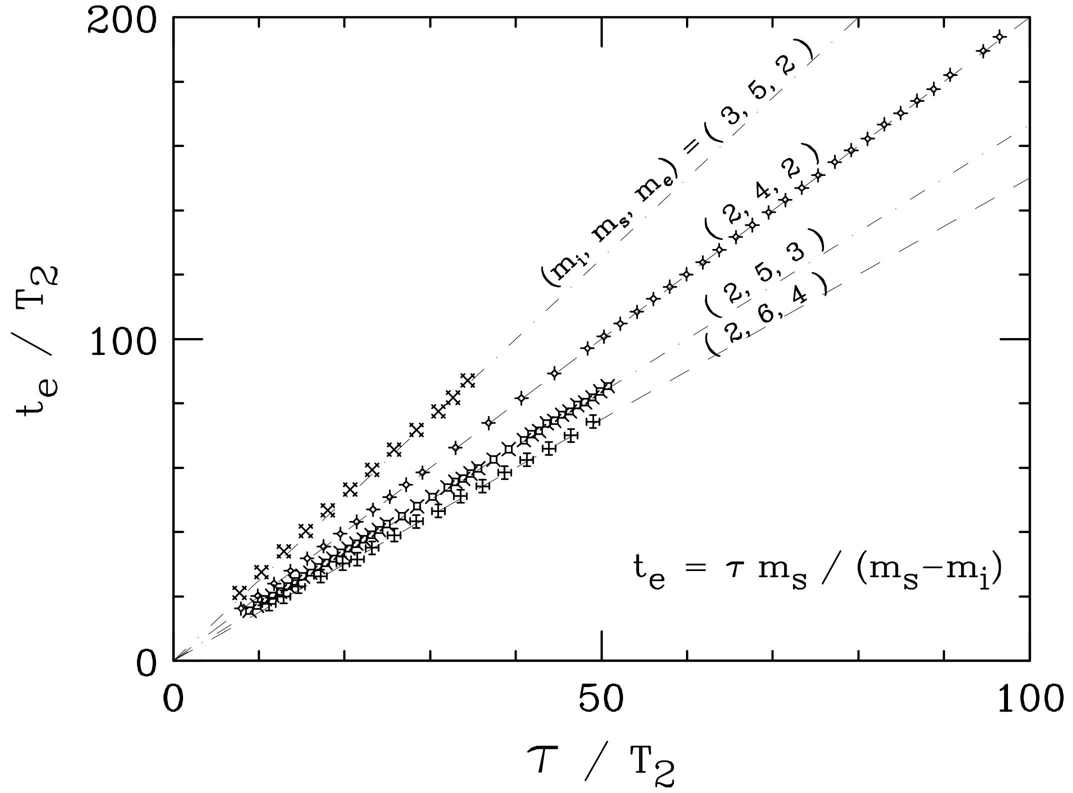

Figure 3.4: Echo appearance time t_e versus the second wave launch time τ, both normalized to the $m = 2$ wave period T_2, using various mode numbers.

initial wave phase mixing. At $t = 0.2$ ms $\equiv \tau$, a 5-period sinusoidal drive at $f_s = 220$ kHz $\simeq f_5$ is applied to a single S7 wall sector. Image (d) shows the peak $m_s = 5$ density perturbation, and image (e) shows the modulated phase mixed density perturbation. The echo peaks in image (f) at $t = 0.342$ ms $\simeq \tau m_s/m_e = \tau\, 5/3$, with mode number $m_e = 3$. The measured frequency of the echo signal is $f_e = 134$ kHz.

The $m = 2$ critical layer (the range of radii over which the density perturbation executes spiral wind-up) is narrower here than the critical layer of an $m = 2$ wave excited by a square pulse, as in Figure 3.2(b), even though the density profiles are similar. This is due to the broader range of frequencies that comprises a square pulse, compared to the nearly pure spectral content of a 5-period sinusoidal drive.

3.3.2 Simple Collisionless Prediction

To further compare the collisionless theory with experiments, we evaluate Equation 3.23 near the echo appearance time t_e, and write the "no collision" theory prediction for the peak echo wall signal as

$$S_e^{nc} \equiv GE_w(t \approx t_e) = \alpha V_i J_1(\beta V_s \tau). \tag{3.25}$$

The gain is given by $G \equiv (A/C)\tilde{G}$, where A is the area and C is the capacitance of the detection sectors, and where $\tilde{G}$ is the amplifier gain. Here, the initial and second excitations A_i, A_s are represented by the applied wall voltages V_i, V_s; and the couplings $k_i \Delta t_i$, $k_s \Delta t_s$ are absorbed into α and β.

Equation 3.25 follows from Equation 3.23 because at $t \approx t_e$, the Bessel function argument in Equation 3.23 containing the *initial* perturbation amplitude is extremely small, and $J_1(x) \approx x/2$ for small x. The Bessel function argument which contains the *second* perturbation amplitude is large at the time of the echo appearance, so this Bessel function is not expanded. Theoretically, at $t = t_e$, the echo wall signal is zero, since $J_1(0) = 0$.

Stated explicitly,

$$\begin{aligned} \alpha &\equiv Gk_i\Delta t_i \, \epsilon \frac{ec\, m_i m_e}{2BR_w^{m_i+3}} \int_0^{R_w} dr r^{m_i+2} n_o(r) \frac{\partial \omega_E}{\partial r} \\ &\equiv \alpha' \int_0^{R_w} dr\, r^{m_i+2} n_o(r) \frac{\partial \omega_E}{\partial r}, \end{aligned} \tag{3.26}$$

$$\beta \equiv k_s \Delta t_s \, m_i m_s \frac{c}{Br} \left(\frac{r}{R_w} \right)^{m_s} \frac{\partial \omega_E}{\partial r} \equiv \beta' \, r^{m_s - 1} \frac{\partial \omega_E}{\partial r}, \tag{3.27}$$

where ϵ represents the difference between the theoretical echo appearance time t_e and the measurement time. This measurement time is defined as the time of the

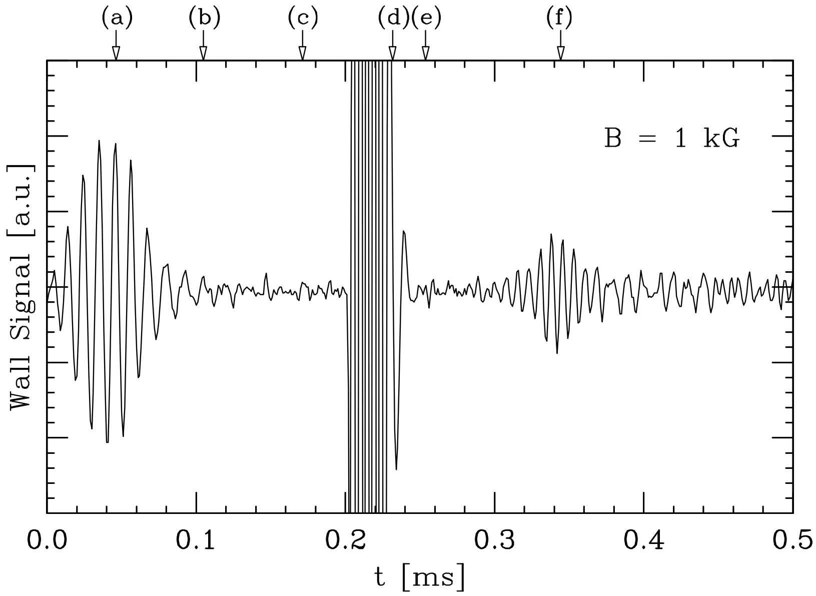

Figure 3.5: Measured wall signal of an $m_i = 2$, $m_s = 5$, $m_e = 3$ echo sequence using one sector of S7 as the detection antenna.

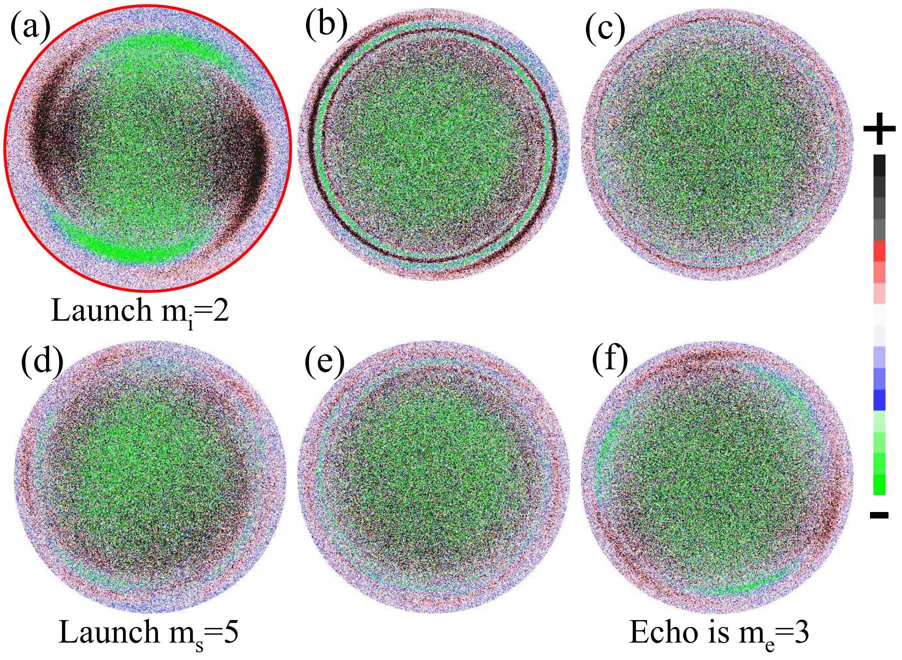

Figure 3.6: Density perturbation images at the six times labeled in Figure 3.5. The red circle in image (a) shows the wall radius.

maximal echo wall signal, and is typically within 1 or 2 plasma rotation periods of t_e. The terms α' and β' are defined here and will appear later in a collisional theory, described in Section 3.5.2.

3.3.3 Asymmetric Roles of Initial and Second Waves

We test the asymmetry in the roles of the initial and second perturbations predicted by Equation 3.25, and find that data quantitatively agree with theory for small values of V_i and V_s.

Figure 3.7 shows that the peak measured echo signal S_e is linearly proportional to the initial excitation voltage V_i, until nonlinear wave trapping effects are observed. The initial wave peak amplitude S_i (diamonds) is observed to be proportional to V_i as expected.

Large initial wave amplitudes cause particle-trapping in the initial wave perturbation, forming Kelvin's "cat's eyes" [16, 25]. The resulting nonlinear trapping oscillations [26] are explicitly seen on the wall signal for $V_i \gtrsim 4$ V. A finite but undetectable level of particle trapping by the wave may exist at lower amplitudes, and is presumably responsible for the departure from the observed linear dependence of S_e on V_i at $V_i \gtrsim 2$ V. In the echo experiments presented in this thesis, we intentionally limit V_i in an effort to keep the initial wave damping in the linear regime.

The maximal echo signal is generally a significant fraction of the initial wave amplitude; in Figure 3.7, the echo amplitude S_e is slightly less than 1/2 of the initial wave amplitude S_i. When the second wave is launched at a time τ that maximizes the echo amplitude, we observe a nearly complete initial wave reconstruction, with $S_e/S_i = 0.7$.

Figure 3.8 shows the measured S_e versus the second excitation strength V_s,

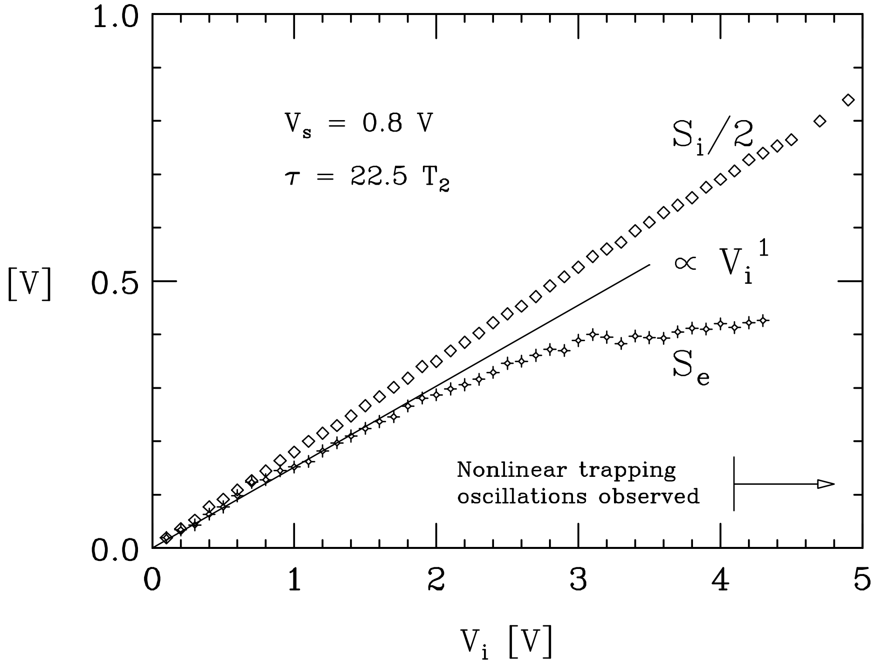

Figure 3.7: The peak initial wave and echo wave wall signals, S_i and S_e respectively, versus the initial wave excitation voltage V_i. The solid line is the theory prediction $S_e \propto V_i$.

for fixed values of V_i and τ. The star points are data, and the line is a fit to the peak of the data using Equation 3.25, with α and β as fitting parameters. At small values of the product $V_s\tau$, the measured echo wall signal increases roughly linearly with V_s, in agreement with a second-order echo theory.

For larger values of V_s, in this case just under 1 volt, S_e "saturates" and decreases. This saturation effect, predicted by Equation 3.25, is caused by second-wave-induced radial drifts that are larger than optimal for the given τ, resulting in an incomplete initial wave unwinding.

3.4 End-field θ-smearing

The trap's end confinement fields create $\mathbf{E} \times \mathbf{B}$ drifts in the θ-direction, providing an additional rotation $\omega_{end}(r, v_z)$ which adds to the plasma space charge

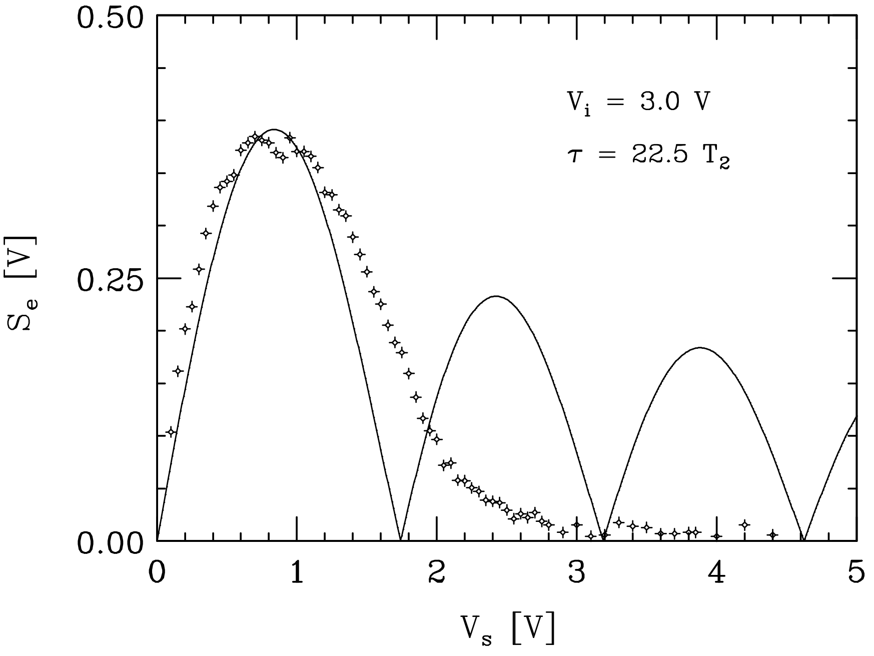

Figure 3.8: The peak echo wall signal versus the second wave excitation voltage V_s. The disagreement between the data and the theory prediction (solid line) at large second wave excitations is not understood.

$\mathbf{E} \times \mathbf{B}$ rotation $\omega_E(r)$. The resulting θ-shift for a particle depends on the particle's end-residence time, and hence on the particle's z-velocity v_z. This finite-length effect, which we call "θ-smearing," breaks the 2D ideal fluid/nonneutral plasma isomorphism [9], and one might expect that end effects would destroy the echo. We find, however, that in the absence of collisions, θ-smearing alone does not destroy the echo.

Consider a plasma with curved ends, that is, with plasma length $L(r, v_z)$. Figure 3.9 schematically depicts a finite length plasma, and shows the guiding center of an electron bouncing off one end. In the experimental ranges of density and temperature, the Debye length is small ($\lambda_D < R_p$), and the guiding center experiences a quasi-impulsive kick normal to the plasma end sheath. This kick contains a radial electric field component from the end confinement voltage, causing

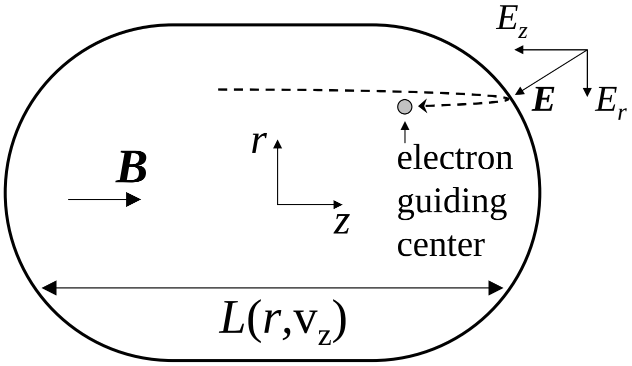

Figure 3.9: Schematic of a finite length plasma. The guiding center of the electron bounces off the end of the plasma and experiences a radial component of the confinement field, resulting in $\mathbf{E} \times \mathbf{B}$ drifts in the θ-direction.

the electron to $\mathbf{E} \times \mathbf{B}$ drift in the θ-direction.

The radial impulse an electron experiences depends on its axial velocity v_z, so we write the total bounce-averaged rotation frequency, neglecting the (small) diamagnetic drifts, as

$$\omega_R(r, v_z) = \omega_E(r) + \omega_{end}(r, v_z), \tag{3.28}$$

where $\omega_E(r)$ is the $\mathbf{E} \times \mathbf{B}$ rotation frequency from the plasma space charge, and $\omega_{end}(r, v_z)$ is the θ-smearing effect.

To find the magnitude of θ-smearing, it is convenient to work with the bounce-action

$$I \equiv \frac{1}{2\pi} \oint p_z dz \approx \frac{p_z}{\pi} L(r, v_z), \tag{3.29}$$

where $p_z \equiv \mathrm{m} v_z$ is the electron z-momentum. The unperturbed Hamiltonian, including z-dynamics, is then

$$H_z = \frac{p_z^2}{2\mathrm{m}} - e\phi_o(r, z) = \frac{\pi^2 I^2}{2\mathrm{m} L^2(r, v_z)} - e\phi_o(r, z). \tag{3.30}$$

The bounce-averaged rotation frequency is found from the θ equation of motion:

$$\omega_R(r, v_z) \equiv \frac{\partial \theta}{\partial t} \equiv \frac{\partial H_z}{\partial p_\theta} = \frac{c}{eBr}\frac{\partial H_z}{\partial r} = -\frac{c}{Br}\frac{\partial \phi_o}{\partial r} - \frac{c}{eBr}\frac{\pi^2 I^2}{\mathrm{m}L^3}\frac{\partial L}{\partial r} \equiv \omega_E(r) + \omega_{end}(r, v_z). \tag{3.31}$$

The end-field θ-smearing contribution to the rotation frequency is then

$$\omega_{end}(r, v_z) = -\frac{v_z^2}{\Omega_c L\, r}\frac{\partial L}{\partial r}. \tag{3.32}$$

A more physical argument leading to the same result is found in reference [27].

From Equation 3.32, we find that end θ-smearing causes v_z-dependent phase mixing of particles. In the absence of collisions or other randomizing effects, however, each particle remains in its original velocity class, which executes its own spiral wind-up (and unwinding). The second wave reverses the effects of $\omega_{end}(r, v_z)$, in the same fashion as it reverses the effects of $\omega_E(r)$. Thus, θ-smearing alone does not destroy the echo.

3.5 Collisional Irreversibility of θ-smearing

At late times, the echo no longer appears. In this section, we develop a second-order theory that describes the collisional irreversibility of θ-smearing. This result is combined with the fully nonlinear, collisionless theory described in Section 3.3. We compare experiments to the collisional theory, and find that collisions acting on the end-field θ-smearing cause an unavoidable, "baseline" degradation of the echo in a time of 100 to 200 wave periods.

3.5.1 Collisional Theory

The theoretical effects of collisions are found by solving the Boltzmann equation to second order, using a Fokker Planck collision operator that models small angle Coulomb collisions.

The wall excitations are modeled as impulsively applied, similar to the collisionless theory. The Hamiltonian H' used for the collisional case, however, includes z-dynamics, and is

$$H' = H_z + \delta H' \tag{3.33}$$

where the unperturbed Hamiltonian H_z is given by Equation 3.30, and the wall excitations are given by

$$\delta H' = eA_i(r)e^{im_i\theta}\delta(t) + eA_s(r)e^{-im_s\theta}\delta(t-\tau). \tag{3.34}$$

The Boltzmann equation that describes collisions acting on the particle distribution function $f(r, v_z, t)$ is

$$\frac{\partial f}{\partial t} + [f, H'] = \nu\,\bar{v}^2\frac{\partial^2 f}{\partial v_z^2}, \tag{3.35}$$

where ν represents the electron-electron parallel scattering rate [28], given by

$$\nu_\| \equiv 2.8\sqrt{\pi}\,n\,\bar{v}\,b^2\,\ln\left(r_L/b\right). \tag{3.36}$$

Here, $r_L \equiv \bar{v}/\Omega_c$ is the cyclotron radius and $b \equiv e^2/T$ is the distance of closest approach for thermal electrons.

In the collisional theory development, we define

$$\nu \equiv \nu_{\text{eff}}\,\frac{n(r)}{n(0)}\left(\varepsilon_z/T\right)^{-1}, \tag{3.37}$$

where $\varepsilon_z \equiv \mathrm{m}v_z^2/2$ is the electron kinetic energy. This allows us to directly obtain an effective electron-electron collision rate ν_{eff} from the echo data. We then compare ν_{eff} with the actual electron-electron collision rate $\nu_\|$ to test the validity of the collisional theory in describing echo destruction.

The Poisson brackets in Equation 3.35 are shorthand for the following operation:

$$[a, b] \equiv \frac{\partial a}{\partial \theta}\frac{\partial b}{\partial p_\theta} - \frac{\partial a}{\partial p_\theta}\frac{\partial b}{\partial \theta}. \tag{3.38}$$

In addition, we use $p_\theta = \frac{eB}{2c}r^2$, similar to the collisionless theory, to express p_θ in terms of r.

The evolution of the perturbed distribution function δf can then be written

$$\frac{\partial \delta f}{\partial t} + \frac{\partial \delta f}{\partial \theta}\omega_R(r, v_z) - \frac{c}{eBr}\frac{\partial f_M}{\partial r}\frac{\partial \delta H'}{\partial \theta} = \nu\,\bar{v}^2\frac{\partial^2 \delta f}{\partial v_z^2}, \tag{3.39}$$

where $\omega_R(r, v_z)$ is given by Equation 3.31, and includes the θ-smearing effect. $\frac{\partial f_M}{\partial r}$ is the radial derivative of the unperturbed distribution function, given by $\frac{\partial f_M}{\partial r} \equiv \frac{1}{\sqrt{2\pi\bar{v}^2}}\frac{\partial n_o}{\partial r}\exp[-\varepsilon_z/T]$.

For $t < \tau$, the first-order solution from the initial excitation only is

$$\begin{aligned}\delta f_i^{(1)} &= -im_iA_i\frac{c}{eBr}\frac{\partial f_M}{\partial r} \\ &\quad\cdot\exp\left[-im_i\theta + im_i\omega_E(r)t - \frac{im_iv_z^2}{\Omega_cLr}\frac{\partial L}{\partial r}t - \nu\frac{4}{3}\frac{m_i^2v_z^2\bar{v}^2}{\Omega_c^2L^2r^2}\left(\frac{\partial L}{\partial r}\right)^2t^3\right],\end{aligned} \tag{3.40}$$

where $im_i\omega_R(r, v_z)t$ is written as the second and third terms in the exponential argument. In obtaining Equation 3.40, we have made the approximation $\frac{\partial^2}{\partial v_z^2}\delta f \simeq \frac{1}{\delta f}\left(\frac{\partial}{\partial v_z}\delta f\right)^2$. The rather strange t^3 scaling of the collisional term in the exponent comes from the collision operator $\nu\bar{v}^2\frac{\partial^2}{\partial v_z^2}$ acting on δf, which has the v_z-dependent θ-smearing effect in $\omega_R(r, v_z)$. This brings down t^2, and the integral $\nu\bar{v}\int_0^t dt'\frac{\partial^2\delta f}{\partial v_z^2}$ then yields t^3.

For $t > \tau$, we solve the Boltzmann equation to second order, using

$$\frac{\partial \delta f}{\partial t} + [\delta f, H_z] + [\delta f_i^{(1)}, \delta H'] = \nu\,\bar{v}^2\frac{\partial^2 \delta f}{\partial v_z^2}. \tag{3.41}$$

The second Poisson bracket describes the modulation of the initial wind-up $\delta f_i^{(1)}$ by the second wall excitation in $\delta H'$, and produces the echo.

Keeping only terms containing the first power of ν, the second-order perturbed distribution function at $t > \tau$ is

$$\delta f^{(2)}(t) = im_i^2m_s\left(\frac{c}{Br}\right)^2\frac{\partial \omega_E}{\partial r}\frac{\partial f_M}{\partial r}A_iA_s\tau\,\exp\left[im_e\theta - i\omega_R(r, v_z)m_e\left(t - \frac{\tau m_s}{m_e}\right)\right]$$

$$\cdot \exp\left\{-\nu \frac{4v_z^2\bar{v}^2}{\Omega_c^2 L^2 r^2}\left(\frac{\partial L}{\partial r}\right)^2\left[\frac{m_i^2\tau^3}{3}+\frac{m_e^2(t-\tau)^3}{3}+m_i^2\tau^2(t-\tau)-m_i m_e\tau(t-\tau)^2\right]\right\}. \tag{3.42}$$

Again, the time of the echo appearance t_e is obtained by setting the r-dependent (phase mixing) terms in the first exponential argument equal to zero. At time $t = t_e \equiv \tau\frac{m_s}{m_e}$, the second-order collisional solution for the peak echo amplitude is

$$\delta f^{(2)}(t_e) = i m_i^2\, m_s \left(\frac{c}{Br}\right)^2 \frac{\partial\omega_E}{\partial r}\frac{\partial f_M}{\partial r} A_i A_s\, \tau\, \exp\left(i m_e \theta\right)\, \exp\left[-\gamma^3(\nu_{\text{eff}}, r, \varepsilon_z)\,\tau^3\right], \tag{3.43}$$

where the collisional damping term is given by

$$\gamma^3(\nu_{\text{eff}}, r, \varepsilon_z) \;\equiv\; \nu_{\text{eff}}\, \frac{n(r)}{n(0)}\left(\frac{\varepsilon_z}{T}\right)^{-1} \varepsilon_z\, T \left(\frac{c}{eBr}\right)^2\left(\frac{1}{L}\frac{\partial L}{\partial r}\right)^2 \frac{8}{3}\frac{m_i^2\, m_s}{m_e}. \tag{3.44}$$

Here, we have used Equation 3.37. The ε_z dependence is in the plasma length $L(r, \varepsilon_z)$, defined by the electron end reflection at $L/2$, i.e.,

$$e\phi(L/2, r) - e\phi(z = 0, r) = \varepsilon_z. \tag{3.45}$$

Finally, we combine the collisionless, fully nonlinear result of Equation 3.23 with the collisional, second-order result of Equation 3.43, and obtain

$$\begin{aligned} E_w|_{t\simeq t_e} \;&=\; \frac{ec}{2B} m_i m_e \epsilon \int_0^{R_w} dr A_i(r) \frac{r^3}{R_w^3}\frac{\partial \omega_E}{\partial r}\frac{\partial n_o}{\partial r} J_1\left(\frac{c}{Br}\frac{\partial\omega_E}{\partial r} m_i m_s A_s(r)\,\tau\right) \times \\ &\frac{1}{2\sqrt{\pi T}}\int_0^\infty \frac{d\varepsilon_z}{\sqrt{\varepsilon_z}}\, \exp\left[-\varepsilon_z/T - \gamma^3(\nu_{\text{eff}}, r, \varepsilon_z)\,\tau^3\right]. \end{aligned} \tag{3.46}$$

The $1/\sqrt{\varepsilon_z}$ term arises from changing a velocity integral $\delta n = \int dv\, \delta f$ to an energy integral $\delta n = \int d\varepsilon_z\, \delta f/\sqrt{2\mathrm{m}\varepsilon_\mathrm{z}}$.

3.5.2 Comparison with Experiments

To compare with experiments, we numerically evaluate the double integral in Equation 3.46. Using the measured z-integrated density from a CCD image and known plasma confinement geometry and voltages, a 2D Poisson solver [29] calculates the local density $n(r, z)$ and potential $\phi(r, z)$. To obtain the solution, local thermal equilibrium is presumed at every r and z. The plasma length $L(r, \varepsilon_z)$ is then calculated from Equation 3.45, and the plasma rotation frequency is calculated from $\omega_E(r) \equiv -\frac{c}{Br}\frac{\partial\phi(r)}{\partial r}$, at $z = 0$.

Equation 3.46 can be written as the following collisional prediction for the peak echo wall signal, near the echo appearance time:

$$\begin{aligned} S_e^{col} &= \alpha' \, V_i \int_0^{R_w} dr \, r^{m_i+3} \frac{\partial \omega_E}{\partial r} \frac{\partial n_o}{\partial r} J_1\left(\beta' \, r^{m_s-1} \frac{\partial \omega_E}{\partial r} \, V_s \, \tau\right) \times \\ & \frac{1}{2\sqrt{\pi T}} \int_0^\infty \frac{d\varepsilon_z}{\sqrt{\varepsilon_z}} \exp\left[-\varepsilon_z/T - \gamma^3(\nu_{\text{eff}}, r, \varepsilon_z) \, \tau^3\right], \end{aligned} \tag{3.47}$$

where α' and β' are given by Equation 3.26 and Equation 3.27, re-written here as

$$\alpha' \equiv G k_i \Delta t_i \, \epsilon \frac{ec \, m_i m_e}{2BR_w^{m_i+3}} \tag{3.48}$$

$$\beta' \equiv k_s \Delta t_s \, m_i m_s \frac{c}{BR_w^{m_s}}. \tag{3.49}$$

We obtain an effective electron-electron collision rate ν_{eff} by fitting the theory expression for S_e^{col} to data sets of the measured peak echo wall signal versus τ, with ν_{eff}, α', and β' as fitting parameters.

Figure 3.10 shows data of the measured peak echo wall signal S_e versus the second wave launch time τ. The solid line is the fit of the collisional theory of Equation 3.47 with $\nu_{\text{eff}} = 31$ sec^{-1}. For the weak second wave excitation used here ($V_s = 0.25$ V), the value of ν_{eff} is fairly close to the electron-electron scattering rate of $\nu_{\|} = 21$ sec^{-1}. The result of a simplified approach, described later in

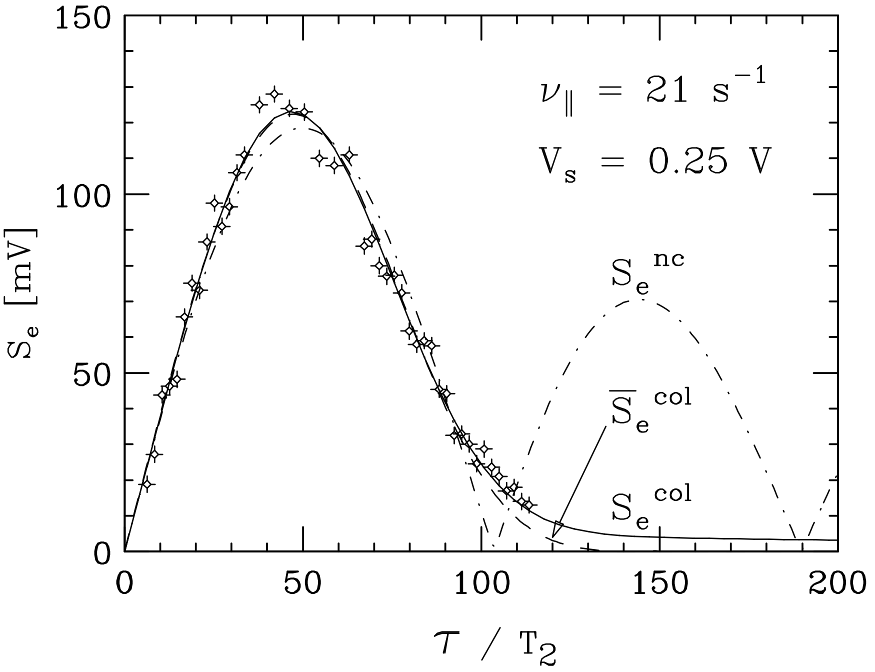

Figure 3.10: Measured peak echo wall signal S_e versus the second wave launch time τ. The solid line shows the fit from numerically integrating the collisional theory expression of Equation 3.47. The dot-dashed line is obtained from the collisionless theory of Equation 3.25, and the dashed line is obtained from the simple collisional expression of Equation 3.54.

Section 3.5.3, is shown as a dashed line, and the fit yields $\bar{\nu}_{\text{eff}} = 4\ \text{sec}^{-1}$. The fit obtained from the simple collisionless theory of Equation 3.25 is also shown as the dot-dash line, and does not accurately describe the data at late times.

At early times, S_e increases approximately linearly with τ, as predicted by second-order perturbation theory. At intermediate times, the measured S_e exhibits the saturation effect predicted by the (second wave Bessel function in the) fully nonlinear collisionless theory. At late times, the cumulative effect of collisional velocity scattering, combined with end-field θ-smearing, can destroy the echo. In addition, we find that large excitation amplitudes can destroy the echo up to 5× faster than collisions.

Figure 3.11 summarizes the comparison between the collisional theory and echo data. The vertical axis is the experimentally determined v_z-scattering rate ν_{eff}, obtained from fits to 65 data sets such as Figure 3.10. The horizontal axis is the electron-electron collision rate $\nu_{\|}$ for the specific plasma parameters, given by Equation 3.36, where we use the characteristic density $n(r_c)$ near the critical radius r_c.

In Figure 3.11, the strength of the plasma perturbation A_s from the second wall excitation is represented by the size of the data symbol, with larger symbols corresponding to larger second excitation strengths. At a given value of $\nu_{\|}$, identical symbols of different sizes correspond to identical plasma parameters, but with different values of the second wave excitation strength. The strength of A_s is varied over a factor of 50 in the data plotted here. The arrow identifies the data point corresponding to Figure 3.10.

Figure 3.11 shows that the echo lifetime is limited by collisional irreversibility of end-field θ-smearing when the second wave excitation is sufficiently small; it also shows that the echo can be used to measure the electron-electron collision rate. At large second wave amplitudes, a different (unknown) effect destroys the echo as effectively as collisions enhanced by 100×.

Note that the large variations in ν_{eff} translate into much smaller variations in the time of echo destruction, because of the τ^3 scaling in the collisional exponential decay argument in Equation 3.46. Thus, a factor of 100 enhancement in ν_{eff} gives only a 4.6× reduction in the echo viability time.

3.5.3 Simple Approach

One simple alternative to the previous analysis of collisional echo destruction consists of approximating the integrands in Equation 3.47 as constant; thus, we approximate the electron energy here as $\varepsilon_z \simeq \bar{\varepsilon}_z \equiv T$. The collisonal damping

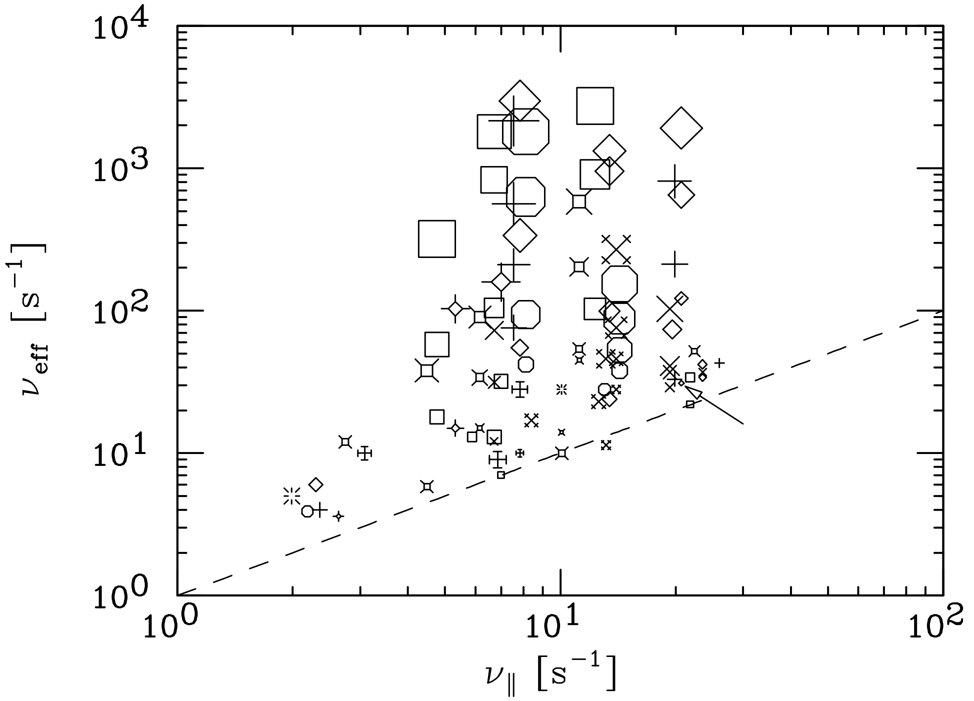

Figure 3.11: Echo data showing the measured effective electron-electron collision rate $\nu_{\rm eff}$, versus calculated electron-electron collision rate $\nu_\parallel$. The size of the data symbols represents the strength of the second wave perturbation.

terms in γ^3, described by Equation 3.44, can then be approximated as

$$\frac{c}{eBr}\frac{T}{L}\frac{\partial L}{\partial r} \approx \omega_E(0)\frac{T}{\Delta\phi}\frac{\Delta L}{L_p} \approx \omega_E(0)\left(\frac{\lambda_D}{R_p}\right)^2\frac{\Delta L}{L_p}, \tag{3.50}$$

where $\lambda_D \equiv \sqrt{T/4\pi n e^2}$ is the Debye length. Here the end curvature is rather crudely defined as

$$\Delta L \equiv \left.\frac{\partial L}{\partial r}\right|_{r_c}\Delta r_c \equiv \left.\frac{\partial L}{\partial r}\right|_{r_c}\gamma_2\left(\left.\frac{\partial \omega_E}{\partial r}\right|_{r_c}\right)^{-1}, \tag{3.51}$$

where Δr_c is the critical layer for the $m = 2$ diocotron wave, and γ_2 is the $m = 2$ diocotron wave damping rate. In addition, the plasma length is defined as

$$L_p \equiv L(r = 0, \varepsilon_z = T). \tag{3.52}$$

The simplifed collisional damping term is then

$$\bar{\gamma}^3(\bar{\nu}_{\text{eff}}) \equiv \bar{\nu}_{\text{eff}}\, \omega_E^2(0) \left(\frac{\lambda_D}{R_p}\right)^4 \left(\frac{\Delta L}{L_p}\right)^2 \frac{4}{3} \frac{m_i^2\, m_s}{m_e}, \tag{3.53}$$

and this approach yields the following simplified collisional expression for the peak echo wall signal, near the echo appearance time:

$$\bar{S}_e^{\,col} \equiv \alpha V_i\, J_1(\beta V_s \tau)\, e^{-\bar{\gamma}^3 \tau^3}, \tag{3.54}$$

where α and β are given by Equation 3.26 and Equation 3.27, and the integrand in α is treated as constant.

Figure 3.12 shows the effective electron-electron scattering rate $\bar{\nu}_{\text{eff}}$ obtained from the simplified approach of Equation 3.54. Each symbol is obtained from a fit to a data set of $S_e(\tau)$ as in Figure 3.10, with α, β, and $\bar{\gamma}^3$ used as fitting parameters, and $\bar{\nu}_{\text{eff}}$ is then obtained from Equation 3.53. Again, the size of the symbols represents the strength of the second excitation. Using this simple analysis, we see general correspondence (within a factor of 10 in $\bar{\nu}_{\text{eff}}$ for small second wave excitations) between the theory and data. However, the plot shows that the more thorough analysis used to obtain Figure 3.11 (i.e., evaluating the r and ε_z integrals) is necessary for a quantitative study of collisions using the echo.

We define here the collisional echo destruction time t_c, obtained from $\bar{\gamma}^3(\nu_{\|})\, t_c^3 = 1$, as

$$t_c \equiv \nu_{\|}^{-1/3}\, \omega_E(0)^{-2/3} \left(\frac{\lambda_D}{R_p}\right)^{-4/3} \left(\frac{\Delta L}{L_p}\right)^{-2/3} \left(\frac{4}{3} \frac{m_i^2\, m_s}{m_e}\right)^{-1/3}. \tag{3.55}$$

In Section 3.8, we compare the echo destruction time due to collisions (t_c) with that due to viscosity (t_v), and find that collisions destroy the echo 5 to 10× faster than viscosity.

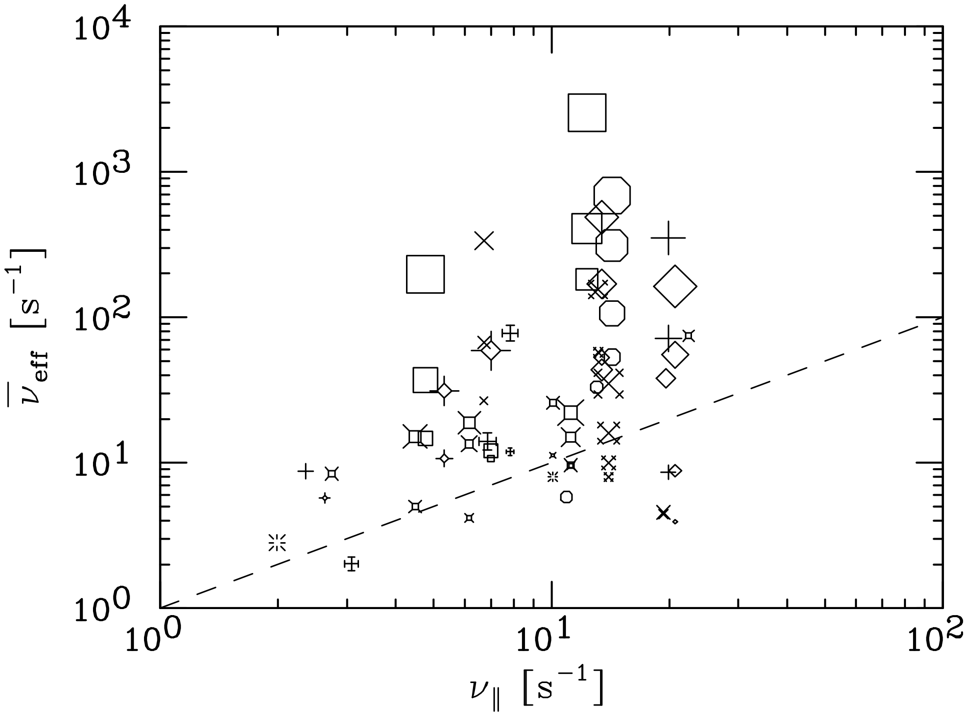

Figure 3.12: The effective electron-electron collision rate $\bar{\nu}_{\text{eff}}$ obtained from the simple collisional theory of Equation 3.54. The plot shows that the more complete treatment of Equation 3.46 is required for quantitative analysis.

3.6 Echo with Applied Noise

We intentionally apply noise (with a 10 MHz bandwidth) to the plasma to artificially increase the velocity scattering rate. We find noise kills the echo, and the echo is destroyed sooner at larger rms noise amplitudes.

Figure 3.13 shows the measured peak echo amplitude S_e, versus the second wave launch time τ, for different strengths of the applied noise. The effective collision frequency for the data set with no noise is $\nu_{\text{eff}} = 30$ sec^{-1}, using the approach described in Section 3.5, and this agrees within a factor of 2 with $\nu_{\parallel} \simeq 15$ sec^{-1}. The data set with 61 mV rms noise yields $\nu_{\text{eff}} = 710$ sec^{-1}, a factor of nearly 24 larger than the no-noise case.

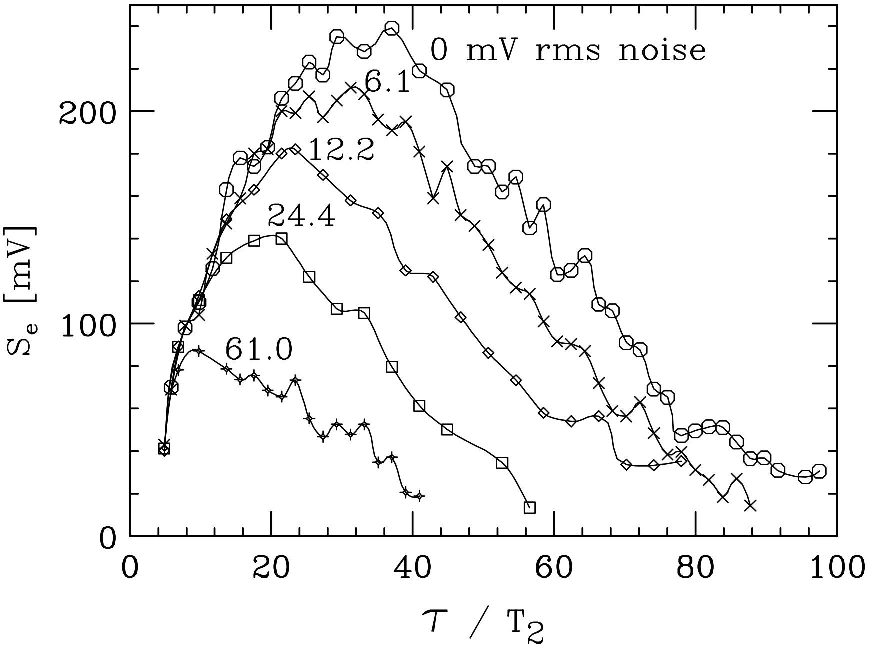

Figure 3.13: Measured peak echo wall signal S_e versus the second wave launch time τ, with and without the enhanced velocity scattering due to applied noise. The effective electron-electron collision rate ν_{eff} increases from 30 sec^{-1} (no noise) to 710 sec^{-1} (61 mV rms noise).

3.7 Filamentation and Cyclotron Discreteness

The echo depends on the maintenance of the coherence of the spiral phase mixing pattern. As time progresses, the density filaments wind up into an ever tighter spiral, and the radial distance between filaments $d(r,t)$ decreases.

A prediction for the filament spacing d is easily obtained from the expression for the first-order density perturbation (see Equation 3.14), which varies as $\exp[im_i(\theta - \omega_R(r)t)]$. We expand the rotation frequency ω_R around the average radial position r_f between two filaments, and set the phase difference between r_f and $r_f + d$ equal to 2π. That is, we use the expansion $\omega_R(r_f + d) \approx \omega_R(r_f) + \frac{\partial \omega_R}{\partial r} d$, and find that the initial density filament spacing varies with time as

$$d(r,t) = \frac{2\pi r}{m_i S(r) t}, \tag{3.56}$$

where the shear $S(r) \equiv r\partial\omega_R/\partial r$ is due to the bulk plasma rotation.

The measured filament spacing $d(r_f, t)$ is plotted in Figure 3.14, showing good agreement with the simple prediction. The solid line is the prediction of Equation 3.56, using the shear measured at the radial location r_f. For the data plotted here, $r_f = 0.7R_w$.

The echo is seen up to 200 $m = 2$ periods after the initial wave excitation, despite the extremely fine-scale initial wave filamentation. At $t = 200\,T_2$ and in this shear S, the filament separation $d = 0.007$ cm $= 1.5\,r_L\,(B/1\,\mathrm{kG})$, where $r_L = \bar{v}/\Omega_c$ is the electron cyclotron radius. When $d \approx r_L$, the filaments are "coarse-grained" by the discreteness effect of the electron cyclotron orbit, and one might expect the echo to be destroyed. However, we presume that the cyclotron motion does not affect the guiding-center dynamics of particles, since the fast cyclotron motion is averaged over a guiding center.

We define the "filament-cyclotron" time t_f as the time when the radial spacing d between filaments is equal to the cyclotron radius r_L. The filament-cyclotron time is found by setting $d(r_c, t_f) = r_L$, yielding

$$t_f \equiv \frac{\Omega_c}{m_i \bar{v}} \left(\left. \frac{\partial f_R}{\partial r} \right|_{r_c} \right)^{-1} . \tag{3.57}$$

Equation 3.57 predicts the scaling $t_f \propto B^2$. At lower fields, the cyclotron radius r_L is larger, so the filament-cyclotron time t_f is sooner.

Presumably, at $t \approx t_f$, the visibility of the density filaments is limited by the discreteness of the cyclotron orbit, since the phase of the cyclotron motion is random at the dump time. This effect might be seen at low fields, but has not yet been explored experimentally.

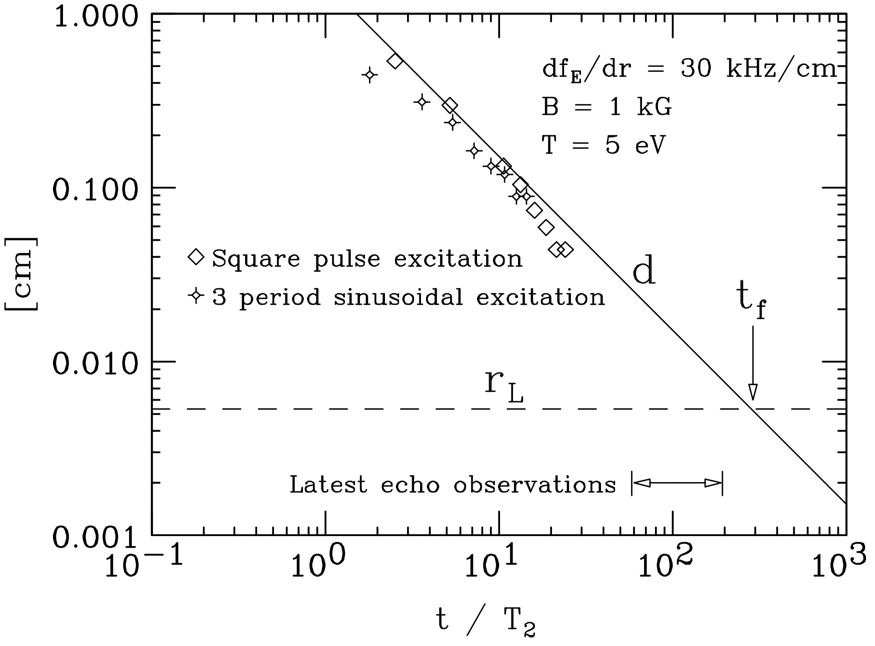

Figure 3.14: The measured radial filament spacing as a function of time. The time $t = 0$ corresponds to the end of the wall excitation. The solid line is the prediction of Equation 3.56, and the dashed line shows the cyclotron radius r_L for $B = 1$ kG and $T = 5$ eV.

3.8 Estimate of Viscous Echo Destruction

Viscosity acts on shear in the $\mathbf{E} \times \mathbf{B}$ flow, resulting in internal transport of particles [15] and a diffusive spreading. Fine-scale structures with large density gradients, such as the spiral filaments, should be "smoothed out" by viscosity. This viscous spreading would result in an increase of a filament's radial width $w(t)$, scaling as $\sqrt{t}$. Simultaneously, the filament radial spacing $d(r, t)$ decreases steadily due to spiral wind-up, with $d \propto t^{-1}$. If a filament's radial width w is comparable to the distance d between filaments, the filaments would overlap and the phase-mixing pattern would be smoothed out, resulting in a loss of phase information and reduction of the echo amplitude.

We estimate the viscous echo destruction time t_v, defined by $d(t_v) = w(t_v)$.

In Appendix A, the (long-range) viscous spreading of a filament is analyzed, giving an estimate for the filament width

$$w(t) = \frac{\omega_p}{\Omega_c}\,(\kappa\, t)^{1/2}\,, \tag{3.58}$$

where κ is the kinematic viscosity, and ω_p is the electron plasma frequency.

Setting $w(t_v) = d(r_c, t_v)$, where d is given by Equation 3.56, we find the viscous echo destruction time is

$$t_v = \left(\frac{\Omega_c}{\omega_p}\right)^{2/3} \left(m_i \frac{\partial f_R}{\partial r}\right)^{-2/3} \kappa^{-1/3}. \tag{3.59}$$

To compare with our experiments, we use values of the kinematic viscosity previously measured in a pure electron plasma [15], given by $\kappa = (40\ \text{cm}^2/\text{sec})$ $(B/1\,\text{kG})$. In addition, we use typical echo-experiment values for the critical radius $r_c = 2.8$ cm, and normalized shear $(\partial f_R/\partial r)|_{r_c} = (25\,\text{kHz/cm})\,(B/1\,\text{kG})^{-1}$.

Our estimate of the viscous echo destruction time is then $t_v = (4.6\,\text{ms})$ $(B/1\,\text{kG}) = 410\,T_2$, using the typical value for the $m = 2$ wave period $T_2 =$ $(11\,\mu\text{s})\,(B/1\,\text{kG})$. This estimate for t_v is $2 \rightarrow 10$ times longer than the echo decay time observed in experiments. Thus, we believe viscosity is not the dominant cause of echo destruction in our experiments.

Figure 3.15 shows the magnetic field scaling for the predicted echo destruction time due to (1) collisions, indicated as t_c (given by Equation 3.55 for a fixed value of end curvature $\Delta L/L_p$); and due to (2) viscosity, indicated as t_v (given by Equation 3.59). The solid lines are drawn for large density $n = 2 \times 10^7$ cm^{-3} and temperature $T = 8$ eV, and the dashed lines are drawn for small density $n = 0.2 \times 10^7$ cm^{-3} and temperature $T = 4$ eV. The data taken at 0.2 kG have low density and are to be compared with the dashed lines.

Best estimates of viscous echo destruction based on the above theory concepts and previous experimental data suggest that viscosity is negligible on the time

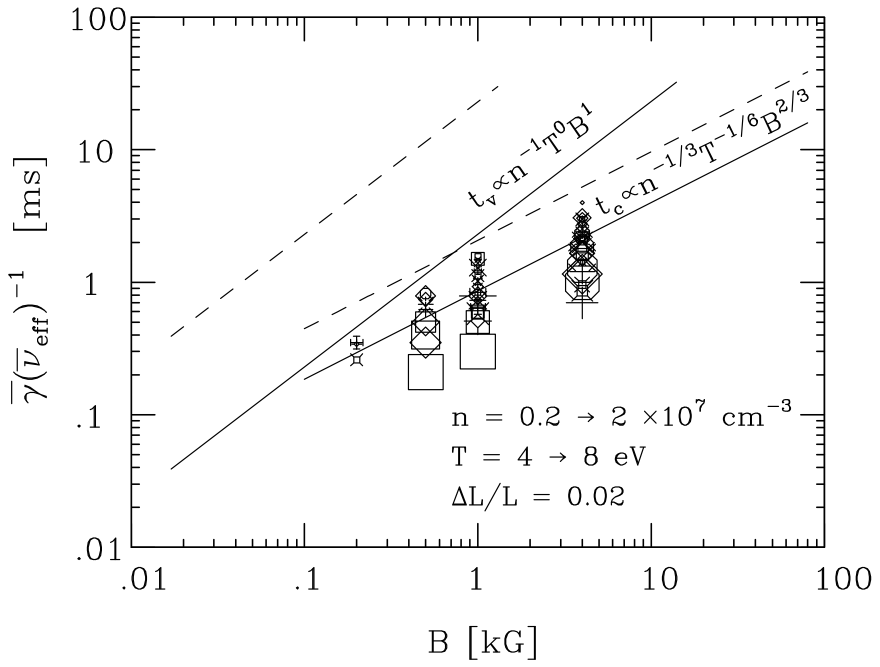

Figure 3.15: Measured echo degradation time $\bar{\gamma}^{-1}$ versus B. The predicted echo degradation times due to collisions (t_c) and viscosity (t_v) are shown, with the solid lines drawn for large n and T, and the dashed lines drawn for small n and T. The data at $B = 0.2$ kG are to be compared with the dashed lines.

scales seen here; and experimentally, we see no compelling reason for it, namely the late-time echo destruction is limited by electron-electron velocity scattering combined with end-field θ-smearing. However, Figure 3.15 shows that at $B \lesssim 0.1$ kG and with large electron density and temperature (solid lines), viscosity may degrade the echo sooner than collisions. In addition, Figure 3.15 shows the effect of large second excitations (indicated by the size of the data symbols) degrading the echo up to 5× faster than collisions.

3.9 Electron-Neutral Scattering

We find that v_z-scatterings from electron-neutral collisions cause negligible echo degradation at pressures below 10^{-8} torr. Figure 3.16 shows S_e versus τ for

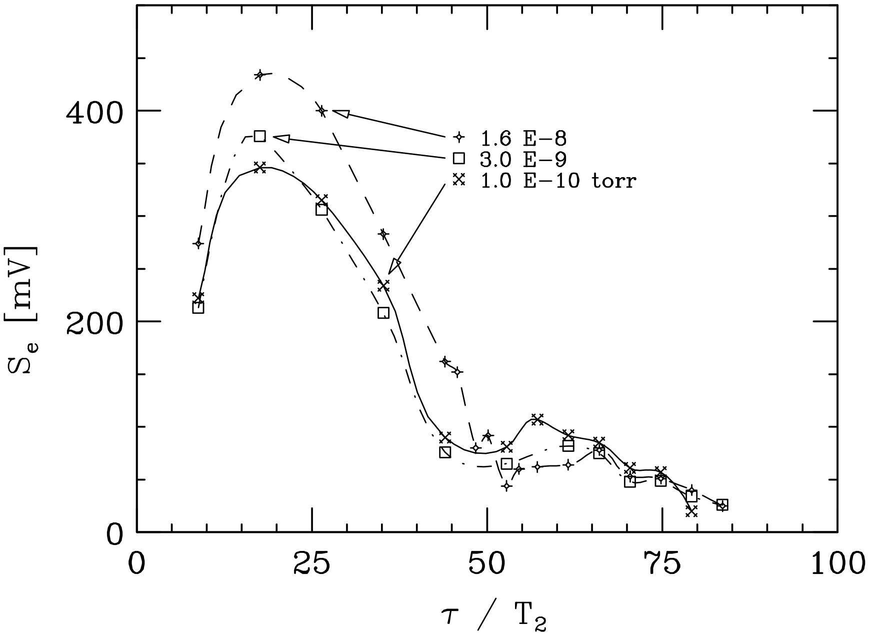

Figure 3.16: The measured echo wall signal S_e versus the second wave launch time τ, for 3 different values of background neutral pressure. At these pressures, the echo destruction at late times is *not* due to electron-neutral collisions.

3 different values of neutral background pressure. The pressure was varied from the nominal $P < 1.0 \times 10^{-10}$ torr up to 1.6×10^{-8} torr, and no significant echo destruction is seen at the higher pressures. Actually, the measured echo amplitude is slightly larger at higher pressure, presumably because changing the background pressure alters the shaped density profile $n(r)$.

3.10 Large Second Wave Effect

At large values of the second wave excitation, e.g. $V_s \gtrsim 1.6$ V in Figure 3.8, there is gross disagreement between the theory and experiment. This "large second wave effect" is not yet understood, and below we discuss possible causes, and describe experiments that show wall-induced particle trapping is not the cause of echo destruction.

One possible cause for the echo destruction at large second wave amplitudes is the resonant collective plasma behavior of the second wave. Collective effects cause particles to deviate from ballistic, free-streaming orbits, and may reduce the echo amplitude.

In addition, we look for particle trapping due to the second wave's potential, in the form of Kelvin's cat's eyes and nonlinear "bouncing" in the second wave amplitude. Using both the wall signal and the CCD camera, we do not observe nonlinear wave particle-trapping at the second wave amplitudes used in the echo experiments. However, the second wave may create a finite but undetectable level of particle trapping, and this effect may destroy the echo at large second wave amplitudes.

Yet another possible explanation is that at large second wave excitations, harmonics of the second wave interact with the initial wave, producing separate echoes. These higher-order echoes are explicitly seen in controlled experiments (see Section 3.12). The echoes may then interfere, causing a reduction of the amplitude of the lowest-order echo.

In addition, the radial electric field from the second wall excitation causes (presumably irreversible) θ-shifts of particles. The maximum θ-displacement from the second wall excitation is found by integrating Equation 3.10, and is given by

$$\delta\theta_s|_{max} \equiv \frac{c}{Br}\frac{\partial A_s}{\partial r} = \frac{c}{Br} k_s V_s \Delta t_s m_s R_w^{-m_s} r^{m_s - 1}. \tag{3.60}$$

An estimate of the second excitation voltage V_s required to cause a θ-shift of $\delta\theta_s|_{max} = \frac{1}{2}(2\pi/m_s)$ (i.e., a shift large enough to presumably prevent echo formation) is $V_s \sim 75$ V, which is 4 times larger than the maximal V_s used in experiments.

The echo degradation at large second excitations is most likely caused by velocity mixing that occurs due to the wall excitation. As mentioned, the wall excitation creates electric fields in the θ-direction, resulting in radial $\mathbf{E} \times \mathbf{B}$ drifts. A particle that steps radially may move to a location with a new electrostatic plasma potential $\phi_o(r)$, resulting in a change in the particle's z-kinetic energy. This velocity mixing mimics collisional velocity scattering. We showed in Section 3.5 that the echo can be destroyed due to collisional velocity scattering, which acts on v_z-dependent θ-smearing in the end confinement fields. We expect that the second-excitation-induced velocity mixing, combined with end-field θ-smearing, can also cause irreversible phase decoherence, but this effect has not been studied experimentally.

Below, we describe experiments that show wall-voltage-induced particle trapping is not the cause for the echo destruction at large second wave amplitudes. The idea here is that the application of large second wave wall voltages creates a temporary separatrix between locally trapped and untrapped particles [30, 12]. This separatrix alters the distribution function, and causes locally enhanced velocity scattering in the boundary layer near the separatrix [13]. One might expect that the enhanced velocity scattering destroys phase information, and kills the echo.

To test this idea, we vary the confinement geometry to reduce or eliminate the wall particle-trapping effect. As shown in Figure 3.17(a), we first place the second-wave-excitation sectored cylinder S7 adjacent to the end confinement cylinder, to reduce the wall particle-trapping effect presumably by a factor of 2 (compared with the nominal configuration with S7 near the z-center of the trap). In this new configuration, we still find a significant deviation between theory and experiments at large V_s, similar to Figure 3.8.

We also use S7 as the whole confinement region, as shown schematically in Figure 3.17(b). After the profile-shaping electric asymmetry is applied to a long plasma as shown in Figure 3.17(a), we "cut" the plasma by lowering the cylinder

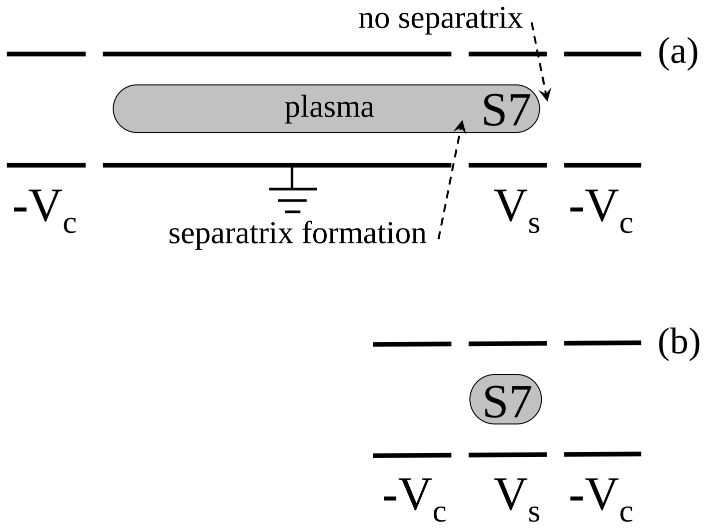

Figure 3.17: In order to minimize wall-induced particle-trapping and separatrix formation, the second wave excitation cylinder S7 is used as (a) the end cylinder, and (b) the whole confinement region (by cutting the plasma).

adjacent to S7 to $-V_c = 100$ V. After the cut, the initial and second waves are excited with (separate) S7 sectors.

This geometry eliminates separatrix formation, yet we continue to see the echo destruction at large second wave amplitudes. We find, then, that wall particle-trapping effects are *not* the cause of the disagreement between theory and data at large values of V_s.

3.11 Squeeze-Pulse Effect

We find that an axisymmetric, $m = 0$ excitation destroys the echo in a similar fashion as the $m_s = 4$ second wave excitation. The temporal form of the $m = 0$ excitation is similar to the half-period square pulse used for the $m_s = 4$ excitation, and we call this applied $m = 0$ excitation a “squeeze-pulse.”

Interestingly, the echo destruction depends on the time t_p at which the squeeze-pulse is applied, and the maximum destruction occurs when $t_p = \tau$. Fig-

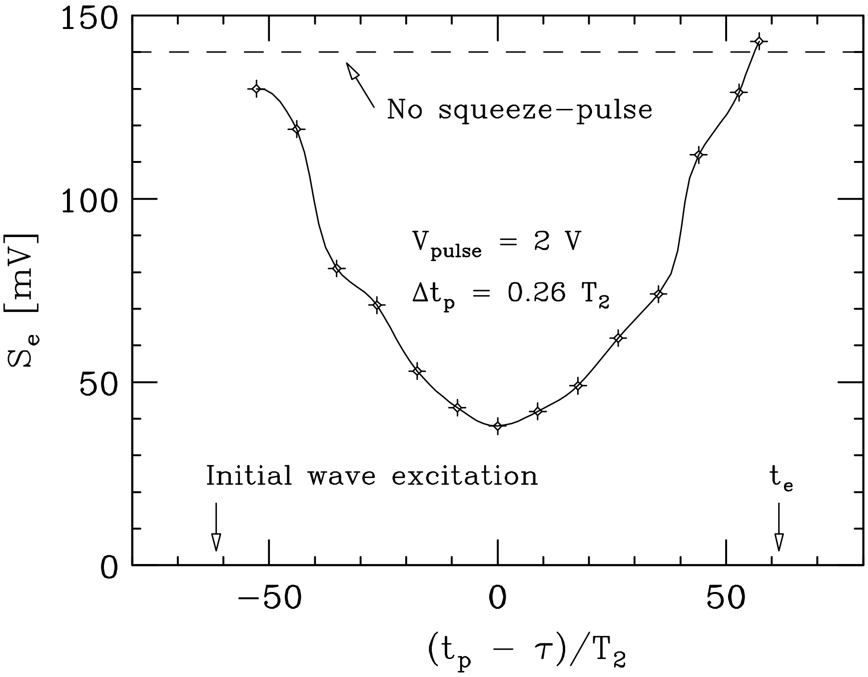

Figure 3.18: The echo amplitude versus the squeeze-pulse excitation time t_p minus the second wave launch time τ. The maximum echo destruction occurs when $t_p = \tau$.

ure 3.18 demonstrates this effect, showing the measured echo wall signal S_e versus the squeeze-pulse application time t_p minus the second wave launch time τ, normalized to the $m = 2$ wave period T_2. The dashed line shows S_e with no squeeze-pulse applied. For this data, the squeeze-pulse cylinder is near the z-center of the trap, and the squeeze-pulse duration is $\Delta t_p = 0.26\,T_2 \approx 0.5\,T_4$.

In the previous sections, we found that large second wave excitations destroy the echo. Typically, the $m_s = 4$ excitation is applied with one polarity only (only 4 of the 8 sectors on S7 are normally used, because the others are used for detection and electric tilt), resulting in a significant $m = 0$ component. A single-polarity $m = 4$ excitation applied to $4 \times 25°$ sectors has an $m = 0$ Fourier component of 0.28, and an $m = 4$ Fourier component of 0.49.

We test if the squeeze-pulse effect from the finite $m = 0$ component of the typical $m_s = 4$ excitation is the dominant cause of echo destruction at large V_s. Utilizing relays, we use all 8 sectors of S7 to excite the $m_s = 4$ perturbation with $+/-$ polarity, thus eliminating the $m = 0$ component ($m = 0$ component of 0, $m = 0 = 4$ component of 0.98). In this configuration, the echo is destroyed just as effectively by large V_s. This result demonstrates that the echo destruction at large second wave amplitudes is not due to the squeeze-pulse effect.

3.12 Echoes of Spatial Harmonics

The sectored cylinders used to excited the diocotron waves produce "square wave" potentials in θ at $r = R_w$, so spatial Fourier harmonics of the applied signal can produce their own echoes. In addition to the $m = 2$ echo discussed thus far, we observe echoes of the spatial harmonics of the applied wall excitations at $m = 4, 6, ...$

Here we apply two temporally-separated excitations of the *same* fundamental mode number $m = 2$, and find that the third spatial harmonic of the second excitation ($m_s^{(3)} = 6$) can interact with the first harmonic of the initial excitation ($m_i^{(1)} = 2$), producing an echo. Here, the superscripts in parenthesis refer to the spatial harmonics being considered. We find that applying two $m^{(1)} = 2$ excitations, separated by time τ, produces an $m_e^{(1,3)} = m_s^{(3)} - m_i^{(1)} = 4$ echo at time $t_e \approx 3\tau/2$.

The measured wall signals are shown in Figure 3.19 for two detector configurations, one chosen to maximize the $m = 2$ signal, and the other chosen to maximize the $m = 4$ signal. The observed time of the beginning of the $m = 4$ echo agrees with the predicted time $t_e^{(1,3)} = \tau\, m_s^{(3)}/m_e^{(1,3)} = \frac{3}{2}\tau = 0.18$ ms. The first two pulses of the bottom trace are a direct coupling of the $m = 2$ excitations to the $m = 4$ detection, and do not represent the $m = 2$ or $m = 4$ response of the plasma.

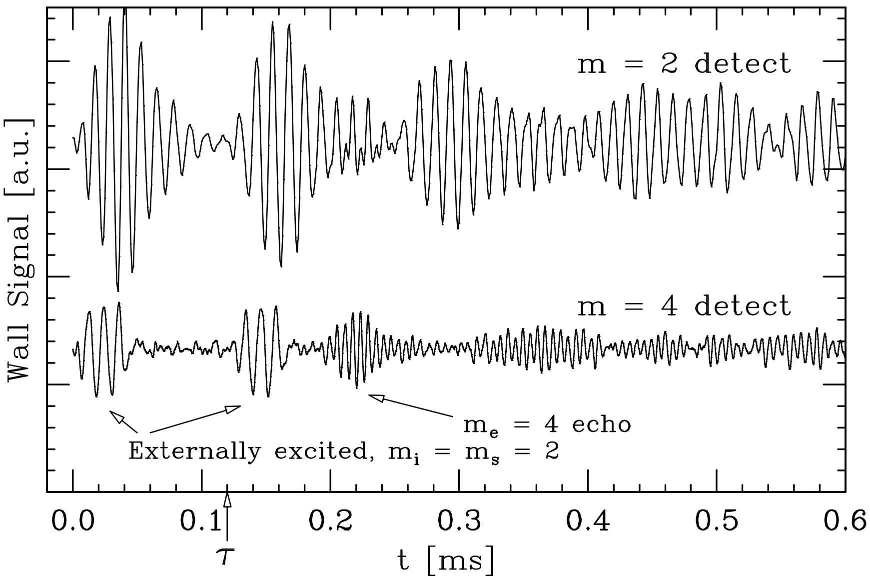

Figure 3.19: The measured wall signals from $m_i = 2$ and $m_s = 2$ excitations, using detection schemes that maximize the $m = 2$ signal (top), and the $m = 4$ signal (bottom). The $m_e^{(1,3)} = 4$ echo is due to the third spatial harmonic of the second excitation modulating the initial excitation. Higher-order echoes are also seen.

The third "wavepacket" of the top trace in Figure 3.19, beginning at $t = 0.25$ ms $\approx 2\tau$, is an $m = 2$ echo. This echo is due to the interaction of the $m_s^{(1)} = 2$ first harmonic of the second wave with the $m_e^{(1,3)} = 4$ echo. The $m = 2$ echo at $t = 0.25$ ms could also be due to the interaction of the first harmonic of the initial wave $m_i^{(1)}$ with the second harmonic of the second wave $m_s^{(2)}$.

The $m = 4$ echo later in time, beginning at $t \approx 2.6\,\tau = 0.32$ ms, is presumably due to even higher spatial harmonics. This echo's azimuthal mode number and time of echo appearance are consistent with the interaction of the second excitation ($m_s^{(1)} = 2$ at $t = \tau$) with an (undetected) $m = 6$ echo at $t = 2\,\tau$. This $m = 6$ echo itself is presumably due to the third spatial harmonic of the first wave ($m_i^{(3)} = 6$) interacting with the sixth spatial harmonic of the second wave ($m_s^{(6)} = 12$).

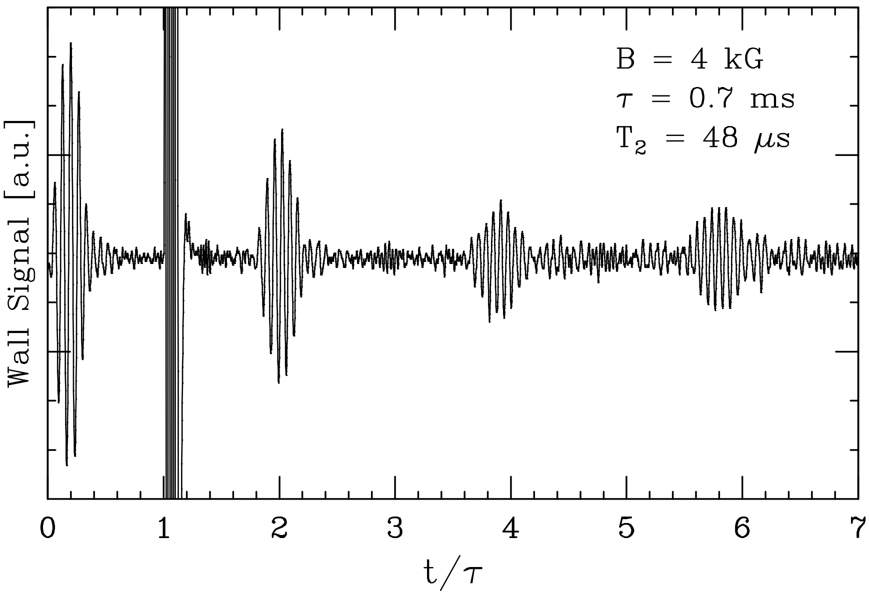

Figure 3.20: Echoes of echoes seen from the measured wall signal with $m_i = 2$ and $m_s = 4$ excitations, using an $m = 2$ detection. For the excitation parameters used here, a train of $m = 2$ echoes of echoes is seen at $t \sim 2$, 4, and $6\,\tau$.

3.13 Echoes of Echoes

Echoes of echoes are also observed, resulting in a train of echoes that can persist 3 to 6× longer than the late-time observation of a single lowest-order echo.

Figure 3.20 shows the measured wall signal versus time, using the nominal $m_i^{(1)} = 2$ and $m_s^{(1)} = 4$ excitations. Here, an $m = 2$ detection scheme is used, and 3 distinct $m = 2$ echoes are seen. Other data show a train of as many as 25 distinct $m = 2$ echoes, the latest echo being visible at $t \simeq 550\ T_2 = 25$ ms (at 4 kG) after the initial wave excitation. This is 4× longer than expected from the progressive collisional velocity scatterings acting on a single echo, described by t_c. We find that in general, echoes of echoes persist longer when τ is smaller.

The first two pulses in Figure 3.20 show the initial and second external excitations. The second pulse is a direct coupling of the $m_s = 4$ excitation to the wall sectors used as detectors. The first $m = 2$ echo, peaking at $t \approx 2\,\tau$, is the lowest-order echo. The second $m = 2$ echo, peaking at $t \approx 4\,\tau$, is due to the first echo interacting with a $m = 4$ echo at $t \approx 3\,\tau$, and is an echo of an echo. The $m = 4$ echoes are not easily seen in Figure 3.20 because of the $m = 2$ detection scheme, but are readily observed using a detection that maximizes the $m = 4$ signal. These $m = 4$ echoes occur midway (in time) between each pair of $m = 2$ echoes, and presumably are due to spatial harmonics of the external wall excitations. The late-time observations of $m = 2$ and $m = 4$ echoes, however, suggests that nonlinear harmonic generation occurs within the plasma as well.

Chapter 4

Trapped-Particle Diocotron Modes, Collisional Damping, and Transport

4.1 Overview

We now turn our attention to the Trapped-Particle Diocotron Mode, its collisional damping, and the associated transport in the presence of θ-asymmetries.

Local particle trapping is endemic in Penning-Malmberg traps due to small construction errors ($\sim$0.1 mm) in the confinement electrode stack, and due to weak axial variations ($\sim 10^{-3}$) in the magnetic field. A local electrostatic barrier or magnetic mirror prevents some particles from traversing the entire trap along the z-direction, and this creates a velocity-space separatrix between trapped and passing particles.

The TPDM consists of $\mathbf{E} \times \mathbf{B}$ drifting trapped particles that are 180° out of phase on either end of an electrostatic squeeze barrier, with passing particles partially Debye shielding these drift perturbations. The TPDM's have $k_z \neq 0$ and azimuthal mode number $m = 1, 2, ...$; in this thesis we focus on $m = 1$. A linear kinetic theory predicts mode frequencies that agree within 10% of the measured mode frequencies.

The mode damps due to particle scatterings across the velocity-space separatrix. When we resonantly excite particles with velocities near the separatrix velocity, we observe up to a 10× increase in the mode damping rate, due to enhanced separatrix crossings. In addition, by varying the frequency of the applied RF signal, we are able to map out the Maxwellian velocity distribution near the separatrix.

Small, unavoidable electric or magnetic θ-asymmetries in the confinement fields are known to cause bulk radial transport, and eventual plasma loss. We find that this aymmetry-induced transport is driven by collisional separatrix crossings, for a wide range of plasma parameters. Currently, we observe the TPDM with electric trapping only, and do not observe the mode with magnetic trapping. However, asymmetry-induced transport is caused by particles diffusing across either an electric *or* magnetic separatrix in velocity space. The measured transport rate is proportional to the mode damping rate, with simple scalings for all other plasma parameters.

4.2 Electric Trapping and the Trapped-Particle Dioctron Mode

To study the TPDM, a negative squeeze voltage $-V_{sq}$ is applied near the z-center of the trap, creating a velocity-space separatrix and locally trapping a fraction of the particles. Figure 4.1 shows a schematic of a squeezed plasma, with the TPDM causing density and potential variations. By itself, V_{sq} causes the equilibrium to "neck down" in the center. The $k_z \neq 0$, $m = 1$ TPDM creates further variations on this equilibrium. The light and dark shading in the plasma represent positive and negative mode potentials. The TPDM has z-odd parity; that is, the mode potential is essentially uniform with z within each end, but has

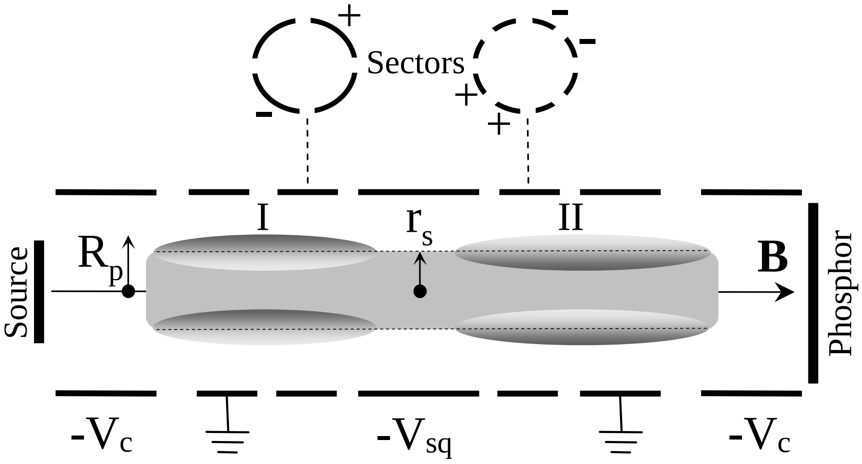

Figure 4.1: The TPDM in a pure electron plasma, with sectors showing the excitation method.

a 180° phase shift on either side of the squeeze barrier.

Particles at radius r with axial velocity v_z less than the separatrix velocity $v_s(r)$ are trapped, while particles with $v_z > v_s(r)$ sample both sides of the squeeze barrier and are called "passing." Simple energy considerations give the separatrix velocity as $v_s(r) = \sqrt{2eV_{sq}(r)/\mathrm{m}}$, where $V_{sq}(r)$ is the amount that the potential at $z = 0$ is changed by the applied wall voltage $V_{sq}(R_w)$.

In Figure 4.2, we schematically show particle trajectories in phase space (z, v_z), along a given magnetic field line at $r = 0.5$ cm. An electric squeeze voltage of $V_{sq} = 2\phi_p/3$ is applied to the central confinement cylinder, typically with length $L_{sq} = 7$ cm, resulting in a separatrix velocity $v_s \approx 0.7\,\bar{v}$. Here, the plasma potential is defined as $\phi_p \equiv \phi_o(r = 0, z = 0)$. All particles are reflected by the confinement fields at the ends of the trap. Solid lines represent orbits of passing particles, and dashed lines represent orbits of particles trapped in one end or the other. The shaded region represents the boundary layer near the separatrix, where the effects of collisions are important in smoothing out the perturbed distribution function.

The squeeze potential increases with radius, so more trapped particles are

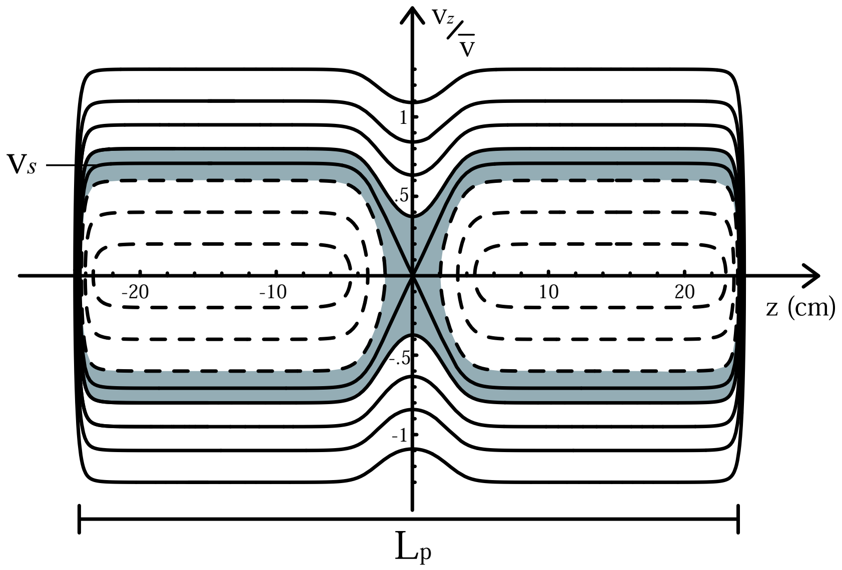

Figure 4.2: Phase space orbits in the presence of an electric squeeze. The solid lines represent trajectories of passing particles, and the dashed lines represent trajectories of trapped particles.

located near the radial edge of the plasma at $r \gtrsim r_s$, where r_s is defined by $v_s(r_s) = \bar{v}$. Figure 4.1 shows r_s schematically; however, with any significant squeeze voltage, particles are trapped at all radii. For small V_{sq}, a fraction

$$\frac{N_L^{(tr)}}{N_L} \approx 1.2 \frac{V_{sq}}{\phi_p} \tag{4.1}$$

of the electrons are trapped, where the line density $N_L \equiv \int 2\pi r \, dr \, n(r)$.

The mode is excited by applying $m = 1$ voltages that are 180° out-of-phase on either end of the plasma. We typically resonantly excite the mode using a 1 to 10 period sinusoidal drive near the mode frequency. Using other wall sectors as receiving antennae, the mode signal is detected and digitized. This waveform is then fit with an exponentially decaying sine wave, giving the measured frequency and damping rate.

Figure 4.3 shows the measured TPDM frequency f_a and damping rate γ_a

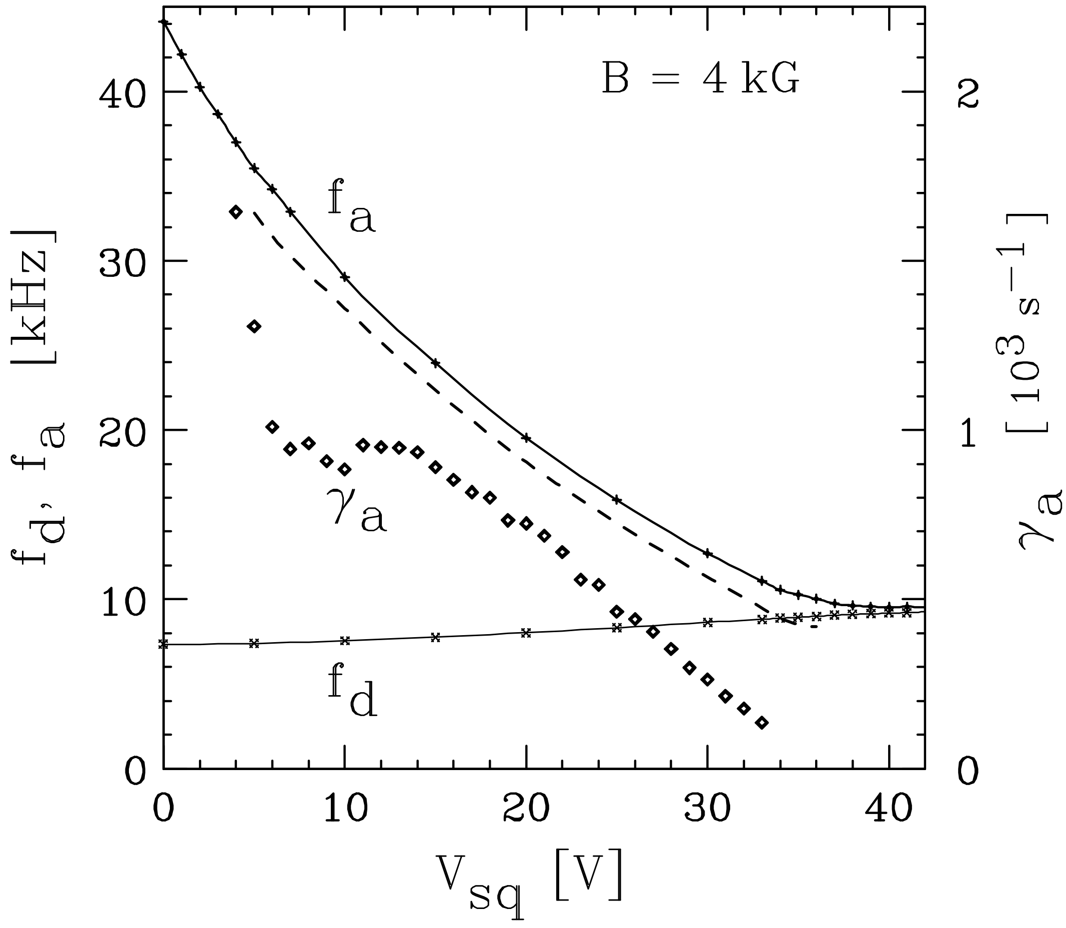

Figure 4.3: Measured frequency and damping rate of the TPDM versus squeeze voltage V_{sq}. The dashed line shows the theory prediction for the mode frequency, and the measured $m = 1$ diocotron mode frequency f_d is shown for reference.

as the applied squeeze voltage V_{sq} is varied. The measured mode frequency f_a is compared to a simple kinetic theory model [10] with an idealized zero-length trapping barrier, and is found to agree within 10%. The standard $m = 1, k_z = 0$ diocotron mode frequency f_d is also shown for reference. At small V_{sq}, f_a is largest, and is near the edge plasma rotation frequency $f_R(R_p)$. As V_{sq} increases, f_a decreases until the plasma is essentially cut in half at $V_{sq} \gtrsim \phi_p$. For these large squeezes, the TPDM is equivalent to two 180° out-of-phase $k_z = 0$ diocotron modes in either end of the plasma.

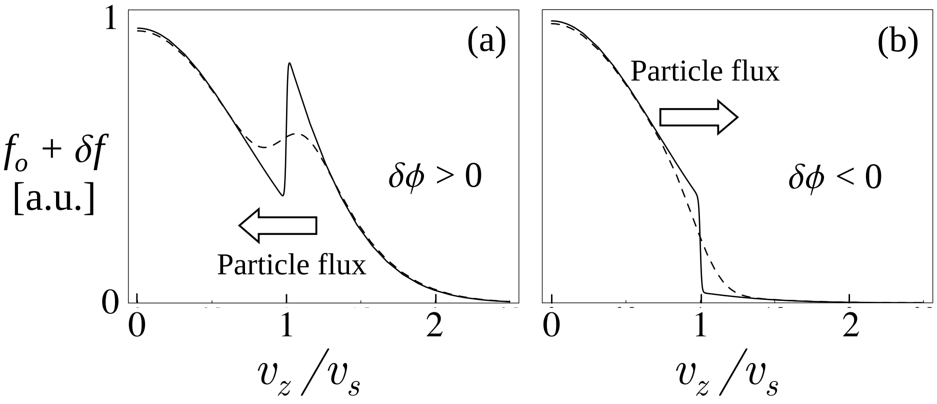

Figure 4.4: Schematic of diffusion across the velocity-space separatrix. The solid lines represent (fabricated) initial states, and the dashed lines show $f(v)$ after partial collisional relaxation at $t = \nu_{\|}^{-1}/100$. For (a) $\delta\phi > 0$, the net particle flux is to lower velocities (from passing to trapped populations). For (b) $\delta\phi < 0$, net particle flux causes an increase of the fraction of passing particles.

4.3 Mode Damping due to Collisional Separatrix Crossings

We find that the TPDM damps due to collisional separatrix crossings. Any velocity-space diffusion near the separatrix mixes the trapped and passing populations, which damps the TPDM.

The dynamics of trapped and passing particles are different, resulting in a perturbed distribution function near the separatrix velocity. Without collisions, the distribution function would (theoretically) be discontinuous at v_s. Small-angle velocity scattering, however, would then tend to smooth the distribution function in the boundary layer near the separatrix, resulting in a flux of particles in velocity space.

Figure 4.4 shows a schematic of this diffusion across the separatrix. The solid lines are hypothetical initial conditions for the distribution function, and the dashed lines show the partial relaxation after a time of $0.01\,\nu_{\|}^{-1}$, where $\nu_{\|}$ is the electron-electron parallel diffusion rate given by Equation 3.36. The dashed lines are obtained by numerically solving the Boltzmann equation using a Fokker-Planck collision operator, with the solid lines as the initial conditions. These sharp initial gradients give rise to large fluxes. Figure 4.4(a) and (b) represent opposite phases of a mode cycle. In (a), we have $\delta\phi > 0$ as at point II in Figure 4.1, and there is an excess of passing particles; collisional diffusion across the separatrix causes a net flux of particles from passing ($v_z > v_s$) to trapped ($v_z < v_s$). In (b), we have $\delta\phi < 0$ as at point I, and the flux is from trapped to passing.

Below we describe a linear, kinetic theory of the damping, and compare with experiments.

4.3.1 Hilsabeck and O'Neil Theory

Recent theory developed by Hilsabeck and O'Neil [13] describes the TPDM damping using a boundary layer analysis, similar to that used by Rosenbluth, Ross, and Kostomarov [31] for the dissipative trapped-ion instability. A Fokker-Planck collision operator models velocity scattering, which smooths out the separatrix discontinuity over a boundary layer width $\delta v_s \approx \bar{v}\sqrt{\nu_\parallel / f_*}$, where $f_* \equiv m f_R(r) - f_a$ is the TPDM frequency seen in the rotating plasma frame.

The modes are taken to be of the form $\delta\phi_a(r,\theta,z,t) = \widetilde{\delta\phi}_a(r,z)e^{i(m\theta-\omega_a t)}$, with a step function in z for the mode potential:

$$\widetilde{\delta\phi}_a(r,z) = \begin{cases} -\widetilde{\delta\phi}_a(r) & z < 0 \\ +\widetilde{\delta\phi}_a(r) & z > 0. \end{cases} \tag{4.2}$$

The trapped and passing particle densities satisfy $n_t(r) + n_p(r) = n(r)$, and are given by

$$n_t(r) = \int_{-v_s(r)}^{v_s(r)} dv_z\, f_M(r, v_z), \tag{4.3}$$

$$n_p(r) = 2\int_{v_s(r)}^{\infty} dv_z\, f_M(r, v_z), \tag{4.4}$$

where $f_M(r, v_z)$ is the equilibrium Maxwellian velocity distribution.

Passing particles sample both ends of the plasma, and are assumed to have a zero bounce-averaged mode potential. That is, the passing particles are assumed to experience no bounce-averaged $\mathbf{E} \times \mathbf{B}$ drift perturbations, and to develop *only* the Debye shielding response. In contrast, trapped particles execute $\mathbf{E} \times \mathbf{B}$ drift orbits in the z-independent potential $\widetilde{\delta\phi}_a(r)$. The trapped and passing particles responses are

$$\begin{aligned} \delta f_a^{(t)}(r, v_z) &= \frac{cm}{2\pi B r} \frac{\widetilde{\delta\phi}_a(r)}{f_*(r)} \frac{\partial f_M}{\partial r} \qquad \mathbf{E} \times \mathbf{B} \text{ drifts,} && (4.5) \\ \delta f_a^{(p)}(r, v_z) &= \frac{e\widetilde{\delta\phi}_a(r)}{T} f_M \qquad \text{Debye shielding,} && (4.6) \end{aligned}$$

leading to a (theoretical) discontinuity at the separatrix. The Fokker-Planck collisional operator contains velocity derivatives that become arbitrarily large at such a discontinuity, so the effects of collisions cannot be ignored even if $\nu_\parallel$ is small.

The linearized Boltzmann equation is solved for the trapped and passing particle distributions, with the requirement that the values and slopes of $\delta f_a^{(t)}$ and $\delta f_a^{(p)}$ match at $v_z = v_s$. Substituting into Poisson's equation yields an eigenvalue equation for the mode potential, subject to the boundary conditions $\widetilde{\delta\phi}_a(0) = \widetilde{\delta\phi}_a(R_w) = 0$. This eigenvalue equation is then solved for the mode damping rate γ_a. The damping rate depends on the boundary layer width δv_s, and is given by

$$\gamma_a = \frac{\dfrac{2\sqrt{\pi}B}{m} \displaystyle\int_0^{R_w} r\,dr |\widetilde{\delta\phi}_a|^2\, \bar{v} \sqrt{\frac{\nu_\parallel}{f_*}} \left[\frac{2\pi e\, f_M}{T} - \frac{c}{Br} \frac{\partial f_M}{\partial r} \frac{m}{f_*} \right]_{v_z = v_s}}{\displaystyle\int_0^{R_w} dr \frac{|\widetilde{\delta\phi}_a|^2}{f_*^2} \frac{\partial n_t}{\partial r}}. \tag{4.7}$$

The Debye shielding response of passing particles is seen in the first term in the brackets, and the $\mathbf{E} \times \mathbf{B}$ drifts of trapped particles is seen in the second term.

The theory assumes a rapid bounce frequency $f_b >> f_R, f_a$, and the predicted mode damping rate agrees only to within about 50% with experiments

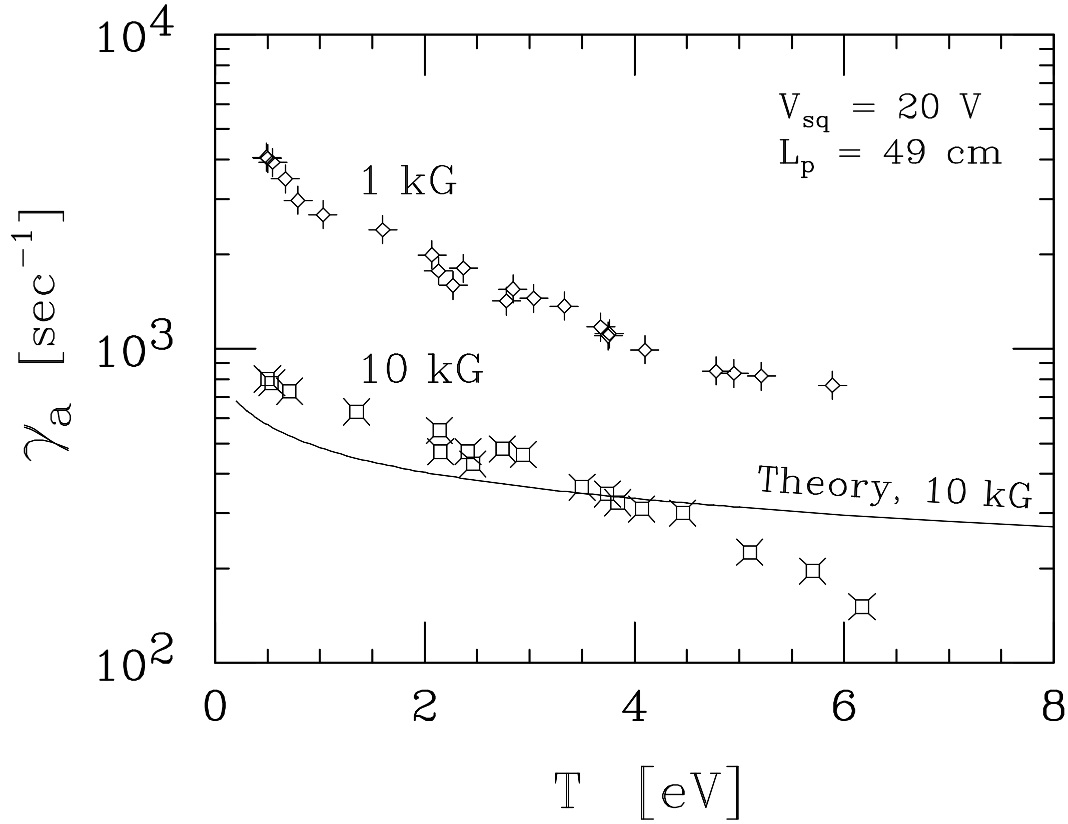

Figure 4.5: Measured TPDM damping rate γ_a versus plasma temperature T.

performed on plasmas that satisfy this frequency ordering. In addition, the experimental eigenfunction of the TPDM has a phase shift of 0.2 π for $r \lesssim r_s$. This phase shift is not understood theoretically, and may be related to subtleties of dynamical Debye shielding. Furthermore, in Section 4.5, we show that passing particles actually $\mathbf{E} \times \mathbf{B}$ drift in an applied asymmetry field, which mimics the TPDM potential.

4.3.2 Mode Damping Measurements

The mode damping depends on temperature, with strong damping at low temperature, and weaker damping at higher temperatures. Figure 4.5 shows the measured mode damping rate γ_a versus the plasma temperature T, for $B = 1$ and

10 kG, $V_{sq} = 20$ V, and $L_p = 49$ cm. The temperature is varied using the standard wiggle heating method [32, 33], by applying an RF drive to one of the confinement cylinders in resonance with the axial electron bounce frequency $f_b \equiv v_z/2L_p$. We typically use a chirped RF drive ($f_{RF} = 0.5 \rightarrow 2.5$ MHz) so that particles with a range of axial velocities are resonantly heated.

The measured mode damping rate γ_a decreases with temperature, since higher temperature plasmas have a lower collision rate and thus less separatrix diffusion. Theory prediction of γ_a for the 10 kG case is shown as a solid line, and agrees with experiments roughly within a factor of two. The theory predicts a weaker T dependence for γ_a than is observed in experiments.

Figure 4.6 shows the measured and predicted γ_a versus magnetic field strength B. Equation 4.7 predicts that the damping rate scales as $1/\sqrt{B}$, and this scaling is seen in experiments for large fields of $B \simeq 2$ to 10 kG, where the theory assumption of rapid bounce frequency $f_b >> f_R, f_a$ is satisfied. At low fields, however, experiments show a $1/B$ dependence, which is not understood theoretically.

4.3.3 Mapping the Electric Separatrix

The TPDM damping rate is greatly increased by applying an external RF drive that is resonant with the axial bounce motion of marginally trapped particles [34]. The RF drive induces scattering across the separatrix, and the enhanced mode damping rate demonstrates unambiguously that the mode damping is due to separatrix crossings. By varying the RF drive frequency, we can map out the structure of the electric separatrix in velocity space.

We apply the RF wiggle to a confinement cylinder that has an existing DC squeeze voltage V_{sq}. The total applied voltage to the squeeze cylinder is $V_{tot} =$

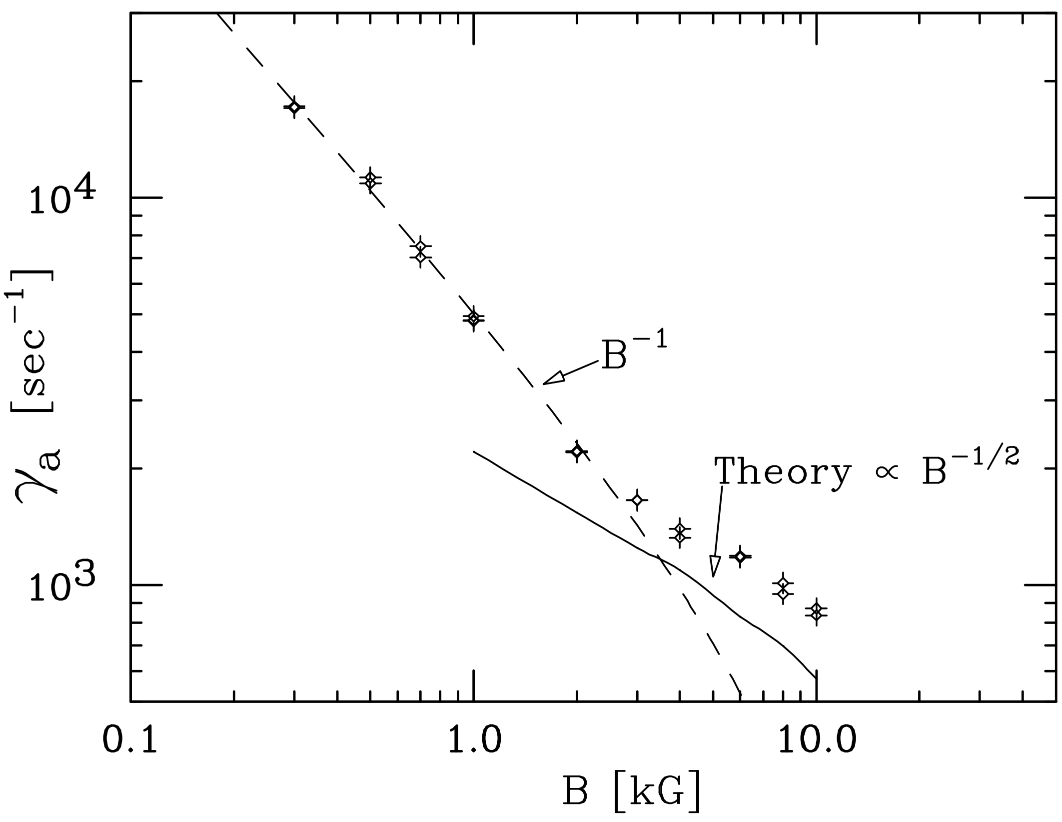

Figure 4.6: Measured TPDM damping rate versus magnetic field. Theory prediction is shown as a solid line, and is valid only for rapid bounce frequency $f_b >> f_R, f_a$. The dashed line shows B^{-1} scaling.

$V_{sq} + V_{RF}\ \sin(2\pi f_{RF}\, t)$.

Figure 4.7 shows the measured mode damping rate γ_a versus the applied RF frequency f_{RF}, for various DC squeeze voltages. Here, the mode damping is increased by a factor of 3 to 4 when the bounce resonance condition $v_s = f_{RF} L_p$ is satisfied. For other plasma parameters with weaker inherent collisional damping, we observe the damping rate increase by a factor of 10 when the resonance condition is satisfied. The lines in Figure 4.7 are Gaussian shapes merely to guide the eye.

The separatrix velocity depends on the DC squeeze voltage as $v_s(r) = \sqrt{2eV_{sq}(r)/\mathrm{m}}$, and the peak resonant RF frequencies $f^\star_{RF}$ shift with different V_{sq} in quantitative agreement with $f^\star_{RF} = v_s/L_p$. For example, the plasma with an 8 V

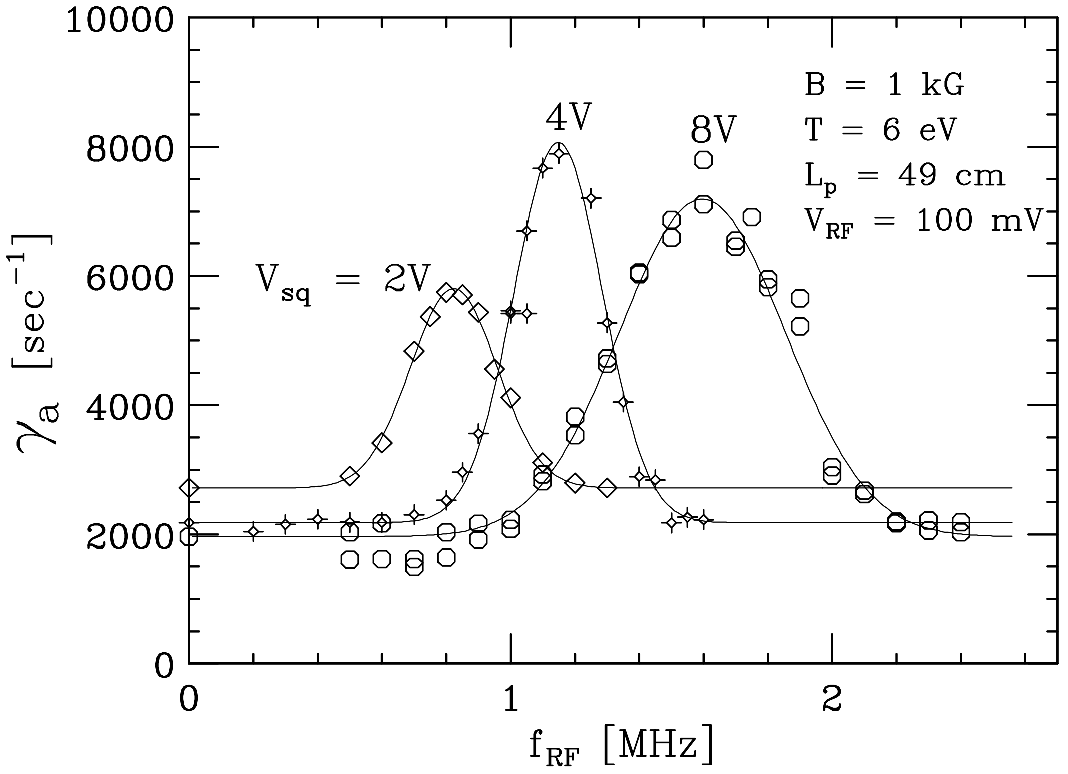

Figure 4.7: TPDM damping rate γ_a versus RF wiggle frequency f_{RF} for various DC squeeze voltages. The RF drive enhances velocity scattering across the separatrix.

squeeze has a peak resonant frequency $f^{\star}_{RF}$ that is 2× that of the plasma with a 2 V squeeze, consistent with $f^{\star}_{RF} \propto \sqrt{V_{sq}}$.

The widths of the resonant peaks predominantly result from the radial averaging of the separatrix velocity. This radial averaging includes the radial dependence of $v_s(r)$, and the radial dependence of the trapped and passing particle densities. Presumably, the separatrix scattering depends on the product $n_t(r)n_p(r)$ of trapped and passing particle fractions, each of which depends on radius. In addition, the separatrix velocity itself depends on radius, because the potential from the squeeze voltage $V_{sq}(r)$ is radially dependent.

For the data in Figure 4.7, naively calculating the peak resonant frequency

$f^{\star}_{RF}$ as $v_s(R_w)/L_p$ wall gives $f^{\star}_{RF}$ that is 2× larger than observed. This implies that the *radially averaged* squeeze potential is 4× less than V_{sq} applied to the wall, since $f^{\star}_{RF} \propto \sqrt{V_{sq}}$.

The resonant frequency $f^{\star}_{RF}$ shifts with different plasma temperatures [34], and higher temperatures result in larger $f^{\star}_{RF}$. These temperature-induced shifts in the resonant peaks occur due to the different velocity distributions of plasma particles, due to the dependence of γ_a on the collisional frequency $\nu_{\|}$, and more subtly, due to differences in Debye shielding of the squeeze voltage. One important result of studying the TPDM is that the mode damping γ_a characterizes *all* the complicated temperature dependence of the separatrix crossings, as will be seen next.

4.4 Asymmetry-Induced Transport with Electric Trapping

Many previous experiments have measured "asymmetry-induced transport" due to inherent (or applied) θ-asymmetries in the trapping fields of nonneutral plasmas; but the detailed mechanism of asymmetry-induced transport remained unknown. Other than the transport due to the "rotational pumping" mechanism [35, 36], previous theory [37, 38] did not agree with transport measurements.

Here we demonstrate that asymmetry-induced transport is often due to the same separatrix crossings that cause TPDM damping, for a wide range of plasma parameters. This trapped-particle-mediated transport is rather ubiquitous in pure electron plasmas, because (1) the rate of separatrix dissipation $\sqrt{\nu_{\|}/f_*}$ is enhanced in low collisionality plasmas, and (2) magnetic trapping can be important for even small magnetic ripples of strength $\delta B/B \sim 10^{-3}$.

In this section, we apply θ-asymmetric electric or magnetic fields (tilts) in addition to the symmetric squeeze voltage, and weakly excite the TPDM to study the connection between transport and separatrix crossings. The asymmetric fields produce transport with or without the TPDM present; the damping of the TPDM merely provides a convenient experimental measure of the separatrix diffusion.

θ-asymmetric electric or magnetic confinement fields create torques on the plasma. These torques change the total canonical angular momentum of the plasma, and change the average plasma radius. The plasma angular momentum is

$$P_\theta \equiv \left[-\frac{eB}{c} \left(R_w^2 - \langle r^2 \rangle \right) + m\langle r v_\theta \rangle \right] N_{tot}, \tag{4.8}$$

where $\langle\ \rangle$ represents an average over all particles. The mechanical part of the angular momentum, mrv_θ, is much smaller (as $r_L/R_p \sim 10^{-2}$ to 10^{-3}) than the vector potential part in a strongly magnetized electron column, so the angular momentum is approximately proportional to $\langle r^2 \rangle$. Thus, static θ-asymmetric fields cause the rotating plasma to lose (negative) angular momentum and expand. We define the transport rate by the measured rate of plasma expansion, as

$$\nu_p \equiv \frac{1}{\langle r^2 \rangle} \frac{d\langle r^2 \rangle}{dt} \approx \frac{1}{P_\theta} \frac{dP_\theta}{dt}. \tag{4.9}$$

4.4.1 Description of Experiments

We apply a static θ-asymmetry with $m = 1, k_z = 1$, using either a magnetic or electric tilt. A magnetic tilt is a misalignment of the magnetic field with respect to the axis of the trap cylinder. The field is $\mathbf{B} = B(\hat{\mathbf{z}} + \alpha_{Bx}\hat{\mathbf{x}} + \alpha_{By}\hat{\mathbf{y}})$, and the magnetic tilt angle is $\alpha_B = \sqrt{\alpha_{Bx}^2 + \alpha_{By}^2}$. The magnetic field is tilted using the B_x and B_y saddle coils, which are typically used for B_z alignment.

Electric "tilt" is an $m = 1$ electrostatic asymmetry applied to sectored cylinders. The tilt is applied either (1) to one end only (single tilt), or (2) to both ends antisymmetrically in z (double tilt), similar to the excitation of the TPDM shown in Figure 4.1.

In the experiments, we take CCD measurements of $n(r, \theta, t)$ at two times separated by Δt. We choose Δt so that the plasma expands by about 2%; this minimizes the temperature increase (due to expansion-liberated electrostatic energy) during the measurements. We then use the same plasma conditions and excite the TPDM, and measure the damping rate.

A separate method of measuring the transport rate is based the rate of change of the (undamped) $m = 2$ diocotron mode frequency f_2, and allows simultaneous measurements of the transport rate ν_p and the TPDM damping rate γ_a. This method gives transport rates that agree to within 3% with measurements of the transport rate using the CCD camera. The method is based on the invariance of the plasma line density $N_L \propto \langle n \rangle \langle r^2 \rangle \propto f_2 \langle r^2 \rangle$, where the last step follows from the diocotron frequency being proportional to the average of the density $\langle n \rangle$ (see Equation 2.12). The transport rate is then given by

$$\nu_p \equiv \frac{1}{\langle r^2 \rangle} \frac{d\langle r^2 \rangle}{dt} = -\frac{1}{f_2} \frac{df_2}{dt}. \tag{4.10}$$

4.4.2 Transport Proportional to Mode Damping

In a squeezed, tilted plasma, we find that the bulk transport rate ν_p is directly proportional to the TPDM damping rate γ_a. This correspondence between ν_p and γ_a shows that a common physical mechanism is responsible for both particle transport and TPDM damping.

Figure 4.8 shows the measured transport rate ν_p versus the measured TPDM damping rate γ_a, for a variety of plasma parameters. In all cases, we find that the bulk transport rate ν_p is directly proportional to the TPDM damping rate γ_a. For most of the data sets in Figure 4.8, γ_a is varied by increasing the

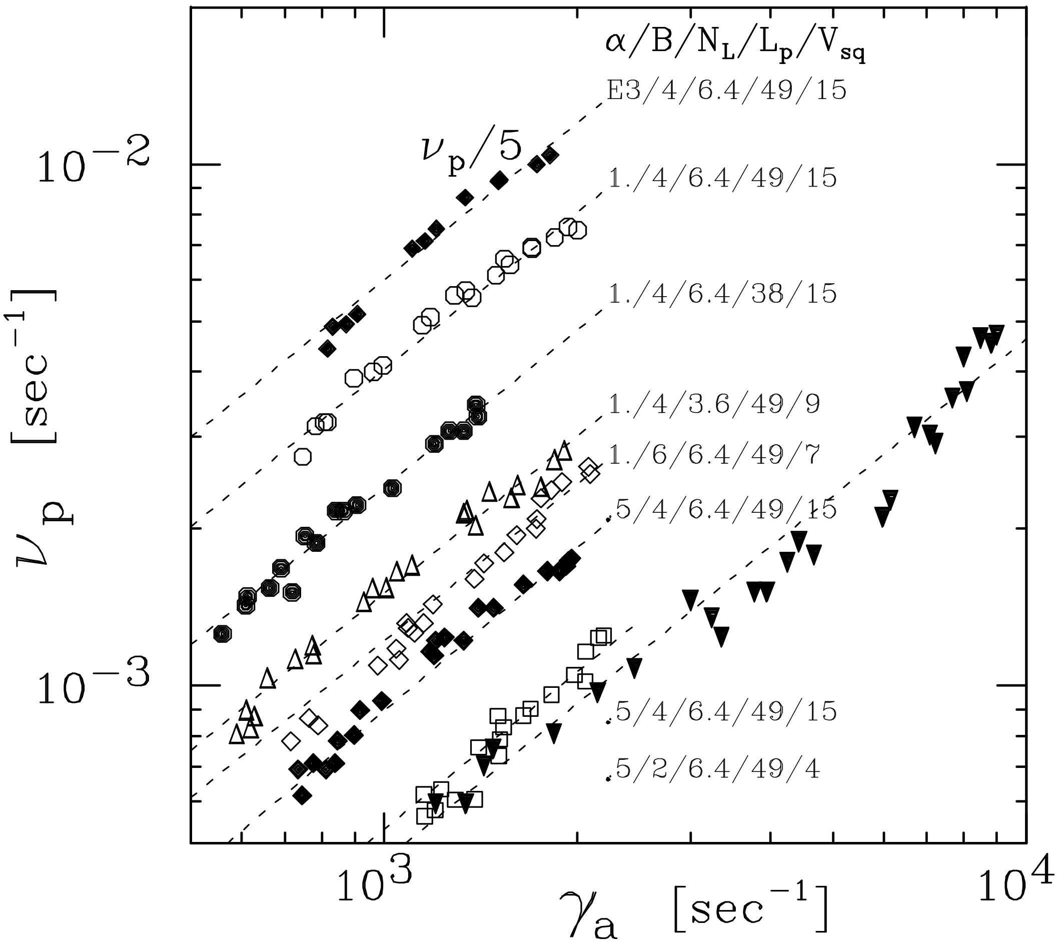

Figure 4.8: Measured transport rate ν_p versus the TPDM damping rate γ_a for various plasma parameters, showing a remarkably simple proportionality between ν_p and γ_a.

plasma temperature T using standard wiggle heating [32, 33]. For the data set with γ_a extending to $\sim 10^4$ sec^{-1} (marked as black triangles), a weak RF drive that is resonant with the separatrix velocity is used to enhance separatrix crossings (and γ_a), in the same fashion as in section 4.3.3.

The Figure 4.8 labels are in units of: magnetic or electric tilt angle α [mrad], magnetic field B [kG], plasma line density N_L [10^7 cm^{-1}], plasma length L_p [cm], and squeeze voltage V_{sq} [V]. The "E3" tilt label represents an electric tilt.

4.4.3 Plasma Parameter Scalings

Previous experiments show that the observed asymmetry-induced transport rate depends in a complicated fashion on plasma parameters. Here we show that in a squeezed, tilted plasma, ν_p is directly proportional to γ_a. This correspondence demonstrates that asymmetry-induced transport and TPDM damping are both caused by the same physical process, namely dissipative separatrix crossings.

For magnetic tilt, varying all the plasma parameters ($n, B, R_p, L_p, T, V_{sq}$, and α_B) shows that the overall transport scaling is given by

$$\frac{\nu_p}{\gamma_a} \approx 7.5 \times 10^{-5} \left(\frac{V_{sq}}{\phi_p}\right) \left(\frac{eN_L^2}{B}\right) \left(\frac{L_p}{R_w}\right)^2 \alpha_B^2. \tag{4.11}$$

Figure 4.9 shows that the normalized transport rate ν_p/γ_a follows the scaling of Equation 4.11 over a range of nearly three decades in ν_p/γ_a. Each point here is obtained from the slope of a data set similar to Figure 4.8. The term V_{sq}/ϕ_p represents the number of trapped particles (from Equation 4.1), and $(\alpha_B L_p/R_w)^2$ represents the strength of the electric potential fluctuation due to tilt. Currently, the term eN_L^2/B is not understood theoretically.

4.4.4 Electric and Magnetic Tilts

In this section, we study plasma transport with a “single” and “double” electric tilt. Electric tilt refers to an $m = 1$ electrostatic asymmetry applied to sectored cylinders. As mentioned, a single electric tilt consists of ± voltages applied to a fraction of the plasma length at one end only. A double electric tilt consist of voltages applied to *both* plasma ends antisymmetrically in z (phase difference of approximately π).

Magnetic and electric tilts can be placed on an equal footing by considering the off-axis (radial) shift Δ that the asymmetry induces [15]. Figure 4.10 shows

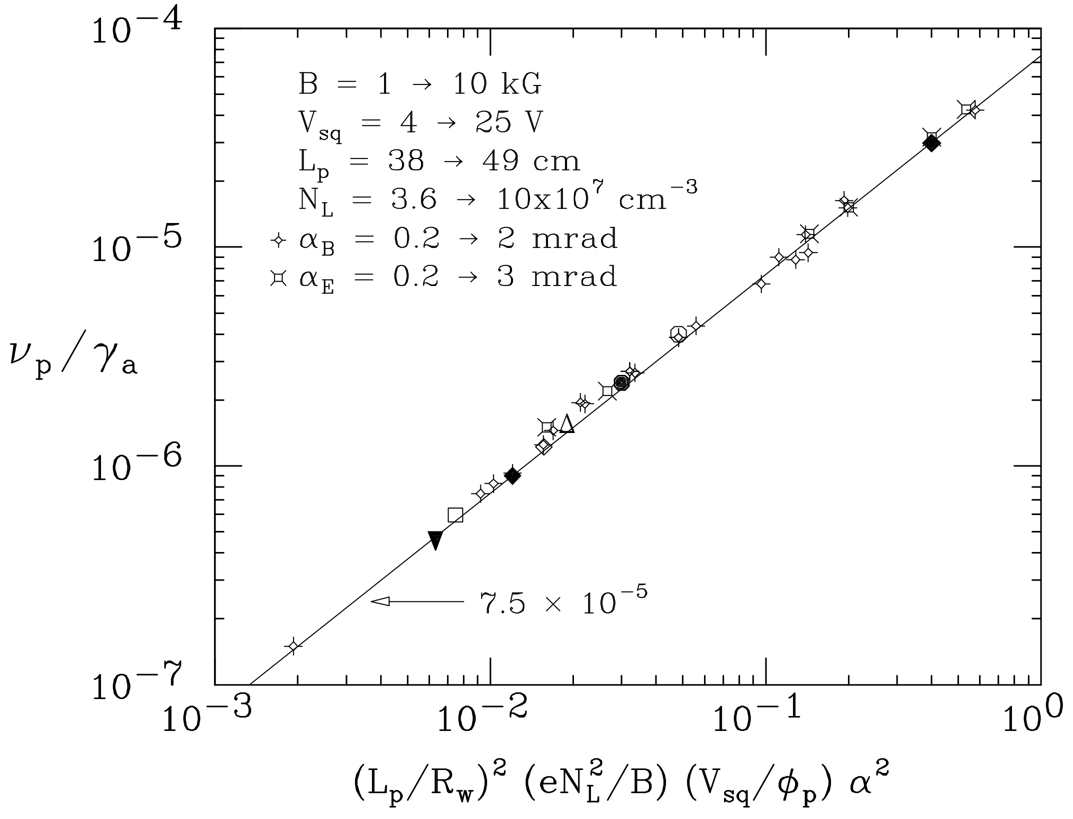

Figure 4.9: Scaling of the measured normalized transport rate ν_p/γ_a for all plasma parameters.

a cartoon of the presumed equilibria (neglecting Debye shielding) for a magnetic and simple (single-end) electric tilt, and shows the radial shift Δ in each case. The dashed line represents the trap axis, and the solid line represents the plasma center-of-mass.

A *magnetic* tilt shifts each $(L_p/2)$ half of the column off-axis by a z-averaged amount

$$\overline{\Delta}_B = \frac{1}{2}\alpha_B\,(L_p/2)\,. \tag{4.12}$$

Similarly, an $m = 1$ single-ended *electric* "tilt", consisting of asymmetry voltages $\pm V_a$ applied to sectors of length L_a at one end of the plasma, shifts the plasma equilibrium off-axis; it does not actually tilt the plasma, except through the

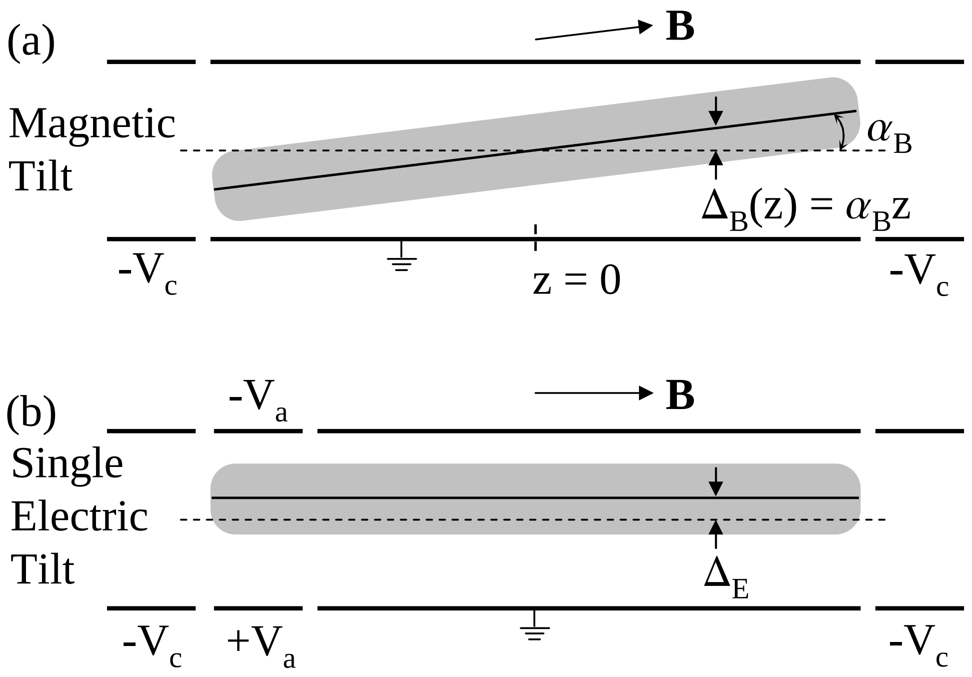

Figure 4.10: Schematic of presumptive asymmetric equilibria: (a) magnetic tilt with off-axis plasma shift Δ_B, and (b) single electric "tilt", showing that the plasma as a whole moves off-axis by $\Delta_E^{(s)}$ toward the negative asymmetry electrode.

Debye shielding component (not shown). An approximate theoretical expression for the plasma center-of-mass displacement $\Delta_E^{(s)}$ from a single electric tilt is found by balancing the forces from the plasma image charges and the bounce-averaged asymmetry field [15]. This treatment ignores fringing fields from the applied wall voltage, and gives

$$\frac{\Delta_E^{(s)}}{R_w} = \frac{\Phi_a}{2eN_L}\frac{L_a}{L_p}, \tag{4.13}$$

where L_a is the length of the asymmetry sectors, and $\Phi_a \equiv k_a V_a$ is the $m = 1$ asymmetry strength. Here, $k_a = (0.51$ or $0.64)$ represents the $m = 1$ Fourier component of the applied ± wall voltage for S7 ($2 \times 25°$) or S4 ($60°$) sectors, respectively [15].

Kriesel studied the equilibrium displacement $\Delta_E^{(s)}$ of an electron column due to an $m = 1$ single electric "tilt", and found that the column was *uniformly shifted* off-axis, as opposed to tilted or kinked [15]. To be consistent with the existing literature, we continue to use the phrase "electric tilt" to describe applied electric asymmetries.

We take a similar approach to Kriesel and use the measured quadrupole moment q_2 of the density image of a dumped plasma to infer the z structure of the plasma. The quadrupole moment of a plasma that is tilted in z is expected to increase with applied asymmetry strength V_a, while q_2 measured from a shifted plasma is expected to be near zero, since the plasma remains circular as it shifts off the trap axis.

Our data supports Kriesel's conclusion that a single electric tilt creates a shifted plasma column rather than a tilted column. Figure 4.11 shows the measured plasma center-of-mass displacement $\Delta_E^{(s)}$ (dashed lines) and quadrupole moment q_2 (solid lines) versus the applied asymmetry voltage V_a, for both V_a on and off during the plasma dump. The theory prediction of Equation 4.13 for $\Delta_E^{(s)}$ is shown as the dot-dash line, and agrees within 20% with the data. The plasma has length $L_p = 21$ cm, $B = 1$ kG, $N_L = 6.3 \times 10^7$ cm^{-1}, and $T \approx 1$ eV. The quadrupole moment q_2 is defined by the semi-major axis a and semi-minor axis b of an ellipse, and is given by

$$q_2 \equiv \frac{(a/b)^2 - 1}{(a/b)^2 + 1}. \tag{4.14}$$

The single-tilt off-axis plasma displacement $\Delta_E^{(s)}/R_w$ is approximately linear with V_a, and is essentially the same with V_a on and V_a off during the dump. Here, the asymmetry is applied to the dump end of the plasma. The measured quadrupole moment q_2, however, depends on whether or not the asymmetry voltage is turned off during the dump process. When the asymmetry voltage is turned off immediately before the dump (within $2 - 3$ μs), the quadrupole moment is

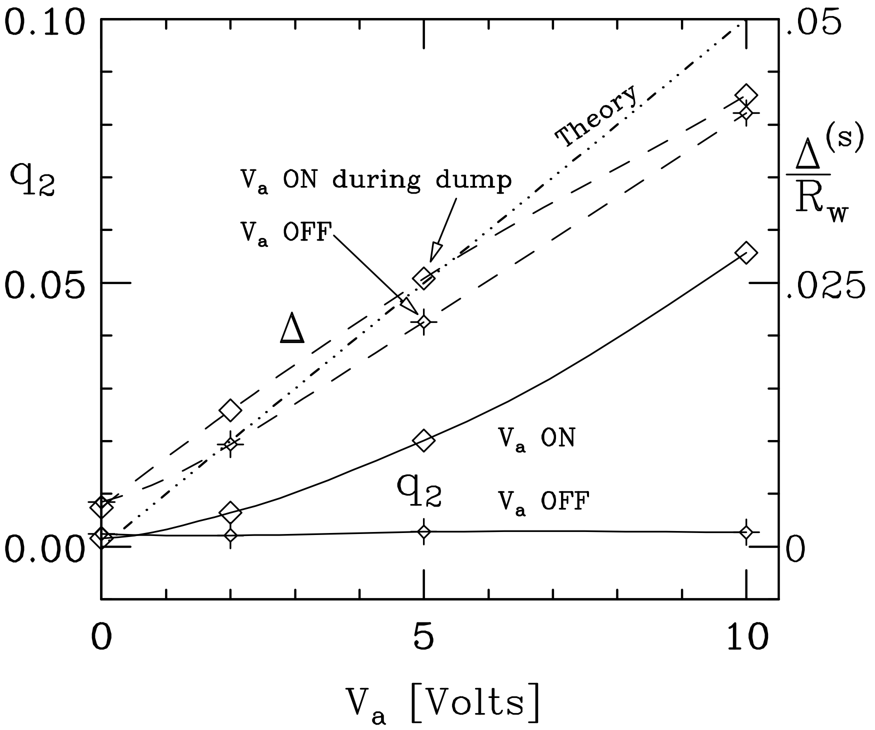

Figure 4.11: Measured off-axis shift $\Delta_E^{(s)}/R_w$ and quadrupole moment q_2 versus asymmetry voltage strength V_a, with an $m = 1$ electric asymmetry applied to the "dump" end of the plasma. The plasma shifts off-axis toward the negative electrode when the asymmetry is applied at one end of the plasma only.

essentially zero and is independent of V_a, supporting the idea of a shifted plasma. In addition, the plasma moves a distance $\Delta_E^{(s)}$ toward the negative asymmetry electrode, in agreement with previous experiments [15, 39].

With V_a *on* during the dump, electrons are trapped behind the negative asymmetry sector, shown schematically in Figure 4.12. Trapped electrons create a θ-localized deficit of electrons in the measured z-integrated electron density, which causes q_2 to increase with the asymmetry strength, as shown in Figure 4.11. In addition, we measure the number of electrons N_t trapped behind the asymmetry sector after the dump, by subtracting a CCD image of a plasma with $V_a \neq 0$ from an image with $V_a = 0$, and find that N_t increases linearly with V_a.

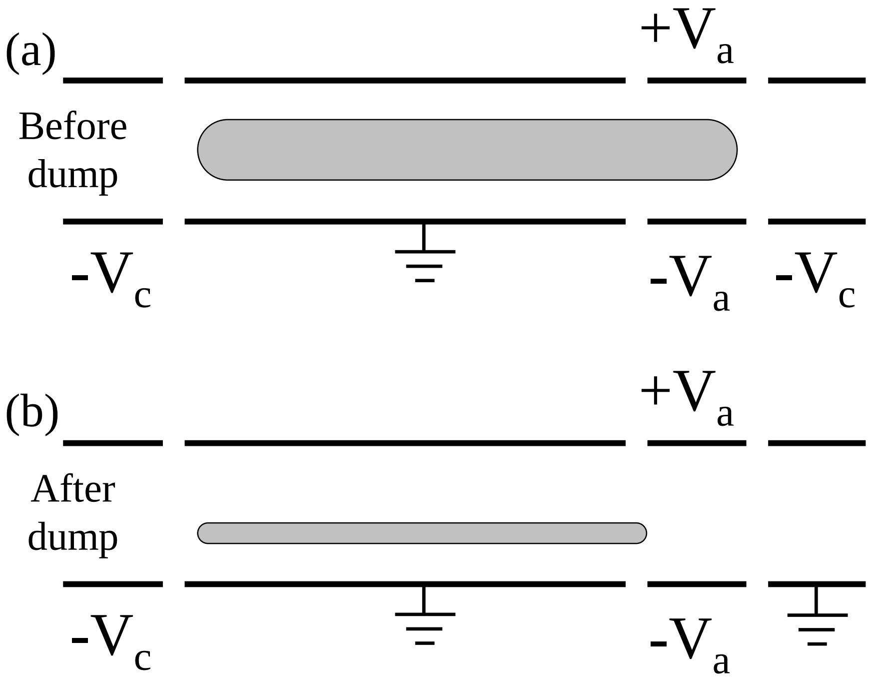

Figure 4.12: With the asymmetry field on during the dump, electrons are trapped behind the negative voltage sector.

We define an electric tilt angle α_E by the off-axis plasma shift due to a double electric tilt

$$\Delta_E^{(d)} \approx k_a R_w \left(\frac{V_a}{2eN_L} \right) \left(\frac{2L_a}{L_p} \right) \equiv \alpha_E \left(\frac{L_p}{4} \right). \tag{4.15}$$

Using this definition of α_E, the simple magnetic tilt scalings for ν_p/γ_a (Equation 4.11) also hold for electric tilt, whether the electric tilt is applied alone or in combination with a magnetic tilt. When both an electric and magnetic tilt are present, the electric tilt can partially cancel a magnetic tilt, and vice versa, demonstrating that both types of tilt are equivalent in terms of transport.

Figure 4.13 and Figure 4.14 show the transport rate ν_p from simultaneous electric and magnetic tilts. Here, static asymmetry voltages V_{ax} or V_{ay} are applied as ± pairs to θ-opposing and z-opposing wall sectors oriented in the $\hat{x}$ or $\hat{y}$ directions, with a simultaneously applied magnetic tilt α_{By} in the $\hat{y}$ direction.

Figure 4.14 has magnetic tilts α_{Bx} and α_{By} in the presence of a $\hat{y}$ electric tilt. For both electric and magnetic tilts, the transport rate scales quadratically with tilt asymmetry, for small asymmetries. At large values of ν_p, the rapid transport causes expansion-induced plasma heating, and the scaling of ν_p with asymmetries deviates from quadratic. The dashed lines show apparent linear scaling, which we believe to be of no particular significance.

Using the definition of α_E from Equation 4.15, the electric tilt transport of Figure 4.13 is identical to the magnetic tilt transport characterized by Equation 4.11. The complete scaling for electric and magnetic tilt-induced transport is thus

$$\frac{\nu_p}{\gamma_a} \approx 6.3 \times 10^{-5} \left(\frac{N_L^{tr}}{N_L}\right) \left(\frac{eN_L^2}{B}\right) \left(\frac{L_p}{R_w}\right)^2 (\vec{\alpha}_B + \vec{\alpha}_E)^2 , \tag{4.16}$$

where $\vec{\alpha} = \alpha_x \hat{x} + \alpha_y \hat{y}$, and Equation 4.1 was used for N_L^{tr}. Note that the cross term $\vec{\alpha}_B \cdot \vec{\alpha}_E$ is only approximate, since the electric asymmetry is applied at discrete z positions. Thus, $\Delta_E(z) \neq z\,\alpha_E$, and the "$z$-overlap integral" between electric and magnetic tilts is generally less than unity.

4.5 Double Electric Tilt

4.5.1 Background

Figure 4.15 is a schematic of a double electric "tilt," with a squeeze trapping barrier applied to the plasma. Figure (a) shows the equilibrium center-of-mass of *trapped* particles as the solid lines, and shows trapped-particle off-axis shift $\Delta_E^{(d)}$. Presumably, the position of trapped particles is the same as that for two separate plasmas with single electric tilts.

Figure 4.15(b) shows the same plasma, with the perspective of "looking" at the bottom of Figure (a). Here, the solid line represents the center-of-mass of *passing displaced* particles, and the z-structure of this line is only approximate.

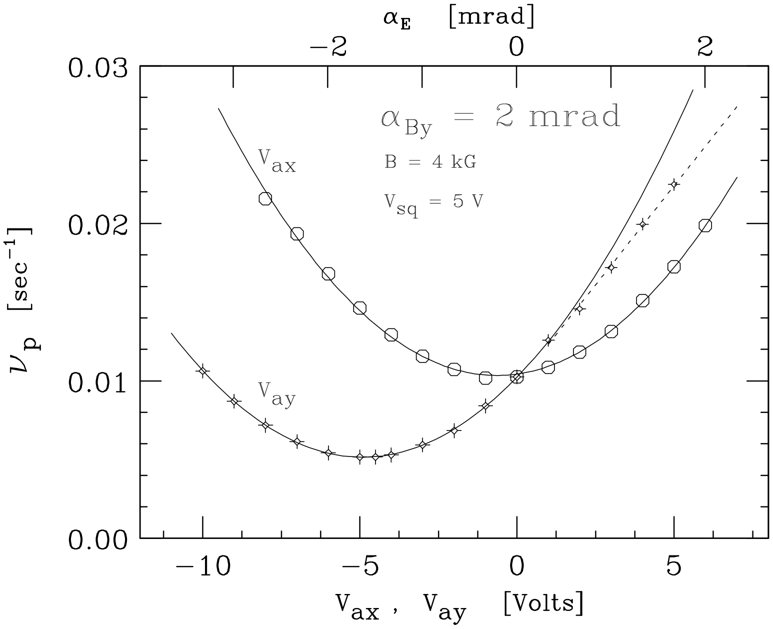

Figure 4.13: Measured transport rate ν_p from static asymmetry voltages with simultaneously applied magnetic tilt. The shift of the minimum of the V_{ay} curve to −5 V, and the reduction of the measured transport rate, shows that an electric tilt can partially cancel a magnetic tilt.

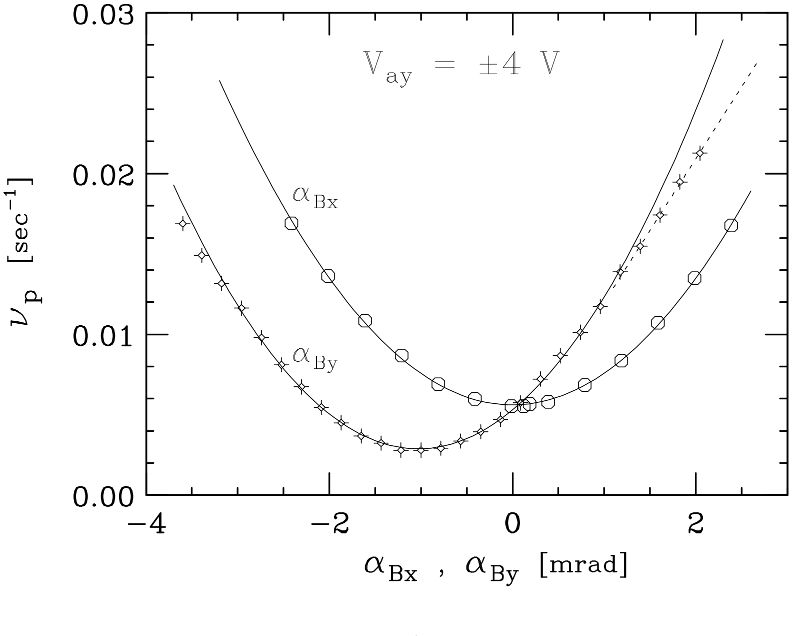

Figure 4.14: Measured transport rate ν_p from magnetic tilts, with simultaneously applied electric asymmetry.

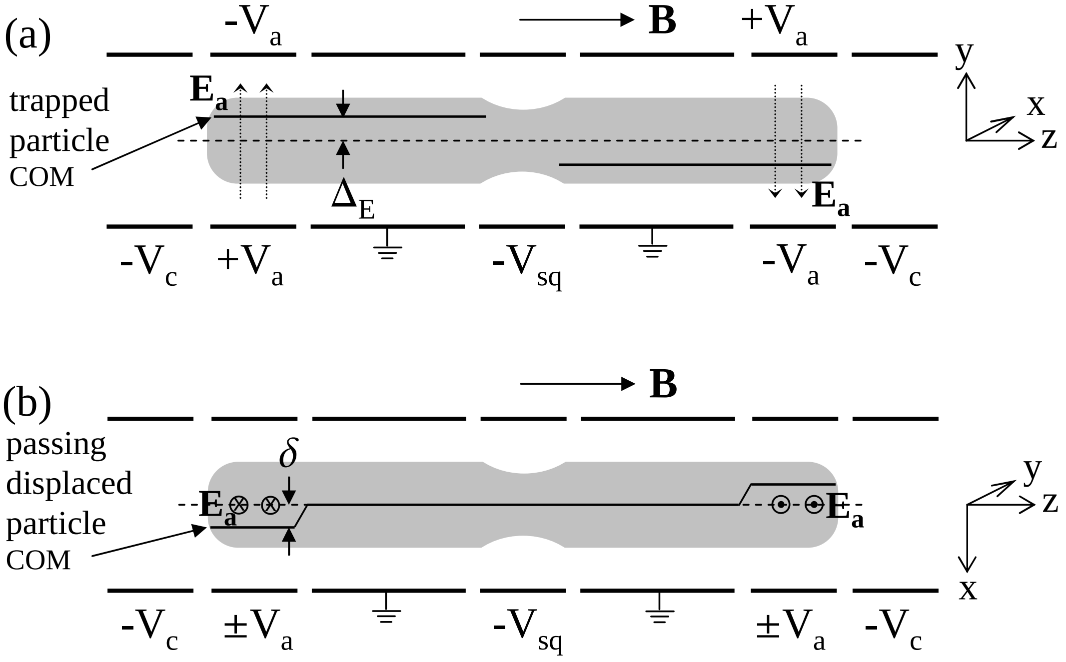

Figure 4.15: Schematic of a plasma with applied double electric tilt showing (a) the equilibrium trapped particle center-of-mass (COM) position from a perspective perpendicular to the electric tilt axis; and (b) the passing displaced particle COM position from a perspective parallel to the tilt axis.

These particles sample the entire length of the plasma, and are displaced on average a distance δ due to $\mathbf{E} \times \mathbf{B}$ drifts in the applied $E_a\,\hat{y}$ asymmetry field. Experiments show that the passing displaced particles are shifted approximately 90° with respect to the electric tilt axis.

We apply a double electric tilt and an optional electric squeeze near the center of the trap, and measure the z-integrated electron density $n^{(h)}(r,\theta)$ by dumping *half* the plasma column. The double electric tilt is applied using a method that minimizes the wall-measured $m = 1, k_z = 0$ diocotron amplitude. The tilted plasma is held for hundreds of $\mathbf{E} \times \mathbf{B}$ rotation periods, and then is cut axially (approximately in half) by suddenly lowering the squeeze voltage to -100 V. The ramp time of the cut is $\sim$2 μs, which is about the same as a thermal electron bounce period $\bar{f}_b^{-1} = 2L_p/\bar{v}$.

The double tilt asymmetry voltages and the time of asymmetry application are chosen so that the wall-measured $m = 1$ diocotron mode amplitude is minimized. The sectored electrodes on each end of the plasma, S4 and S7, do not have the same surface area, and the ratio of the $m = 1$ Fourier components for each cylinder is $k_a^{(S7)}/k_a^{(S4)} = 0.51/0.64 = 0.80$. We experimentally determine that the ratio between the asymmetry voltages applied to S4 and to S7 that minimizes the $m = 1$ diocotron amplitude is $V_a^{S4}/V_a^{S7} = 0.7$.

In addition, the axes of the electric tilts on each side of the squeeze cylinder are slightly different (S4 leads S7 by $\vartheta = 15°$ with respect to the plasma $\mathbf{E} \times \mathbf{B}$ drift direction); thus we apply asymmetry voltage V_a^{S4} to S4 $\Delta t \approx 4.8\,\mu$s (at $B = 4$ kG) *before* applying asymmetry voltage V_a^{S7} to S7. The time difference Δt between asymmetry application to S4 and S7 is determined experimentally, again by minimizing the $m = 1$ diocotron amplitude. The magnitude of Δt is consistent with the known phase difference ϑ between S4 and S7, since

$$\frac{\Delta t}{T_1} 360° = \frac{4.8\,\mu\text{s}}{125\,\mu\text{s}} 360° = 13.8° \simeq \vartheta, \tag{4.17}$$

where $T_1 = 125\,\mu$s is the $m = 1$ diocotron period at 4 kG.

4.5.2 Experiments

With the asymmetry still on, the half-plasma is dumped onto the phosphor screen a chosen time τ_d after the cut, giving the measured half-plasma center-of-mass position $(r_p^{(h)}, \theta_p^{(h)})$, as shown in Figure 4.16. The center-of-mass data points shown in the figure trace out the first $m = 1$ diocotron orbit after the cut.

We find that when the half-plasma is dumped immediately after the cut ($\tau_d \approx 0$), the measured angular position $\theta_p^{(h)}$ shifts by roughly 90° with respect to the θ-center of the negative electrode (or axis of electric tilt). In Figure 4.16,

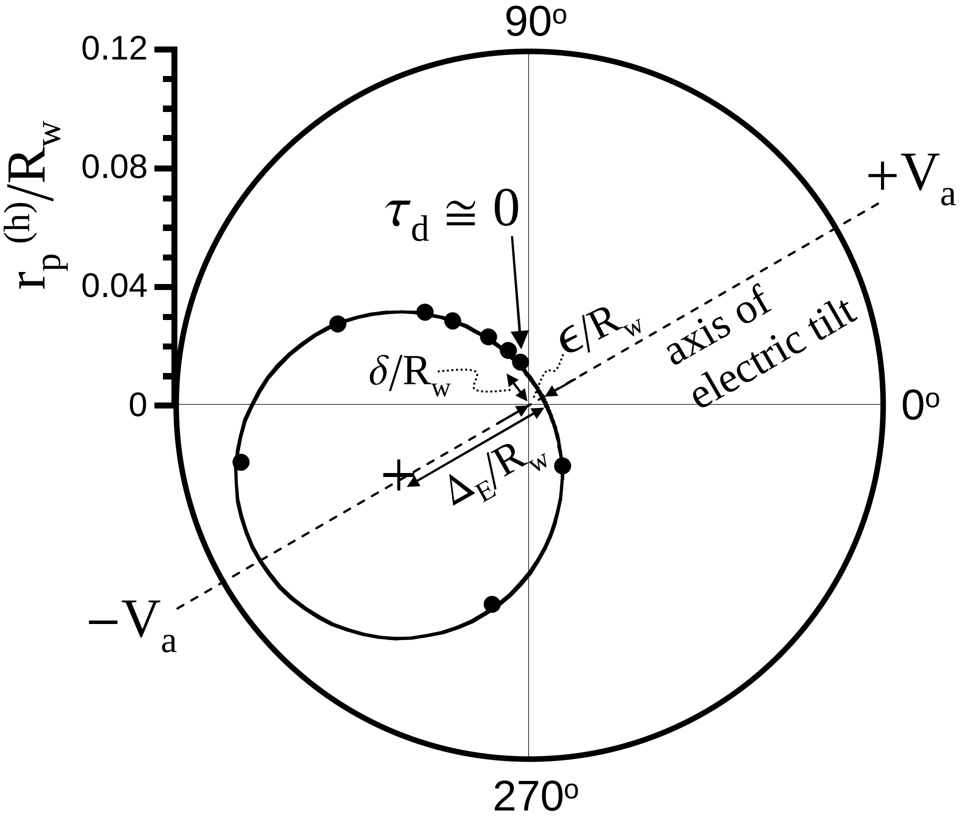

Figure 4.16: The measured positions $(r_p^{(h)}, \theta_p^{(h)})$ of the center-of-mass of a half-plasma, held for various durations τ_d after the cut. The asymmetry voltages are on during the dump. Immediately after the cut, the measured plasma location is shifted roughly 90° with respect to the electric tilt axis.

the circle through the data points is an off-axis circle-fit to the data. The center of this fit is the equilibrium position for trapped particles (in the right-half of the plasma), and is shown as a "+" symbol in Figure 4.16. After the cut, the half-plasma executes a dioctron orbit around this equilibrium position. If diocotron mode feedback damping is applied after the cut, the plasma eventually settles to the (+) position.

We define the off-axis shift $\Delta_E^{(d)}$ of trapped particles as the radius of the circle-fit to data from one diocotron orbit, as in Figure 4.16. We define the half-plasma z-integrated shift δ of passing displaced particles from the measured radial displacement of a plasma dumped simultaneously with the axial cut ($\tau_d \approx 0$). We interpret δ as merely representing the fraction of the diocotron orbit (centered at the equilibrium position) that particles execute during the dump-transit time. This transit time is the minimum time particles spend in one half of the plasma, and is on the order of $L_p/\bar{v} \sim 2\ \mu\text{s} \sim 1/25 f_d$. Figure 4.16 also shows the small displacement ϵ, which presumably represents the Debye shielding component of the plasma shift.

Figure 4.17 shows the measured passing displaced particle shift δ, the equilibrium shift $\Delta_E^{(d)}$ of the cut plasma, and the measured shift ϵ (due to presumptive Debye shielding), versus the applied asymmetry voltage V_a^{S7}: all three shifts increase approximately linearly with V_a. The solid lines merely connect the data points. Here, the asymmetry strength $\Phi_a = 0.51\, V_a^{S7}$, where 0.51 is the $m = 1$ Fourier component for S7 sectors. The dashed line is the theory prediction for $\Delta_E^{(d)}$, using half the plasma length $L_p/2$ in place of L_p in Equation 4.13.

The Debye shielding response ϵ is found by balancing the applied asymmetry electric field $E_a \equiv \Phi_a/R_w$ with the electric field developed in the plasma due to the shielding perturbation $\delta N \equiv N\epsilon/R_p$. This predicts a shift of the (negative electron) plasma toward the positive electrode, and the shift is given by

$$\frac{\epsilon}{R_w} = \frac{\Phi_a}{2eN_L}\left(\frac{R_p}{R_w}\right)^2 \frac{2L_a}{L_p} \tag{4.18}$$

in the opposite direction compared with the equilibrium shift $\Delta_E^{(d)}$. The ratio of the predicted Debye shielding shift to the equilibrium shift is

$$\frac{\epsilon}{\Delta_E^{(d)}} \approx \left(\frac{R_p}{R_w}\right)^2 . \tag{4.19}$$

From Figure 4.17, we obtain $\epsilon/\Delta_E^{(d)} \approx 1/10$, which is reasonably close to the known ratio $(R_p/R_w)^2 = 0.08$.

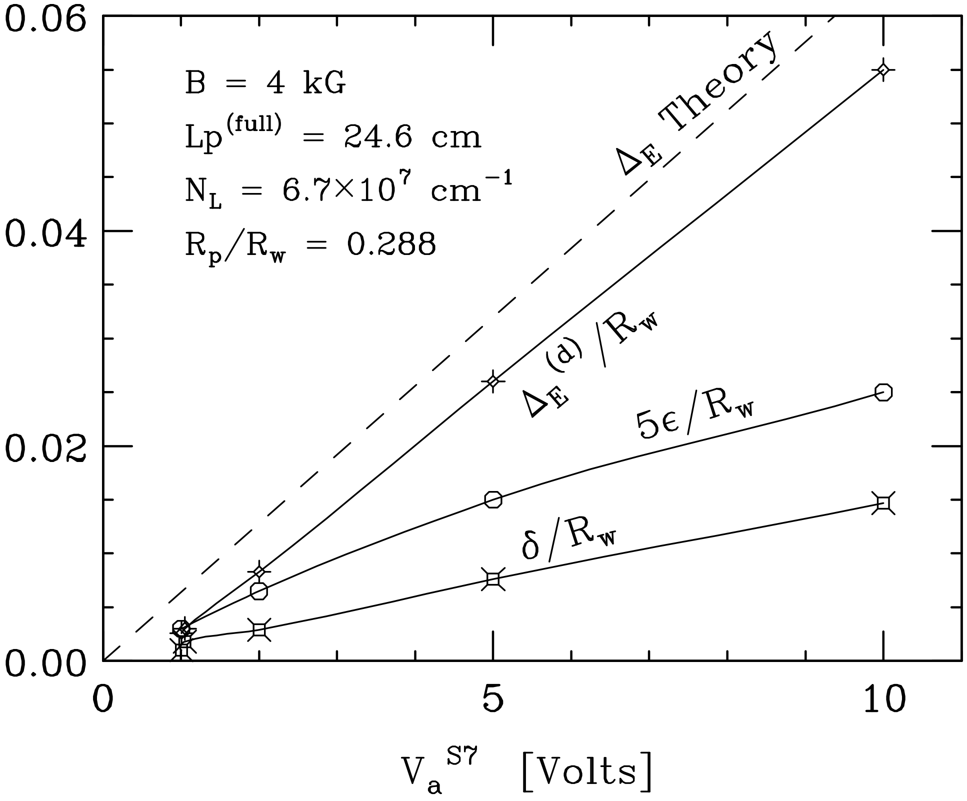

Figure 4.17: The measured shift δ from passing displaced particles, the radial equilibrium shift $\Delta_E^{(d)}$, and the measured shift ϵ (due to presumptive Debye shielding).

Figure 4.18 shows the measured ratio $\delta/\Delta_E^{(d)}$ versus magnetic field B, and shows the diocotron rotation B^{-1} scaling as the dashed line. The δ data have a magnetic field scaling that is slightly weaker than B^{-1}, presumably due to magnetic-field-dependent temperature changes. In the experiments, the plasma temperature increases due to plasma expansion, and this effect is stronger at low magnetic fields. The transit-dump time depends on the plasma temperature; thus, the distance δ (that the plasma moves on its diocotron orbit) is smaller at larger temperatures. Figure 4.18 also shows that the normalized equilibrium position $\Delta_E^{(d)}$ is independent of B.

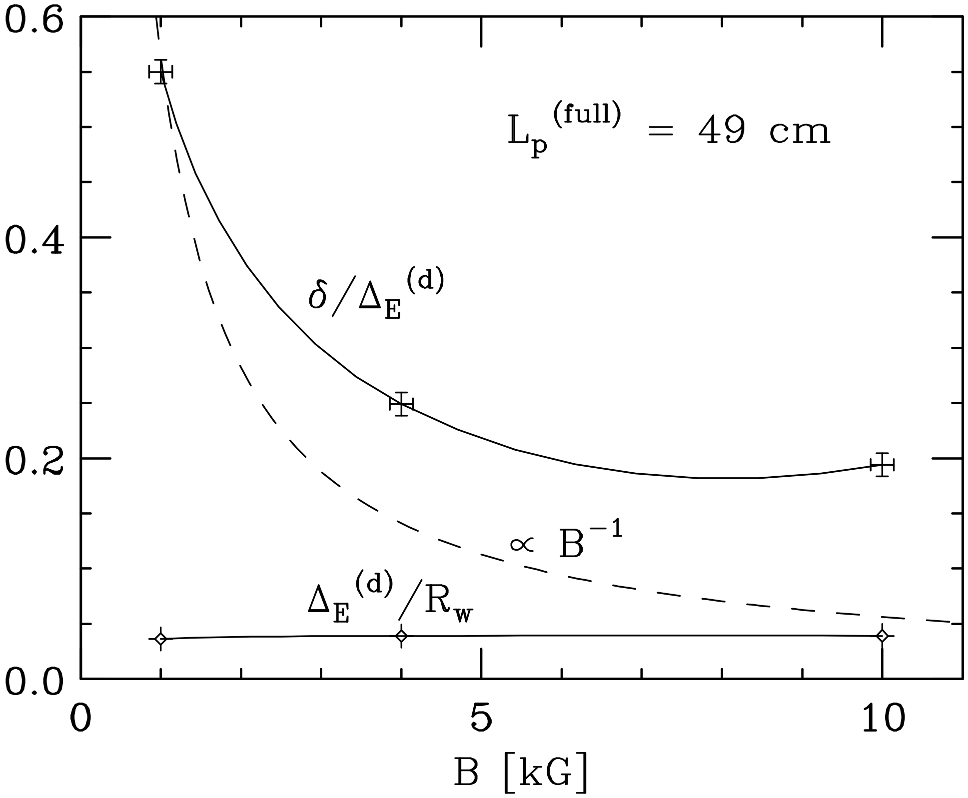

Figure 4.18: The ratio of the passing displaced particle shift to the equilibrium position versus magnetic field B. The solid lines merely connect the data points.

4.6 Transport with Magnetic Trapping

Figure 4.19 shows a schematic of a magnetic squeeze in a pure electron trap. The magnetic mirror strength is defined as $\beta \equiv \delta B/B = (B_H/B_L) - 1$, where B_H is the maximum field strength, and B_L is the nominal minimum field strength. We label the z position in the low field region as z_L, and the position of the highest field region as z_H.

As an electron enters a strong field region from a weak field region, its perpendicular velocity $v_\perp$ increases to conserve μ. The increase in $v_\perp$ causes a decrease in v_z due to energy conservation. At some point, if the mirror ratio β is large enough, v_z reaches zero, and the electron is reflected back to the weak field

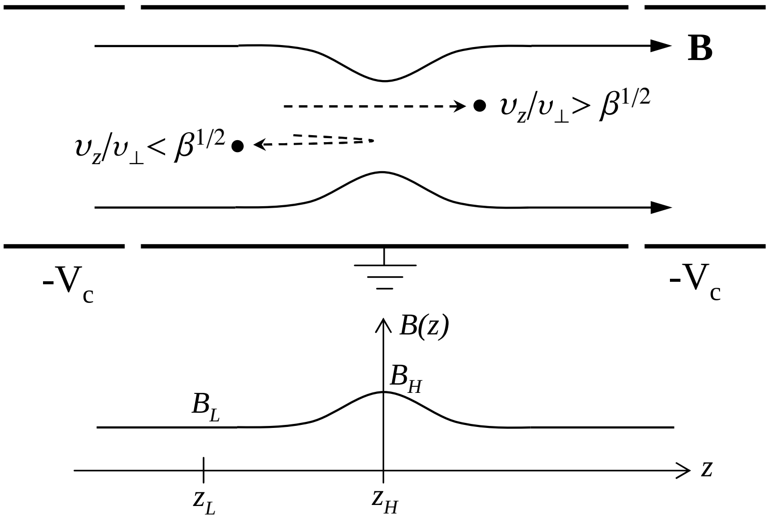

Figure 4.19: Magnetic squeeze in the electron trap. An electron guiding center, labeled by the symbol •, is "reflected" by the magnetic mirror if $v_z/v_\perp < \sqrt{\beta}$. When the opposite condition is true, the electron samples the entire trap length.

region. The threshold $v_z/v_\perp$ ratio (in the low field region) for reflection is found by setting the guiding-center's turning point to the maximum field position z_H. At this turning point, $v_z(z_H) = 0$, and conservation of energy yields

$$v_\perp^2(z_H) = v_\perp^2(z_L) + v_z^2(z_L). \tag{4.20}$$

The invariance of μ gives

$$\frac{v_\perp^2(z_H)}{B_H} = \frac{v_\perp^2(z_L)}{B_L}. \tag{4.21}$$

Combining the above two equations with the mirror ratio β gives the simple magnetic separatrix as

$$v_z = \beta^{1/2} v_\perp, \tag{4.22}$$

where the velocities are those in the low field region.

Equation 4.22 defines the naive magnetic separatrix. Recent work by Fajans [40] shows that a magnetic squeeze causes the electrostatic potential in a nonneutral plasma to vary along a field line by $\Delta\phi$, where $e\Delta\phi$ is on the order of βT. The

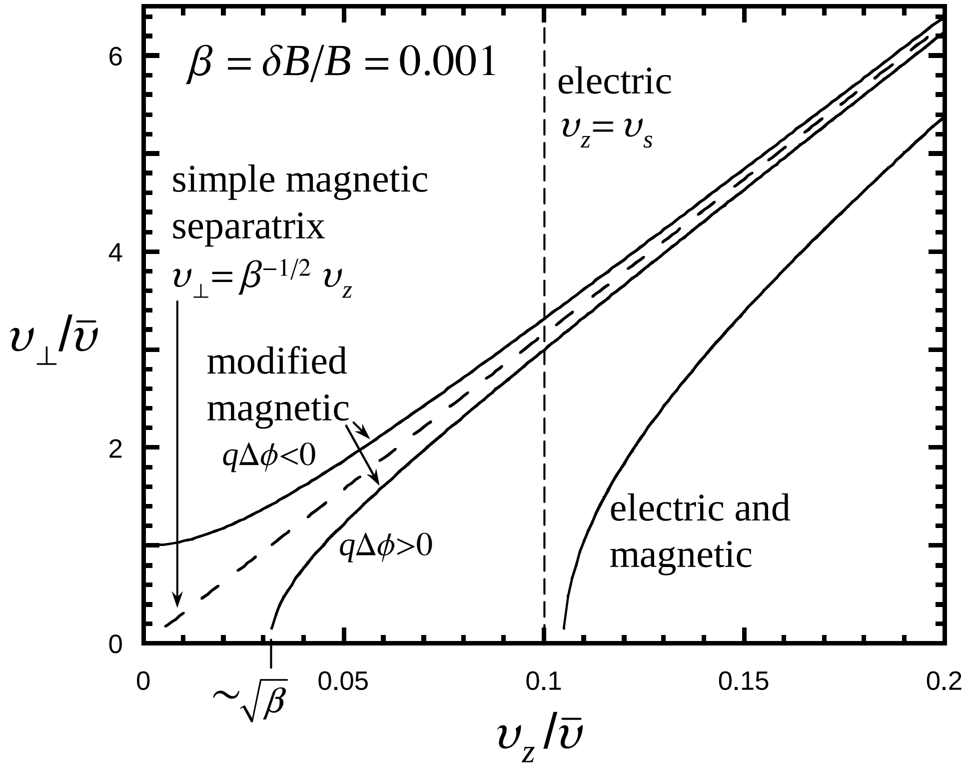

Figure 4.20: Velocity-space separatrices for magnetic trapping, electric trapping, and simultaneous electric and magnetic trapping. Trapped particles are to the left of the separatrices, and passing particles are to the right.

magnetic separatrix is then given by

$$v_z^2 = \beta v_\perp^2 - \frac{2e}{m}\Delta\phi. \tag{4.23}$$

Figure 4.20 shows the simple magnetic separatrix of Equation 4.22 as the diagonal dashed line, and shows the modified magnetic separatrices of Equation 4.23, with $q\Delta\phi > 0$ and $q\Delta\phi < 0$. All magnetic separatrices in the figure are drawn for a magnetic mirror strength $\beta = 10^{-3}$. An applied electric squeeze voltage V_{sq} adds in a similar fashion as $\Delta\phi$, and the separatrix is shown for both an electric and magnetic squeeze applied simultaneously. For comparison, an electric-only separatrix from $eV_{sq} = T/200$ is shown as the vertical dashed line.

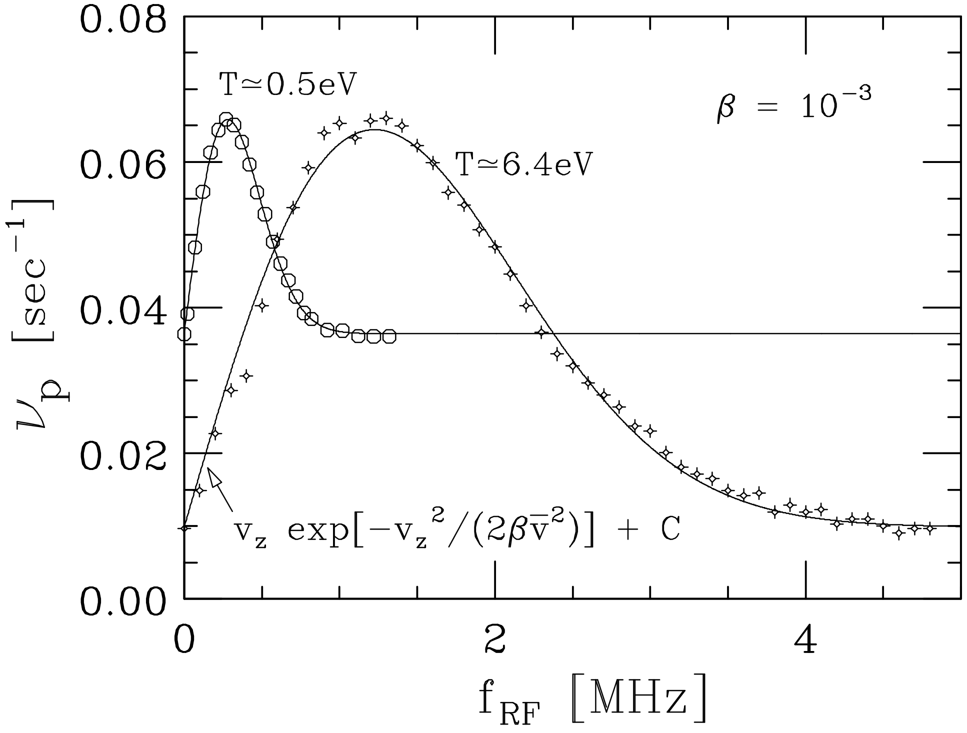

Figure 4.21: The measured transport rate ν_p versus an applied RF field at frequency f_{RF}, at two different temperatures. Two weak magnetic maxima are in the plasma region, and the RF drive enhances separatrix crossings when the resonance condition is satisfied. The data closely resemble Maxwellian distributions, shown as solid lines.

4.6.1 Mapping the Magnetic Separatrix

In a plasma with a weak magnetic mirror, we apply an RF signal to resonantly excite particles in the boundary layer near the separatrix. By varying the frequency of the applied RF signal, we map out the Maxwellian distribution along the separatrix [34].

Figure 4.21 shows the measured transport rate ν_p when a 0.1 V peak-to-peak RF wiggle is applied to a plasma with two small magnetic maxima in the plasma region. The RF drive is applied near the magnetic minimum. Separatrix crossings are enhanced when electrons receive a nonadiabatic kick from the RF drive. These kicks occur when the “sheath transit” resonance condition $v_z \approx L^* f_{RF}$ is satisfied, where $L^* \equiv 2R_w/j_{01}$ represents the axial extent of the electric fields from the applied RF wiggle, and j_{01} is the first zero of the Bessel function J_0 of the first kind.

The transport scales with the number of particles crossing the separatrix. At each f_{RF}, the transport rate reflects the number of resonant electrons in the separatrix boundary layer. By varying f_{RF}, the measured transport rate in Figure 4.21 maps out the velocity distribution of electrons, and the solid lines are Maxwellian fits to the data. The fits in Figure 4.21 are given by

$$\nu_p = A\, v_z \exp\left(-\frac{v_z^2}{2\,\beta\,\bar{v}^2}\right) + C = A'\, f_{RF} \exp\left(-\frac{2R_w^2}{j_{01}^2\,\beta\,\bar{v}^2}\, f_{RF}^2\right) + C, \qquad (4.24)$$

where A and A' are amplitude coefficients, and the offset C represents transport due to Coulomb collision-induced scattering across the separatrix. This background small-angle scattering is temperature dependent, while the maximal transport rate of $\sim 0.06\ \text{sec}^{-1}$ in Figure 4.21 depends only on the RF drive scattering enhancement, and is independent of temperature.

Enhancing separatrix crossings with an Rf drive can be used as a temperature diagnostic, if the magnetic mirror strength β is known [34]. Using the measured $\beta = 10^{-3}$ from the superconducting magnet vendor, the fits give the plasma temperature as $T = 0.4$ and 7.3 eV for the low and high temperature plasmas, respectively, which agree within 14% with direct evaporative temperature measurements of 0.5 and 6.4 eV. Mapping the magnetic separatrix can also be used to find the magnetic mirror strength β, if the plasma temperature T is known. In addition, the agreement between the data and the fits suggests the electron velocity distribution is actually Maxwellian.

Appendix A

Estimate of Viscous Spreading of Filaments

Here we estimate the viscous spreading of a density filament in a cylindrically symmetric fluid, closely following previous work by Kriesel [15] and Driscoll [41].

Viscosity acts on shear in the plasma rotation, and causes radially adjacent fluid elements to resist slipping past each other. The difference in stress on the inward and outward sides of a fluid element leads to a viscous force F_θ in the azimuthal direction. This viscous force creates radial drifts v_r, resulting in a radial flux. We use continuity to relate the flux to the time-dependence of a filament with radial width $w(t)$.

Force balance for fluid of charge in a magnetic field is

$$\nabla \cdot \mathbf{P} = -en\left(\mathbf{E} + \frac{\mathbf{v}}{c} \times \mathbf{B}\right), \tag{A.1}$$

where $\mathbf{P}$ is the pressure-stress tensor. We assume here that all off-diagonal elements of this tensor are solely due to viscosity. The viscous stress is proportional to the shear, and the r-θ component of the stress tensor is

$$P_{r\theta} = P_{\theta r} = -\eta\, \tilde{S}, \tag{A.2}$$

where η is the coefficient of viscosity. The shear $\tilde{S}$ due to the density filaments is given by

$$\tilde{S} \equiv r\frac{\partial \tilde{\omega}_R}{\partial r} = \frac{c}{B}\nabla \cdot \tilde{E} = \frac{4\pi ec}{B}\delta n, \tag{A.3}$$

where the last step follows from Poisson's equation. In this Appendix, the tilde symbol " ~ " refers to quantities that result from the density filaments δn.

From Equation A.1, force balance in the θ-direction yields

$$\frac{1}{r^2}\frac{\partial}{\partial r}r^2 P_{r\theta} = \frac{en\tilde{v}_r B}{c}, \tag{A.4}$$

which gives a radial flux of particles

$$\tilde{\Gamma}_r \equiv n\tilde{v}_r = -\frac{c}{eB}\frac{1}{r^2}\frac{\partial}{\partial r}\left(r^2\eta\tilde{S}\right). \tag{A.5}$$

Continuity relates the rate of change of the pertubed density to the flux:

$$\frac{\partial \delta n}{\partial t} + \nabla \cdot \tilde{\Gamma}_r = 0, \tag{A.6}$$

which we simplify to

$$\frac{\delta n}{t} \approx \frac{c}{eB}\frac{\eta\tilde{S}}{(\Delta r)^2}, \tag{A.7}$$

where $(\Delta r)^2$ is the length scale over which the shear $\tilde{S}$ and δn change. An estimate for the radial width of a filament $w(t)$ is obtained from the above expression, yielding

$$w^2(t) \equiv (\Delta r)^2 \approx t\kappa\left(\frac{\omega_p}{\Omega_c}\right)^2, \tag{A.8}$$

where $\kappa \equiv \frac{\eta}{n\mathrm{m}}$ is the kinematic viscosity, $\omega_p \equiv (4\pi ne^2/\mathrm{m})^{1/2}$ is the electron plasma frequency, and $\Omega_c \equiv \frac{eB}{\mathrm{mc}}$ is the electron cyclotron frequency. Equation A.8 describes the viscous diffusion of a density filament, with the viscous diffusion coefficient given by $\kappa\left(\omega_p/\Omega_c\right)^2$.

We use Equation A.8 to estimate the viscous echo destruction time in Section 3.8.

References

[1] N.A. Kurnit, J.D. Abella, and S.K. Hartman. Observation of a photon echo. *Phys. Rev. Lett.*, 13:567, 1964.

[2] E.L. Hahn. Spin echoes. *Phys. Rev.*, 80:580, 1950.

[3] R.W. Gould. Cyclotron echo phenomena. *Am. J. Phys.*, 37:585, 1969.

[4] T.M. O'Neil and R.W. Gould. Temporal and spatial plasma wave echoes. *Phys. Fluids*, 11:134, 1968.

[5] J.H. Malmberg, C.B. Wharton, R.W. Gould, and T.M. O'Neil. Observation of plasma wave echoes. *Phys. Fluids.*, 11:1147, 1968.

[6] R.W. Gould. Dynamics of non-neutral plasmas. *Phys. Plasmas*, 2:2151, 1995.

[7] A.E. Lifshits. An echo effect in hydrodynamics. *Sov. Phys. Dokl.*, 34:783, 1989.

[8] J. Vanneste, P.J. Morrison, T. Warn. Strong echo effect and nonlinear transient growth in shear flows. *Phys. Fluids*, 10:1398, 1998.

[9] A.J. Peurrung and J. Fajans. A limitation to the analogy between pure electron plasmas and two-dimensional inviscid fluids. *Phys. of Fluids B*, 5:4295, 1993.

[10] A.A. Kabantsev, C.F. Driscoll, T.J. Hilsabeck, T.M. O'Neil, and J.H. Yu. Trapped-particle asymmetry modes in single-species plasmas. *Phys. Rev. Lett.*, 87:225002, 2001.

[11] A.A. Kabantsev and C.F. Driscoll. Trapped-particle modes and asymmetry-induced transport in single-species plasmas. *Phys. Rev. Lett.*, 89:245001, 2002.

[12] A.A. Kabantsev, J.H. Yu, R.B. Lynch, and C.F. Driscoll. Trapped particles and asymmetry-induced transport. *Phys. Plasmas*, 10:1628, 2003.

[13] T.J. Hilsabeck, A.A. Kabantsev, C.F. Driscoll, and T.M. O'Neil. Damping of the trapped-particle diocotron mode. *Phys. Rev. Lett.*, 90:245002, 2003.

[14] K.S. Fine, A.C. Cass, W.G. Flynn, and C.F. Driscoll. Relaxation of 2D turbulence to vortex crystals. *Phys. Rev. Lett.*, 75:3277, 1995.

[15] J.M. Kriesel. *Experiments on Viscous and Asymmetry-Induced Transport in Magnetized, Pure Electron Plasmas.* PhD Thesis, University of California at San Diego, 1999.

[16] A.C. Cass. *Experiments on Vortex Symmetrization in Magnetized Electron Plasma Columns*. PhD Thesis, University of California at San Diego, 1998.

[17] K.S. Fine and C.F. Driscoll. Experiments in vortex dynamics in pure electron plasmas. *Phys. Fluids B*, 2:1359, 1990.

[18] R.J. Briggs, J.D. Daugherty, and R.H. Levy. Role of Landau damping in crossed-field electron beams and inviscid shear flow. *Phys. Fluids*, 13:421, 1970.

[19] D.A. Schecter, D.H. Dubin, A.C. Cass, C.F. Driscoll, I.M. Lansky, and T.M. O'Neil. Inviscid damping of asymmetries on a two-dimensional vortex. *Phys. Fluids*, 12:2397, 2000.

[20] D.A. Schecter. *On the Dynamics of Inviscid Relaxation in 2D Fluids and Nonneutral Plasmas*. PhD Thesis, University of California at San Diego, 1999.

[21] A.P. Bassom and A.D. Gilbert. The spiral wind-up and dissipation of vorticity and a passive scalar in a strained planar vortex. *J. Fluid Mech.*, 398:245, 1999.

[22] N.J. Balmforth, S.G. Smith, and W.R. Young. Disturbing vortices. *J. Fluid Mech.*, 426:95, 2001.

[23] Lord Kelvin. On the vibrations of a columnar vortex. *Phil. Mag.*, 10:155, 1880.

[24] T.M. O'Neil, private communication.

[25] Lord Kelvin. On a disturbing infinity in Lord Rayleigh's solution for waves in a plane vortex stratum. *Nature*, 23:45, 1880.

[26] N.S. Pillai and R.W. Gould. Damping and trapping in 2D inviscid fluids. *Phys. Rev. Lett.*, 73:2849, 1994.

[27] D.H. Dubin and T.M. O'Neil. Two-dimensional bounce-averaged collisional particle transport in a single species non-neutral plasma. *Phys. Plasmas*, 5:1305, 1998.

[28] S. Ichimaru. *Basic Principles of Plasma Physics*. W.A. Benjamin, Inc., Reading, 1973, p. 244.

[29] E.H. Chao, S.F. Paul, R.C. Davidson, and K.S. Fine. Direct numerical solution of poisson's equation in cylindrical (r, z) coordinates. *PPPL techincal report*, PPPL-3251, 1999.

[30] D.D. Dubin, private communication.

[31] M.N. Rosenbluth, D.W. Ross, and D.P. Kostomarov. *Nucl. Fusion*, 12:3, 1972.

[32] B.R. Beck, J. Fajans, and J.H. Malmberg. Measurement of collisional anisotropic temperature relaxation in a strongly magnetized pure-electron plasma. *Phys. Rev. Lett.*, 68;317, 1992.

[33] B.P. Cluggish, J.R. Danielson, and C.F. Driscoll. Resonant particle heating of an electron plasma by oscillating sheaths. *Phys. Rev. Lett.*, 81:353, 1998.

[34] A.A. Kabantsev and C.F. Driscoll. Diagnosing the velocity-space separatrix of trapped particle modes. *Rev. Sci. Instrum.*, 74:1925, 2003.

[35] B.P. Cluggish and C.F. Driscoll. Transport and damping from rotational pumping in magnetized electron plasmas. *Phys. Rev. Lett.*, 74:4213, 1995.

[36] S. Crooks and T.M. O'Neil. Rotational pumping and damping of the $m = 1$ diocotron mode. *Phys. Plasmas*, 2:355, 1995.

[37] R. Keinigs. Field-error induced transport in a pure electron plasma column. *Phys. Fluids*, 27:1427, 1984.

[38] J.D. Crawford and T.M. O'Neil. Nonlinear collective processes and the confinement of a pure-electron plasma. *Phys. Fluids*, 30:2076, 1987.

[39] R. Chu, J.S. Wurtel, J. Notte, A.J. Peurrung, and J. Fajans. Non-neutral plasmas in asymmetric traps. *Phys. Fluids B*, 5:2378, 1993.

[40] J. Fajans. Non-neutral plasma equilibria, trapping, separatrices, and separatrix crossing in magnetic mirrors. *Phys. Plasmas*, 10:1209, 2003.

[41] C.F. Driscoll. Wall losses for a single species plasma near thermal equilibrium. *Phys. Fluids*, 25:97, 1982.